Unbound states of neutron-rich carbon isotopes

Silvia Murillo Morales

Doctor of Philosophy

University of York
Physics

September 2022

Abstract

We work upon the model of a two-state mixing of states of pure proton and pure neutron excitation to describe excited 2^+ states in carbon isotopes [1, 2]. The first 2^+ state of ^{16}C has been measured in other works showing it is dominated by neutron excitations and was recently confirmed in a study that has determined the proton amplitude of the first 2^+ state for ^{16}C, ^{18}C and ^{20}C [3]. The aim of this thesis is to identify the mixed-symmetry 2^+ state, which is above the neutron separation energy and therefore unbound. Its observation will add weight to our simple picture of describing the neutron-rich C isotopic chain, giving us great insights into the shell evolution towards the neutron dripline at Z=6.

For that purpose, an experiment was carried out at GSI with the R3B/LAND setup in order to investigate the structure of unbound states of ^{16}C, ^{18}C and ^{20}C for the first time via quasi-free scattering (p, 2p) reactions from ^{17}N, ^{19}N, and ^{21}N, respectively.

In this work, the results of the invariant-mass spectroscopy of the one neutron evaporation decay of ^{16}C and ^{18}C are presented, reporting three resonant states located at 5.71(06), 7.83(41) and 9.78(88) MeV for ^{16}C and four unbound states observed at 5.54(10), 7.51(20), 9.83(33) and 12.31(30) MeV for ^{18}C. These unbound states are discussed in comparison with shell model calculations performed with WBP, WBT and WBT* interactions. Preliminary exclusive cross sections are also presented for all of these states.

Contents

List of Figures

List of Tables

This work was mainly funded by the Mexican National Council for Science and Technology (CONACYT) through the scholarship Becas al Extranjero Demanda Libre 2018 - 1, and the Nuclear Physics Group in the Department of Physics, University of York, DAAD and the GET INvolved Programme at GSI.

Declaration

I declare that this thesis is a presentation of original work and I am the sole author. This work has not previously been presented for an award at this, or any other, University. All sources are acknowledged as References.

Chapter 1

Introduction

The nuclear structure was first studied with nuclei that lie in and near to the valley of the β stability and current models are based on those first observations. However, there are only 270 stable isotopes while some models predict up to 7000 radioactive nuclei, the study of which can test the predicting power of the existing models derived from stable and near-stable nuclei.

One of the most challenging but prominent questions in today's nuclear physics is understanding the evolution of structure of nuclei that lie out of the valley of the β stability, where large ratio between the number of protons Z and the number of neutrons N characterise these nuclei. However, thanks to the improved capabilities of radioactive and heavy-ion beam facilities expanding worldwide, it is now feasible to study the structure and phenomena of nuclei on the neutron drip-line and beyond. The aforementioned species of nuclei, called *exotic* nuclei, often exhibit a different behaviour and features never observed in stable nuclei. The differences lie in new quantum phenomena, such as nuclear halos [4], new collective excitation modes, changes in the traditional magic numbers [5], etc.

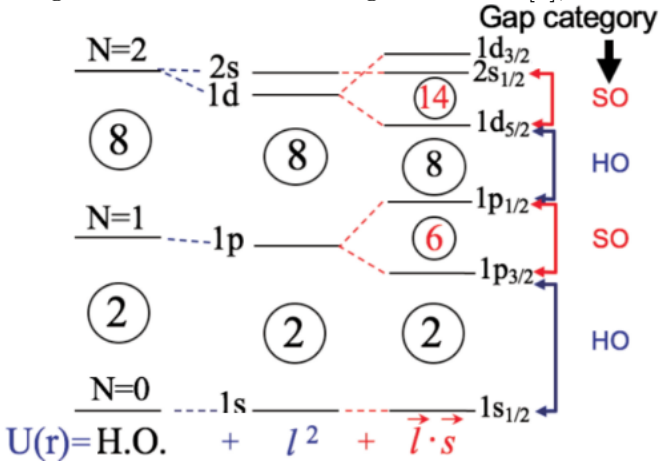

Figure 1.1: Energy level sequence calculated with a harmonic oscillator potential and the spin-orbit term. The first spin-orbit gap is observed at Z=6 between the $1p_{1/2} - 1p_{3/2}$ orbits. Taken from [6]

In particular, neutron-rich carbon isotopes have proved to be an interesting case of study since they have shown to have different shapes and halo structures [7–10]. They also provide information on weak-binding effects due to their small neutron separation energies. In particular, neutron rich carbon isotopes are the perfect testing ground to investigate the first spin-orbit gap between the $1p_{1/2} - 1p_{3/2}$ orbits (see Fig. 1.1) since it has been recently confirmed that there is a weakening in the splitting Z = 6 (see Fig. 1.1) due to influence of the tensor and two-body spin-orbit forces [3].

Recent works have focused on the study of the systematics of the low-lying excited states of neutron-rich carbon isotopes up to ^{20}C. It has been found that the new magic number N=14 observed in neutron rich oxygen isotopes [11] disappears in neutron-rich carbon isotopes [8, 12], which is attributed to the quasi-degenerate character of the levels $s_{1/2}$ and $d_{5/2}$ due to a reduction in the proton-neutron tensor forces.

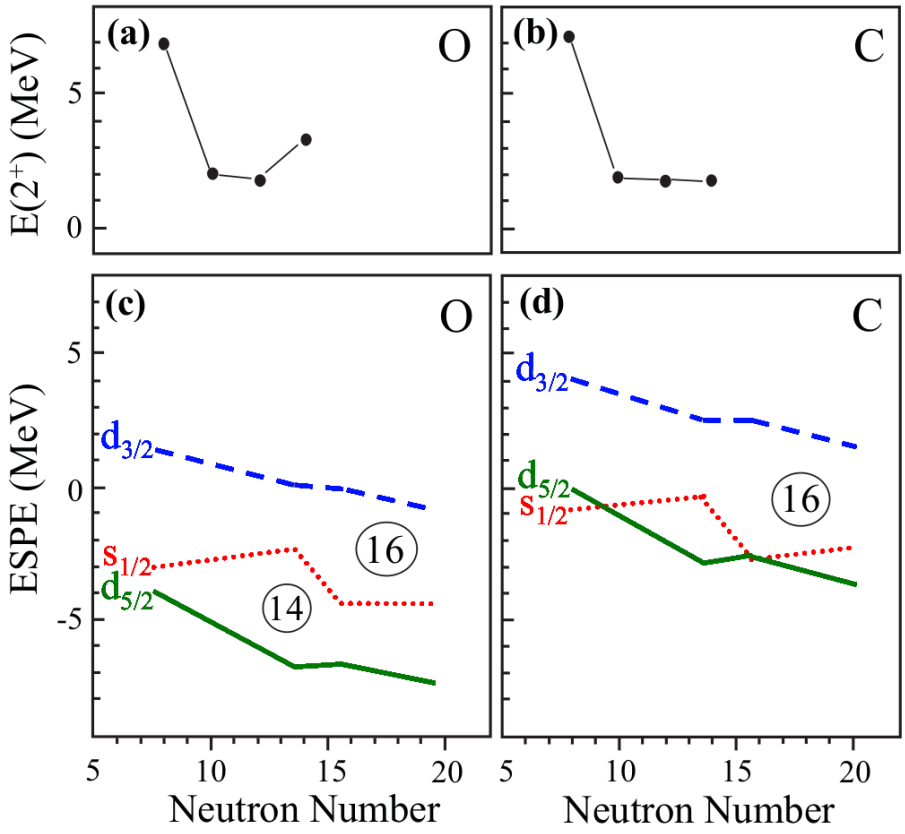

Figure 1.2: Top panels show the evolution of 2_1^+ energies as a function of the neutron number in (a) oxygen and in (b) carbon isotopes. The former presents a rise in the 2_1^+ energy at $N = 16$ that is not observed in the latter. Bottom panels display the evolution of the effective single-particle energies (ESPE) -derived from the WBT interaction- as a function of the neutron number calculated by using the USD effective interaction for the (c) oxygen and (d) carbon isotopes. The subshell gaps that give rise to the new magic numbers N=14 and N=16 observed in neutron-rich oxygen isotopes are narrower in neutron-rich carbon isotopes due to the predicted degeneracy of the $s_{1/2}$ and $d_{5/2}$ orbitals. Figure taken from [12].

Comparing the low-lying 2^+ states of Oxygen and Carbon, we observe that at $N = 8$ we have a shell closure (see Fig. 1.2), and consequently high excitations. In both cases the 2^+ lies at around 7 MeV. Particularly for ^{14}C, it lies at 7012 keV [13], which is evidenced by a transfer reaction study to be proton excitations. Moving towards higher neutron numbers, at $N = 10$, in both O and C, there is a drop in energy of around 6 MeV. The 2^+_1 state of ^{18}O drops to 1982 keV, and similarly, the 2^+ of ^{16}C drops to 1758 keV [14]. The 2^+_1 settles around this value for ^{18}C and ^{20}C, 1588 keV and 1618 keV respectively. This is due to the degeneracy of the $s_{1/2}$ and $d_{5/2}$ observed in carbon, (see (d) in Fig. 1.2), while we see a rise in ^{22}O (N=14, see (c) in Fig. 1.2), and ^{24}O, (N=16, not shown in figure), to 3.20 MeV and 4.79 MeV respectively.

The first 2^+ state in ^{18}O located at 1.982 MeV [13] is considered as the excitation of two neutrons outside the ^{16}O core. Similarly, the first 2^+ in ^{14}C observed at 7.012 MeV [13] is understood as proton excitations of the two proton holes in the ground state. Following the resemblance displayed in Figure 1.3, the first 2^+ state observed in ^{16}C at 1.758 MeV [14] can be interpreted as arising from neutron excitations [3, 15, 16] (as in ^{18}O), while the second 2^+ originated from proton excitations should also be expected around 7 MeV (as in ^{14}C) and, since it is above the S_n=4.250 MeV of ^{16}C, it is therefore unbound.

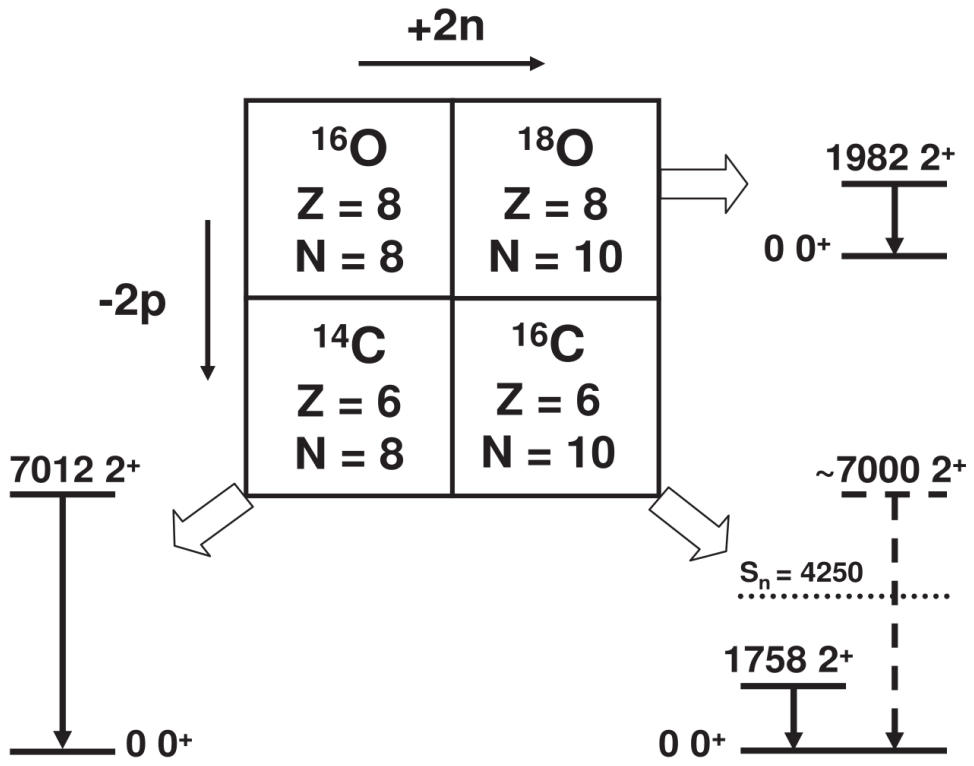

Figure 1.3: Schematic diagram representing the analogy between the 2^+ states in N=8 and N=10 carbon (Z=6) and oxygen (Z=8) isotopes. The 2^+_1 observed in ^{16}C is interpreted as having a similar structure of the 2^+ in ^{18}O, which is a neutron excitation. Their excitation energy reflects the underlying similarities. In the same way, a second 2^+ is expected in ^{16}C around 7 MeV, built on proton excitations like the 2^+_1 in ^{14}C, never measured before. Figure taken from [14]

Given the big gap in energy between the proton excitations and the neutron excitation described above, it is possible to treat the protons and neutrons separately and then to mix them. This concept gives rise to the *configuration mixing*. It is a way to predict realistic states in isotopes by combining two pure states. We use this model to describe the first excited 2^+ state of neutron-rich even-mass carbon isotopes as the mixing of a pure proton (π) and a pure neutron (ν) excitation [17, 18]. The first 2^+ state of ^{16}C has been measured in other works [16, 17] showing it is dominated by neutron excitations and recently confirmed in a quasi-free scattering study that has determined the proton amplitude of the first 2^+ state for ^{16}C, ^{18}C and ^{20}C [3]. The authors used the model of two-state mixing to describe the first excited 2^+ state of the carbon isotopes whose proton amplitude was determined by the ratio of the cross sections corresponding to the first 2^+ and the 0^+ ground state. In order to predict the proton amplitude for ^{18}C and ^{20}C from $B(E2; 2_1^+ \longrightarrow 0_1^+)$ measured values, the authors assumed a two-state mixing of a pure proton and a pure neutron excitation for the first excited state 2^+.

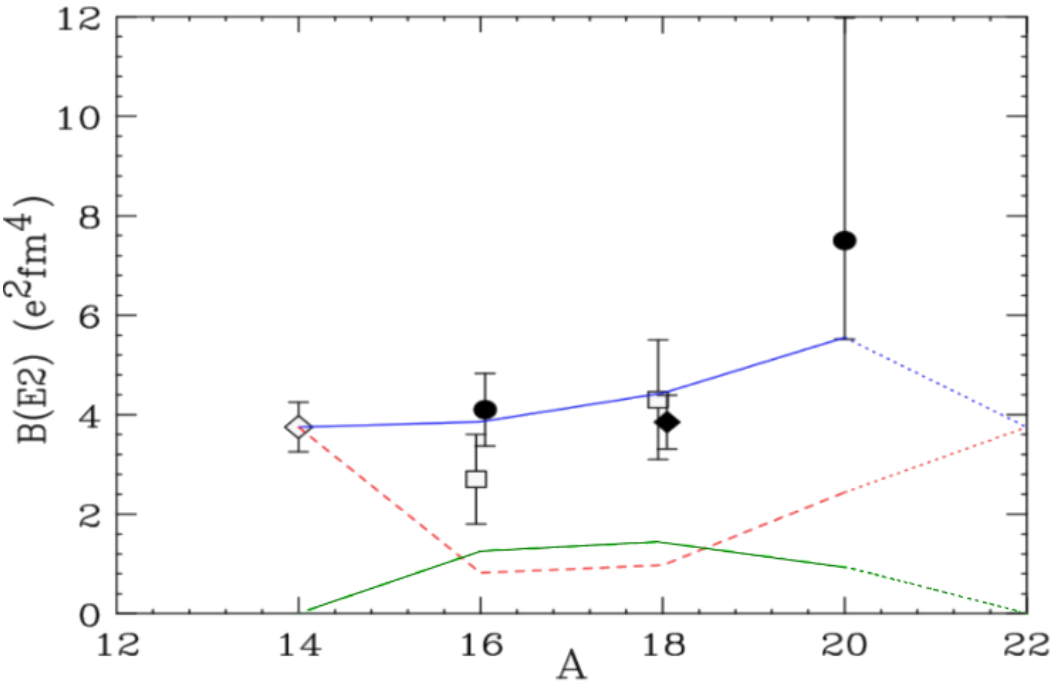

Figure 1.4: Summary of $B(E2)$ experimental values in carbon isotopes. Circles are taken from [15, 17], open diamonds from [19], open squares from [20], and black diamond from [21]. The red line represents the proton component and the green one the neutron component, both in the seniority approach. The blue line is the phenomenological analysis of the $B(E2)$ values. Taken from [18].

A piece of evidence supporting this claim can be provided by the recent measurement of $B(E2)$ values. A. O. Macchiavelli used a seniority inspired scheme to describe the neutron component in the carbon isotopic chain [18]. Experimental measurements of the quadrupole transition strength values from [15, 17, 19–21] were summarised and compared to the contributions from neutrons and protons to the $B(E2)$ in the seniority scheme (see Fig. 1.4).

The obtained proton amplitudes of the 2_1^+ were ∼50%, 11%, 13% and $\gtrsim$30% for ^{14}C, ^{16}C, ^{18}C and ^{20}C respectively. Recently, the authors derived proton amplitudes from the analysis of the experimental cross sections measured for the first 2^+ and the 0^+ ground state of these nuclei. The results showed 10.0%, 7.2%, and $\gtrsim$ 17.0% for ^{16}C, ^{18}C, and ^{20}C respectively. The latest results confirm there is a clear correlation that shows that the increased quadrupole strength is due to the enhanced proton contribution to the 2^+ state in ^{20}C [3] (see Figure 1.5). These small values demonstrate that these 2_1^+ are rather neutron-dominant. However, the well-known increasing parabolic curve of the phenomenological analysis agrees with the increase of the $B(E2)$ values as the mass number also increases, which is proof that although we have neutron-dominant excitations, the proton component is still necessary to reproduce the trend of the experimental measurements.

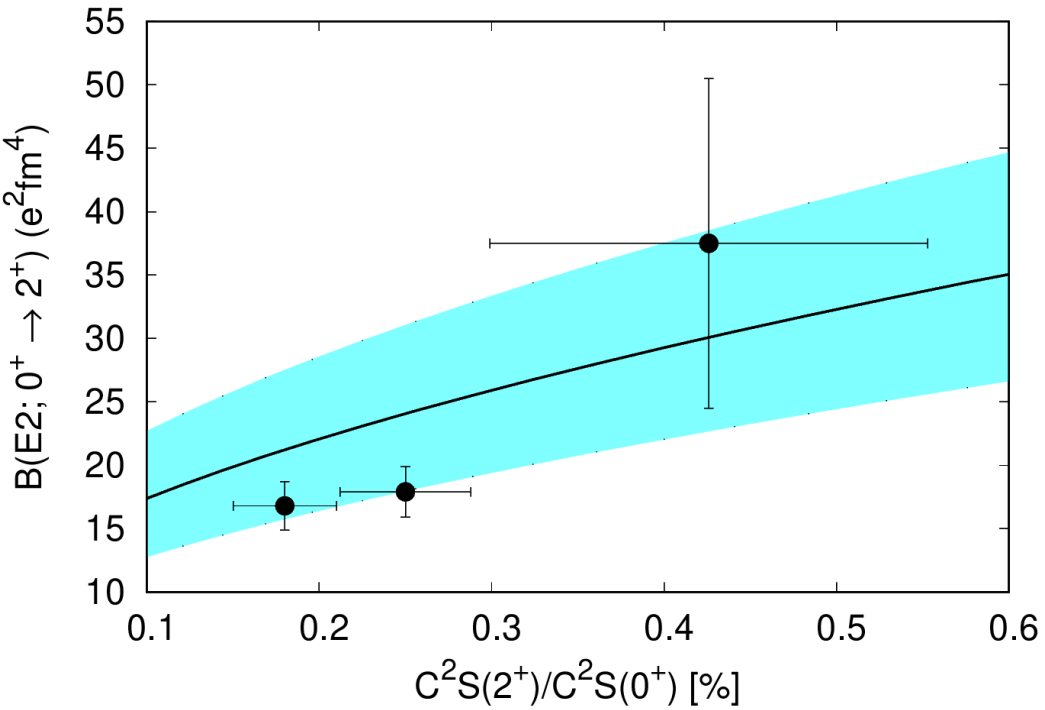

Figure 1.5: Ratio of the spectroscopic factors measured by [3] versus the transition strengths from Ref. [22] for the neutron-rich carbon isotopes ^{16}C, ^{18}C and ^{20}C. The blue shaded area shows the expected limits in the seniority model [18] within one standard deviation, when the proton and neutron $E2$ matrix element are fitted simultaneously to the experimental values of $B(E2)$ and $C^2S(2_1^+)/C^2S(0_1^+)$ for ^{14}C, ^{16}C, ^{18}C and ^{20}C The increase in the $B(E2)$ values is understood as a consequence of the enhanced proton contribution to the 2^+ state in ^{20}C. Taken from [3]

Typically, the first excited state of even-even nuclei decays via electrical quadrupole transition $E2$ from the $2_1^+$to the $0_{g.s.}^+$, and thus, this transition is a benchmark for nuclear structure. A minimum in the $B(E2)$ values together with a high excitation energy of the 2_1^+ is an indication of a shell closure. The $B(E2)$ is at the same time easily affected by the decoupling of protons and neutrons and by small perturbations in the wave function. In recent years, studies on the quadrupole transition strength $B(E2)$ of the first excited 2^+

state have been conducted as well as shell-model calculations in the p shell model space for protons and the sd shell model space for neutrons [1] [15]. The $B(E2; 2_1^+ \rightarrow 0_{g.s}^+)$ strength as well as the level scheme is calculated for ^{16}C, ^{18}C and ^{20}C probing different two-body nucleon-nucleon interactions [23], showing a neutron-dominant nature of the first excited 2^+ state.

The first measurement using the Recoil Shadow Method (RSM) [24] performed by Imai *et al.* [25] showed a quenching in the $B(E2)$ in ^{16}C, which was later corrected by Ong *et al.* [20], and measured also for ^{18}C. The quadrupole transition strength remained nearly constant for ^{14}C, ^{16}C and ^{20}C, hence the expected closed shell nuclei were confirmed and later substantiated through the Recoil Distance Method (RDM) [26, 27] for ^{16}C and ^{18}C in [14, 17, 21].

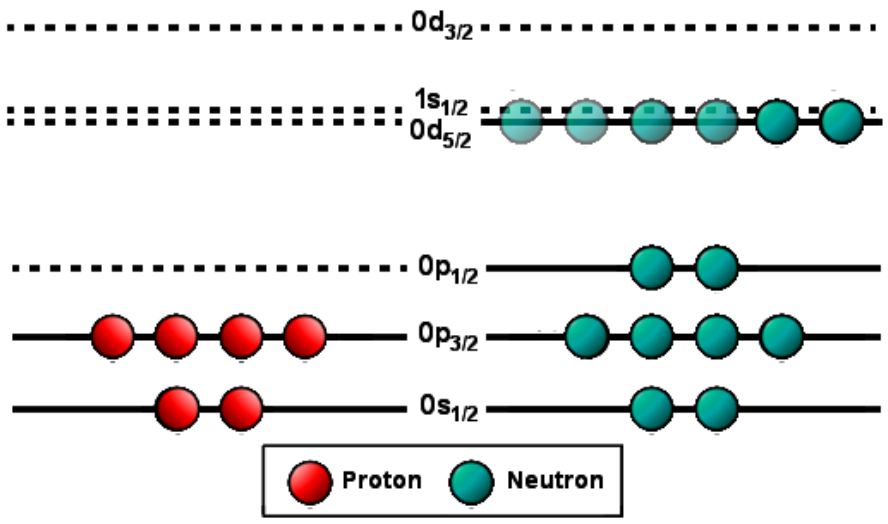

Figure 1.6: Shell structure in neutron-rich carbon isotopes in the independent particle model. The orbits occupied by the protons are shown in red and in green the neutrons. In the $0d_{5/2}$ and $1s_{1/2}$ it is exemplified how the neutrons of ^{16}C, ^{18}C and ^{20}C fill in these orbits.The solid lines represent filled orbits and dashed lines the empty ones.

This experimental study aims to shed new light on the neutron component. We want to identify the mixed-symmetry 2^+ state of ^{16,18,20}C, which is above the neutron separation energy and therefore unbound. We expect to see a strongly populated 2^+ state around 7 MeV (S_{1n}=4.25 MeV for ^{16}C). For that purpose, bound and unbound states in ^{16}C, ^{18}C and ^{20}C have been probed via quasi-free scattering (p, 2p) reactions from ^{17}N, ^{19}N, and ^{21}N beams, respectively. This reaction method was chosen as knock out reactions are the best suited tool to access the $p_{3/2}$ proton component in carbon by removing a proton from a nitrogen (Z=7) beam. In order to populate the 2^+ states the ratio of the spectroscopic factors will be proportional to the proton amplitude by 5/2.

This thesis is organized as follows: Chapter 2 provides a detailed summary of the relevant theory required to discuss this work, including a brief introduction to the current shell model and configuration mixing. Current knowledge of neutron rich carbon isotopes and relevant previous measurements are also presented in this chapter. The details of the experimental setup are shown in Chapter 3, together with the description of the detection systems involved and the radioactive beam production. This chapter includes as well information concerning the electronics, triggers and the data acquisition system. Chapter 4 outlines the data analysis performed starting by the the identification of the incoming and outgoing isotopes, followed by the analysis of the protons from the quasi-free scattering reactions and the γ-rays detected that are used for probing feeding in the analysis of the unbound states unfolded in this thesis. The results are presented and discussed in Chapter 5, including the observed unbound resonances in ^{16}C and ^{18}C.

Chapter 2

Theory

2.1 Liquid Drop Model

Initially, the Liquid Drop Model was proposed by George Gamow [28] in 1930. It describes in a good approximation the spherical quality of a significant number of nuclei but does not accurately reproduce the binding energy around the shell gaps. Mathematically, it was firstly described by Carl F. von Weizsäcker and later optimised by Niels Bohr and John Archibald Wheeler in 1939 with the purpose of unfolding nuclear fission [29]. This derivation gave rise to the *semi-empirical mass formula* or *Bethe-Weizsäcker formula* that thrives to characterise the binding energy, BE as follows:

$$BE = a_V A - a_s A^{2/3} - a_C \frac{Z(Z-1)}{A^{1/3}} - a_A \frac{(A-2Z)^2}{A} \pm \delta(A,Z) \tag{2.1}$$

where Z is the atomic number and A the mass number. Each term corresponds to volume, surface, Coulomb, symmetry and pairing effects respectively.

1. The **volume** term reflects the short-range character of the strong force. The energy term is proportional to A, which proves that a nucleon interacts with the nearest neighbours.

2. The **surface** term accounts for the interaction of the nucleons on the surface of the system with other nucleons inside the nucleus, which is reflected as the reduction of BE proportionally to the surface area of the *drop*.

3. The **Coulomb** term derives from the electromagnetic interaction among protons.

4. The **assymetry** term arises from the Pauli exclusion principle. This allows only two

neutrons or two protons with opposite spin direction in a single energy level.

5. The **pairing** term was obtained from experimental results that indicate that two neutrons or two protons bind more strongly than a single proton with a single neutron.

The derivation of each term can be found in references [30–32]. The first three are derived directly from the liquid drop model, while the latter two terms were included to account for the non collective properties of the nuclei.

Despite adjusting the coefficients a_V, a_S, a_C, a_A and a_P to best reproduce the observed binding energies, the semi-empirical mass formula does not completely reproduce the local maxima in the B/A experimental data, see Figure 2.1. This suggests that nuclei are more tightly bound than what was predicted by the liquid drop model for certain number of protons and neutrons known as *magic numbers*. This observation represents the first piece of evidence of internal structure within the nucleus, leading to the nuclear shell model.

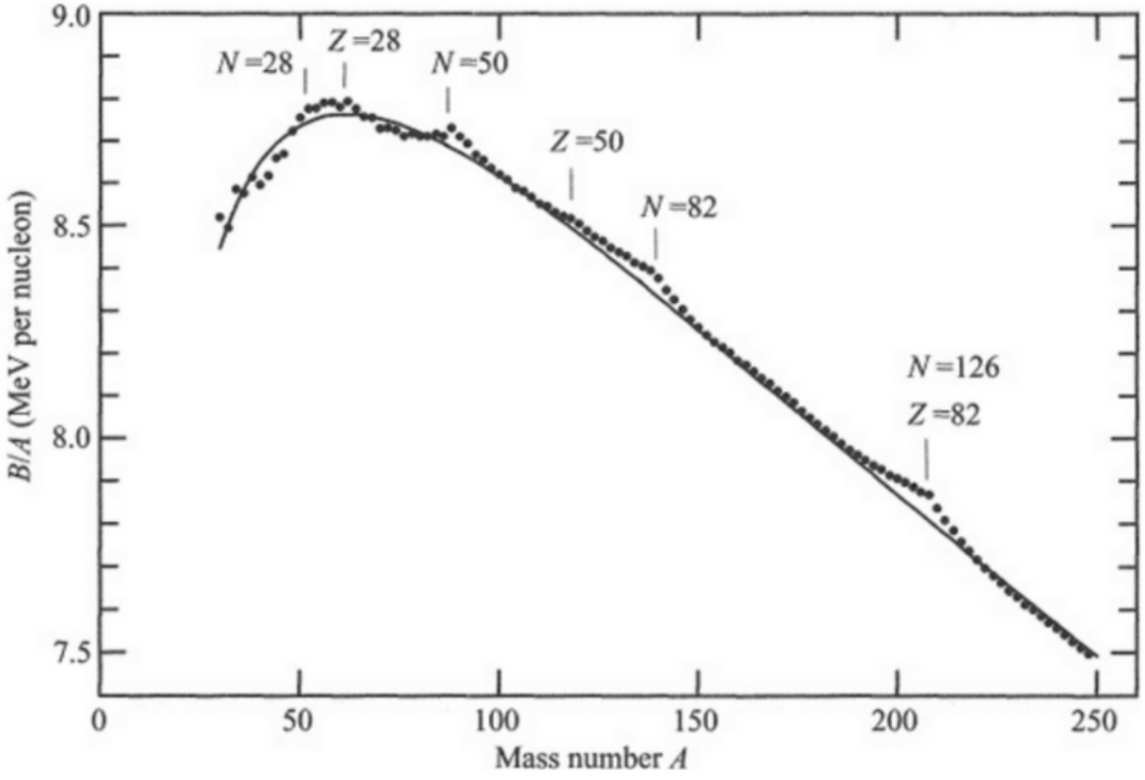

Figure 2.1: Semi-empirical mass formula predictions for the binding energy per nucleon, B/A, as a function of mass number, A, with $a_V = 15.56MeV$, $a_S = 17.23MeV$, $a_C = 0.7MeV$ and $a_A = 23.28MeV$, for odd-even nuclei so that there is no pairing effect. Experimental values are represented by points [31].

2.2 Nuclear Shell Model

In 1932, James H. Bartlett introduced the first hypothesis of the shell structure within the nuclei [33], explaining with a model akin to Bohr model the increased stability of ^{4}He and ^{16}O, and thus, the first recognition of the *magic numbers*, 2 and 8. One year later, W. Elsasser suggested a model in which the nucleons fill discrete energy levels due to an effective potential well created by the rest of nucleons in a system [34]. Unfortunately, this model was rejected due to a lack of experimental evidence.

Nearly two decades later, in 1948, Maria Goeppert-Mayer observed that nuclei around closed shells at Z=50, 82 and N=50, 82, 126 were particularly stable [35], yet she was unable to describe higher shell closures. The following year, in 1949, Mayer [36] and Haxel *et al.* [37] were able to reproduce the shell closures by introducing the spin-orbit coupling to the potential well. The successful description meant a breakthrough in nuclear theory and the magic numbers become a benchmark in the characterisation of nuclear structure.

2.2.1 Mean field model

The nuclear force acts between protons and neutrons binding the nucleus, it is charge symmetric and charge independent and powerfully attractive at short range but quickly becomes negligible (beyond 3-4fm).

The energy levels a nucleon can occupy in a nucleus are a solution of the Schrödinger equation governed by the potential generated by the nuclear interaction with the other nucleons inside the nucleus:

$$\left[-\frac{\hbar^2}{2m}\nabla^2 + V(\vec{r})\right]\psi(\vec{r}) = E\psi(\vec{r}) \tag{2.2}$$

where m is the mass of the nucleon, E is the energy, $\psi(\vec{r})$ is the wave function of the nucleon, and $V(\vec{r})$ is the potential the nucleon undergoes.

The potential mentioned above, usually called *effective* potential, $V_{eff}(r)$, describes the effects of the neighbouring nucleons on a single nucleon. It is comprised of the central nuclear potential $V_0(r)$, the contribution of the spin-orbit coupling $V_{so}(r)$, the Coulomb potential $V_C(r)$ and a centrifugal term.

$$V_{eff}(r) = V_0(r) + V_{so}(r)\vec{l}\cdot\vec{s} + V_C(r) + \frac{l(l+1)\hbar^2}{2mr^2} \tag{2.3}$$

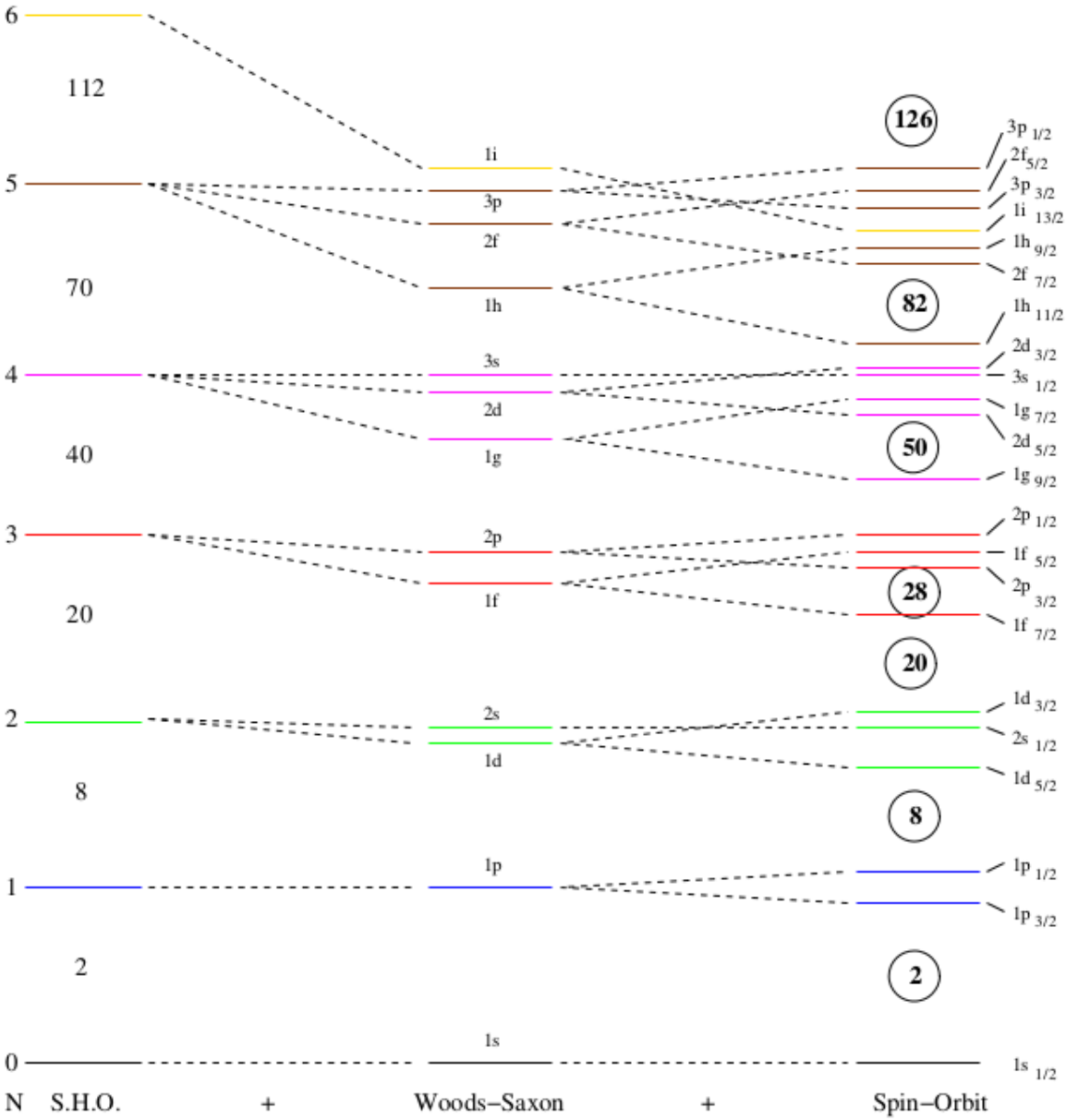

Figure 2.2: Energy level sequence calculated for several potentials. From left to right the spherical harmonic oscillator and the Woods-Saxon potential without and with the spin-orbit term. The levels are tagged with the corresponding quantum numbers nlj, *and their degeneracy is given by* 2j+1. *When several energy levels lie close together they form a nuclear shell, the gaps between these shells are labelled with the corresponding magic numbers.*

Unfortunately, there is no analytic description of the strong interaction responsible for the nuclear force that can be used for the nuclear potential. Therefore, one of the most common approaches is to describe central potential with an harmonic oscillator potential:

$$V_0^{SHO}(r) = \frac{1}{2} m\omega^2 r^2 \tag{2.4}$$

where m is the mass of the nucleon in the potential, and ω the eigenfrequency.

However, a potential that goes smoothly to zero has been more successful reproducing observation (see Fig. 2.2). The most usual form being the so-called Woods-Saxon [38], which is a spherical symmetric potential that decreases asymptotically to zero as r increases, somehow linked to the Fermi-Dirac distribution of the nucleons in the nucleus, is expressed as:

$$V_0^{WS}(r) = \frac{-V_0}{1 + \exp\left(\frac{r-R}{a_0}\right)} \tag{2.5}$$

where R is the nuclear radius $R = r_0 A^{1/3}$, a_0 is the diffuseness of the nuclear surface and V_0 is the potential well depth, which is adjusted to reproduce the binding energies.

The spin-orbit component is expressed as $V_{so}(r)\vec{l} \cdot \vec{s}$ and its intensity proportional to the derivative of the central potential:

$$V_{so}(r) = V_{so} \frac{1}{r} \frac{dV_0^{WS}(r)}{dr} \tag{2.6}$$

where V_{so} defines the depth of the spin-orbit coupling, typically ~ 6 MeV.

The Coulomb potential is derived assuming uniform charge distribution over a sphere the size of the nucleus.

$$V_C(r) = \begin{cases} \dfrac{ke^2(Z-1)}{2R_C}\left(3 - \left(\dfrac{r}{R_C}\right)^2\right) & r \leq R_C \\ \dfrac{ke^2(Z-1)}{r} & r > R_C \end{cases} \tag{2.7}$$

where k is the Coulomb constant, e is the electron charge ($ke^2 = 1.44$ MeV fm) and R_C is the Coulomb radius, $R_C = r_C A^{1/3}$. Tradiotionally $R_0 = R_C$ is accepted.

Finally, the centrifugal term is required to account for the influence of the relative angular momentum between the nucleon and the nucleus itself.

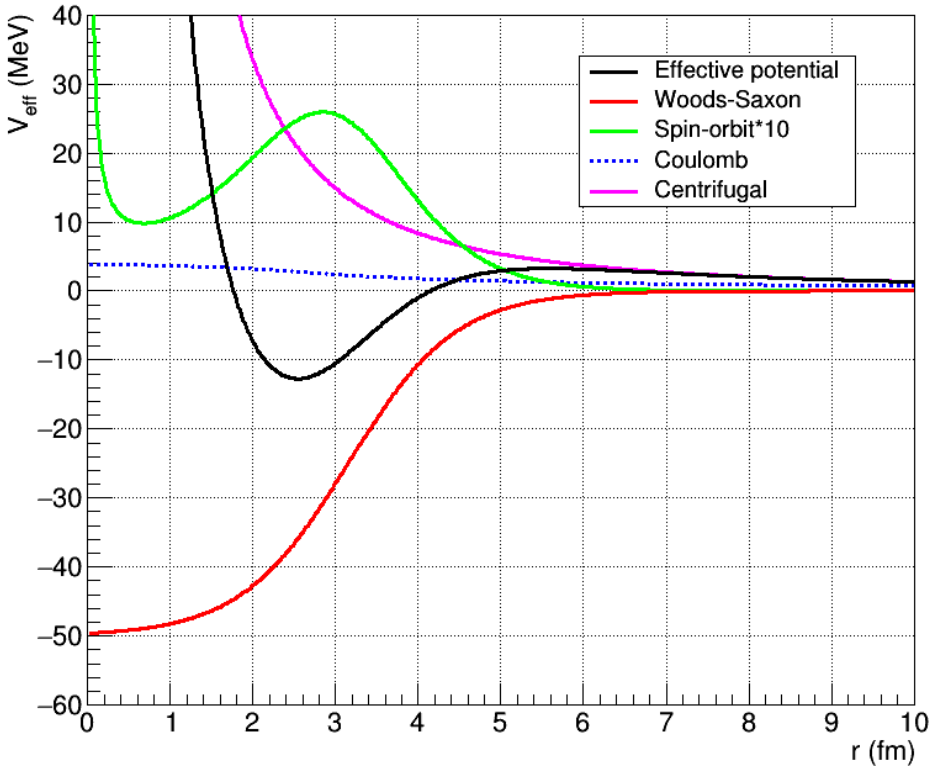

Figure 2.3: Effective potential for ^{16}C (black), and the different components: in red the nuclear mean-field depicted with a Woods-Saxon (V_0=50 MeV, r_0=1.25 fm, a_0=0.65 fm), The spin-orbit term in green (V_{so}=6 MeV, multiplied by 10 to enhance the details). In pink is shown the centrifugal contribution and the blue dashed line indicates the Coulomb effect expected if the particle was a proton instead of a neutron.

Since nuclei obey the laws of quantum mechanics, solving the Schrödinger equation (Eq. 2.2) using the effective potential $V_{eff}(r)$ (see Eq. 2.3) for either a single proton or a neutron moving in a potential well, we will have solutions only for certain values of energy that correspond to the *single-particle states*, which determine the energy levels that a nucleon can populate.

2.2.2 Configuration mixing

The single-particle model (SPM) properly describe spins and parities for spherical nuclei under the hypothesis that all nucleons but one are paired. So for those nuclei with more than one valence nucleon, the shell model predictions deviate from observations. In these situations, the nucleons from an unfilled shell are handled by adding a *residual interaction* to the single-particle Hamiltonian, which will include pairing effects between valence nucleons and NN interactions, so then the Hamiltonian would be:

$$H = H_{SPM} + H_{res} \tag{2.8}$$

This residual interaction can be understood as a perturbation on the effective potential V_{eff} that gives way to the single-particle states to combine, leading to an effect called *configuration mixing*.

The model of the configuration mixing represents a way to predict realistic states in isotopes by combining two pure single-particle states. We use it to describe the first excited 2^+ state of neutron-rich even-mass carbon isotopes as the mixing of a pure proton (π) and a pure neutron (ν) excitation [17, 18].

Moreover, the strength of the residual interaction strongly relies on the overlap between the wave function of the valence nucleon and the wave function of the lower-lying nucleons in the closed shells.

2.2.2.1 Two-state mixing

The mixing of two basis states $|\phi_1\rangle$ and $|\phi_2\rangle$ with energies E_1 and E_2 depends on two variables only: the difference in energy between unperturbed states $\Delta E_u = E_1 - E_2$ and the strength of the mixing interaction V. The mixing ratio is therefore defined as:

$$R = \frac{\Delta E_u}{V} = \frac{E_1 - E_2}{V} \tag{2.9}$$

The final energies and wave functions are obtained by diagonalising the matrix:

$$\begin{pmatrix} E_1 & V \\ V & E_2 \end{pmatrix} \tag{2.10}$$

The final energies are E_I and E_{II} and the respective wave functions, denoted by $|\psi_I\rangle$ and $|\psi_{II}\rangle$, [39] are given by:

$$|\psi_I\rangle = \alpha|\phi_1\rangle + \beta|\phi_2\rangle \tag{2.11}$$

$$|\psi_{II}\rangle = -\beta|\phi_1\rangle + \alpha|\phi_2\rangle \tag{2.12}$$

with the mixing amplitudes α and β of neutron and proton, respectively, satisfying the following equivalences:

$$\alpha^2 + \beta^2 = 1 \tag{2.13}$$

$$\beta = \left(\sqrt{1 + \left(\frac{R}{2} + \sqrt{1 + \frac{R^2}{4}} \right)^2} \right)^{-1} \tag{2.14}$$

Finally, the energies of the mixed states are:

$$E_{I,II} = \frac{1}{2}(E_1 + E_2) \mp \frac{\Delta E_u}{2}\sqrt{1 + \frac{4}{R^2}} \tag{2.15}$$

A schematic representation of the mathematical derivation of the two state mixing is presented in Figure 2.4, where the unperturbed states $|\phi_1\rangle$ and $|\phi_2\rangle$ are shown on the left and the mixed states $|\psi_I\rangle$ and $|\psi_{II}\rangle$ are on the right.

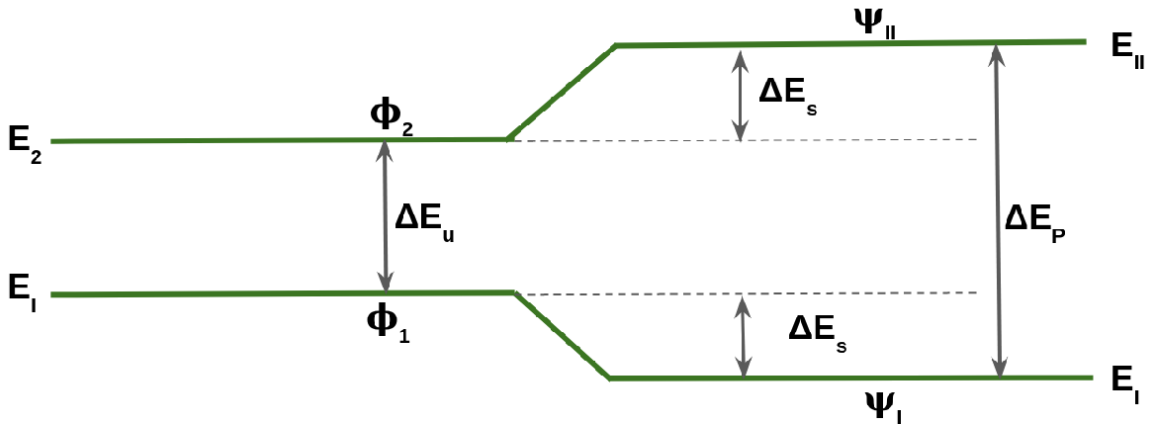

Figure 2.4: Schematic diagram of two-state mixing configuration, showing the initial states $|\phi_1\rangle$ and $|\phi_2\rangle$ on the left and the mixed final states $|\psi_I\rangle$ and $|\psi_{II}\rangle$ are on the right. Scheme based on [39]

Now the general basis for two state mixing have been introduced, we can discuss two extreme cases. First lets consider the mixing of two states completely degenerate, i.e. $E_1 = E_2 = E_0$ and therefore $\Delta E_u = 0$. This results in strong mixing where the mixing amplitudes become $\alpha = \beta = 1/\sqrt{2}$, which means that both states are completely mixed, with their energies being:

$$E_{I,II} = E_0 \mp V \tag{2.16}$$

from this we learn that the smallest energy gap between perturbed final states ΔE_p is twice the interaction strength V.

On the other hand we have the opposite case of weak mixing, where the matrix element of the interaction strength V is significantly smaller than the energy difference between the unperturbed states ΔE_u, i.e. $V \ll \Delta E_u$. In this case, the mixing amplitude β is given by $\beta \approx 1/R$ and the difference between the initial states $|\phi_1\rangle$, $|\phi_2\rangle$ and the resulting mixed states $|\psi_I\rangle$, $|\psi_{II}\rangle$, is small, $\Delta E_s \approx 0$, and hence the gap remains almost the same after the mixing $\Delta E_u \approx \Delta E_p$.

$$\beta \approx \frac{1}{R} = \frac{V}{\Delta E_u} \quad \Rightarrow \quad V \approx \beta \Delta E_u \approx \beta \Delta E_p \tag{2.17}$$

2.2.2.2 Spectroscopic factors

Within the context of configuration mixing, we need to assess the single-particle strength carried by a state in a given nucleus. The spectroscopic factors C^2S are introduced to fulfil this need, and hence are defined as the overlap integral between the wave function in the entrance channel and in the exit channel.

As an example, in case of the ^{17}N→^{16}C* system, the spectroscopic factors provide a measure of the overlap between the initial state in the beam particle ^{17}N and the state populated in ^{16}C coupled to the knocked out proton in the corresponding orbital. The spectroscopic factor value would be 1 in the ideal scenario of removing a single nucleon occupying alone a pure single particle orbital.

Theoretical cross sections are calculated for pure single-particle states. As discussed previously, the nuclear structure is often more complicated than a pure single particle state and the experimental cross section will in general be different from theoretical predictions by a certain factor. This normalisation factor between theoretical and experimental cross sections is the spectroscopic factors, and accounts for the effect of the nuclear structure in the cross section:

$$\left(\frac{d\sigma}{d\Omega}\right)_{exp} = C^2S \left(\frac{d\sigma}{d\Omega}\right)_{th} \tag{2.18}$$

2.3 Shell Evolution

For many years, the classical magic numbers 2, 8, 20, 28, 50, 82 and 126 were deemed as fixed. Opportunely, the recent development of radioactive ion beam facilities have allowed us to probe the impact of large ratios between N and Z in the nuclear structure of very neutron-rich systems by studying experimentally more exotic regions of the nuclide chart. Evidence emerged denying the permanent quality of the aforementioned magic numbers, as the results showed that as we go further from the valley of stability the magic numbers seem to change. This fixed character of the traditional magic numbers was abandoned, and since then the exotic nuclei have become of great interest when searching for the underlying reason of these structural changes, which are not yet fully understood.

Since the nuclear mean field model is angular momentum and spin dependent, we can say that the nucleon-nucleon interaction influences the shell evolution. In addition, features of the nuclear interaction, which are barely influential stable nuclei, such as pairing or coupling between bound states and continuum, can have a significant impact in weakly bound nuclei..

2.3.1 Subshell closure $Z = 6$

In her Nobel Lectures, Maria Goeppert Mayer presentend two different series of magic numbers. The first series: 2, 8, 20 and 40 attributed to the harmonic oscillator potential, while the second one: 6, 14, 28, 50, 82 and 126 arises from the spin orbit coupling. However, she described 6 and 14 as *"hardly noticeable"* acknowledging that the energy gap between the $1p_{1/2}$ and $1p_{3/2}$ orbitals due to the spin-orbit is fairly small [40].

However, recent experimental and theoretical works have suggested the possible existence of a new magic number 6 in $N = 6$ isotones, ^{8}He and ^{14}O, and $Z = 6$ nucleus ^{14}C. The proton subshell closure at $Z = 6$ in neutron-rich even-even carbon isotopes is substantiated by the small $B(E2)$ values observed in ^{14}C to ^{20}C [14, 20, 22].

Magic numbers of protons or neutrons are associated with shell closures and confer the nuclei a particularly stable configuration due to the difficulty of breaking a closed shell and exciting a nucleon across a major shell gap. Thus the level scheme of magic nuclei is characterised for a lack of low-lying excited states. Therefore, the systematics of the energy of the first excited state as a function of the number of protons and neutrons is expected to show local maxima for magic numbers, providing an indication of where the new magic numbers could lie.

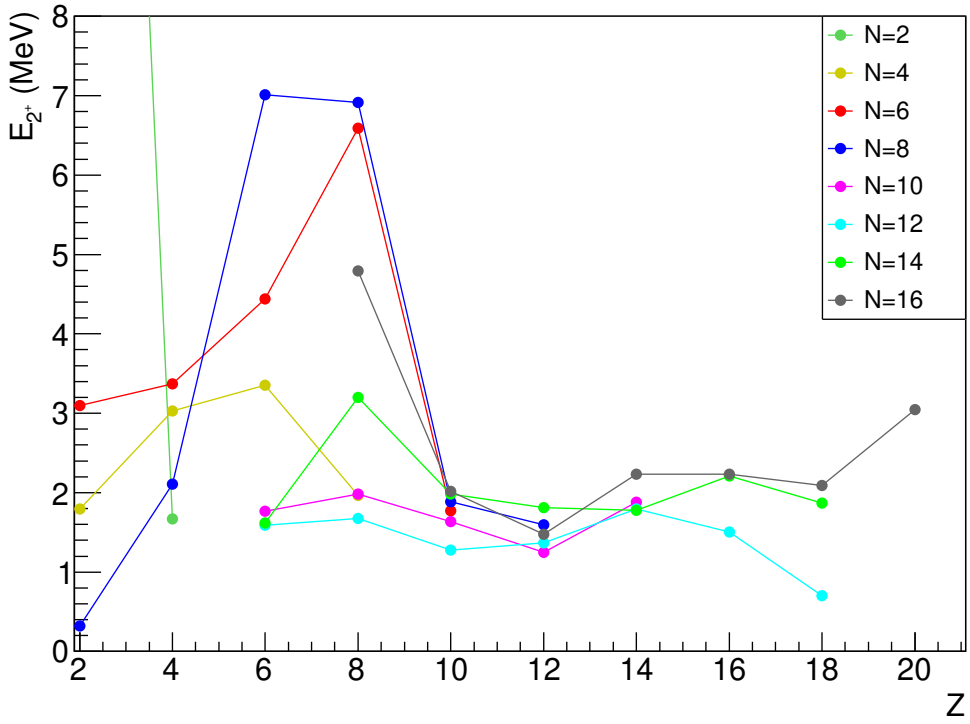

Figure 2.5: Proton number dependence of the energy of the first 2^+ state for even-even nuclei with $N < 17$, where it can be seen that it lies at high excitation energy at the traditional magic Z=8. Also, there are noticeable high excitations at Z=6 for the N=4, 6 and 8, and isotonic chains.

2.3.2 Subshell closure $N = 16$

The very first indication of a new magic number at N=16 lies at plain sight in the nuclide chart. If we observe the neutron dripline for light nuclei, we can see that the last bound isotope of carbon, nitrogen and oxygen ($Z = 6$, 7 and 8) coincide at N=16, but the addition of a single proton suddenly allows the binding of 6 additional neutrons, moving the dripline up to $N = 22$.

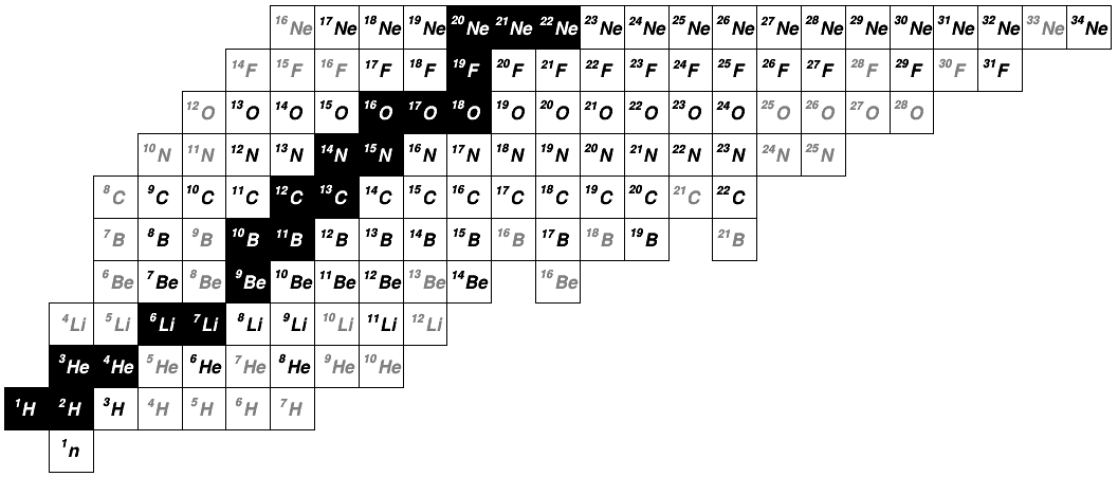

Figure 2.6: Nuclide chart for nuclei up to Z=10, where we can see the sharp extension of the dripline at Z=9, going from ^{24}O (N=16) to ^{31}F (N=22).Unbound nuclei are shown in light grey.

The first experimental evidence of the emergence of the $N = 16$ shell closure was observed by Ozawa *et al.* by analysing the dependence of the neutron separation energies (S_n) and the interaction cross-sections (σ_I) on the neutron number N in light neutron-rich isotopes [41]. Since the neutron after a shell closure is anticipated to be weakly bound, a magic number is expected to show as a break in the neutron separation energy trend. The observation of a break at N=16 for Z=8 indicates the emergence of a new magic number.

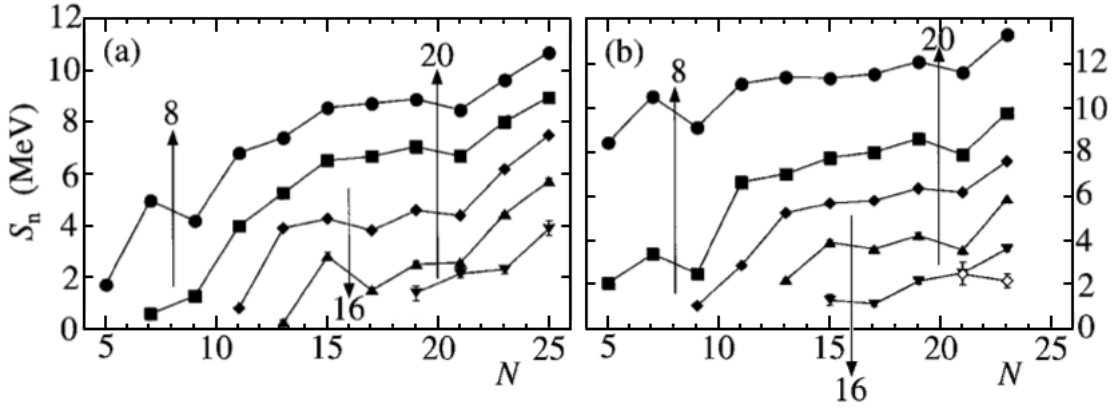

Figure 2.7: Neutron separation energies as a function of N for odd-A even-Z (left) and odd-odd nuclei (right). Each line represent a different isospin number T_z from 1/2 to 9/2 (left) and 0 to 5 (right). Figure adapted from [41].

Figure 2.8 shows the trend of the energy of the first excited state of even-even nuclei for different isotopic chains with the number of neutrons N. It can be clearly seen both the vanishing of the traditional magic number N=20 and the emergence of a new subshell closure at N=16: The maxima observed at N=20 for S and Si isotopic chain slowly disappears at the same time that a new peak appears at N=16 when going from stable ^{32}S to the neutron dripline ^{24}O nucleus.

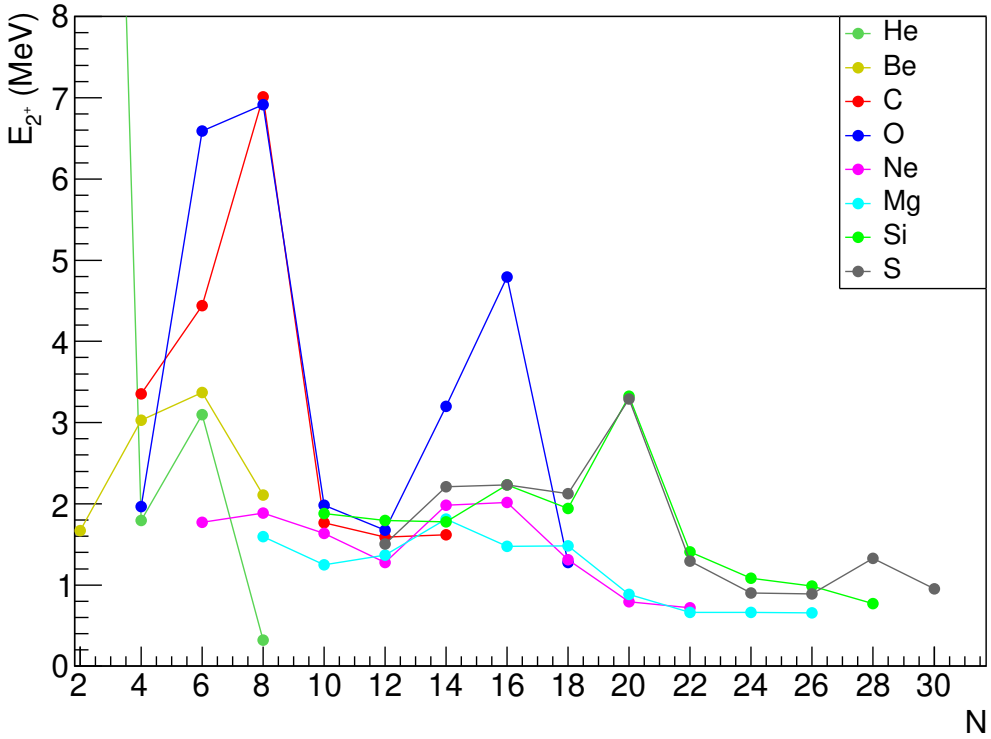

Figure 2.8: Neutron number dependence of the energy of the first 2^+ state for even-even nuclei with Z< 17, whereby the traditional magic number N=20 for sulfur and silicon suddenly disappears when moving down to magnesium. Instead a small maximum appears at N=16 for neon to finally observe a clear peak at N=16 in oxygen.

This behaviour is often explained through the existence of a nucleon-nucleon tensor force acting between protons and nucleons in orbitals with the same angular momentum ℓ, but with a strong spin-isospin dependency that acts between nucleons in orbits with opposite spin s. Hence, when going from sulfur and silicon, Z=14 and 16 respectively, both with a full $\pi d_{5/2}$ orbital towards oxygen, Z=8, and an empty $\pi d_{5/2}$ orbital, the strength of this NN tensor force on the $\nu d_{3/2}$ orbit decreases with the population of the $\pi d_{5/2}$ orbital until it finally disappears when it is empty for oxygen. Therefore the $\nu d_{3/2}$ orbit rises towards the fp-shell, increasing the $N = 16$ gap and reducing the $N = 20$ gap.

2.3.3 Subshell closure $N = 14$

Maxima at N=20 for sulfur and silicon and N=16 for oxygen observed in Figure 2.8 quickly catch all the attention, but if we look more closely we can see that the excitation energy of ^{22}O (N=14) is comparable to that of ^{30}Si and ^{32}S (N=20). This presents N=14 as a new magic number candidate for neutron-rich isotopes, later confirmed experimentally by Staniou *et al.* deducing a large gap in the effective single particle energies in ^{22}O at N=14 [11].

The mechanism leading to the emergence of the N=14 subshell gap in oxygen can be understood in the light of Figure 1.2, where we can see that the N=14 gap grows as the $\nu d_{5/2}$ orbit is filled since the tensor force between like-nucleons is globally attractive. At the same time, the $\nu s_{1/2}$ orbit moves towards higher excitation energies because the NN interaction is repulsive in this case.

However, experimental observation has shown that the N=14 subshell closure disappears in neutron-rich carbon isotopes [8, 12] due to the inversion of the $\nu d_{5/2}$ and $\nu s_{1/2}$ single particle orbitals that makes them quasi-degenerate.

2.4 Proton amplitude

As mentioned before, the concept of configuration mixing will be used to describe the first 2^+ state in even-even neutron-rich carbon isotopes as the mixing of two states, one arising from proton excitations and a second due to neutron excitations [18].

The shell model describes the wave function of the 0^+ ground state in ^{16}C, ^{18}C, and ^{20}C as

$$\begin{aligned} |0^+_{gs};\, ^{\mathrm{A}}\mathrm{C}\rangle = \gamma\ &|\nu\,(sd)^n; J=0\rangle \otimes |\pi\,(1p_{3/2})^4; J=0\rangle \\ &+ \delta\ |\nu\,(sd)^n; J=2\rangle \otimes |\pi\,(1p_{3/2})^4; J=2\rangle \end{aligned} \tag{2.19}$$

with $n = 2, 4, 6$ neutrons for ^{16}C, ^{18}C, and ^{20}C, respectively, with the n valence neutrons occupying a quasi-degenerate *sd* shell [12], as shown in Figure 1.6. Since a higher excitation energy is required for the second term, it is expected that the first term will be the dominant contribution to the wavefunction of the ground state, and therefore we can safely assume $\gamma = 1$ and $\delta = 0$.

Analogously, the first 2^+ excited state can be described as:

$$\begin{aligned} |2^+_1;\, ^{\mathrm{A}}\mathrm{C}\rangle = \alpha\ &|\nu\,(sd)^n; J=2\rangle \otimes |\pi\,(1p_{3/2})^4; J=0\rangle \\ &+ \beta\ |\nu\,(sd)^n; J=0\rangle \otimes |\pi\,(1p_{3/2})^3(1p_{1/2})^1; J=2\rangle \end{aligned} \tag{2.20}$$

In the last equation, α and β are the mixing amplitudes discussed in the two-state mixing formalism presented in Section 2.2.2.1, which in this case represent the amount of pure neutron and pure proton excitation contributing to the first 2^+ state configuration, respectively.

The so-called proton amplitude β can be probed via one-proton knockout reactions induced with nitrogen beams. This can be understood by looking at the wave function of their ground state:

$$|1/2^-_{gs};\, ^{\mathrm{A+1}}\mathrm{N}\rangle = \; |\nu\,(sd)^n; J=0\rangle \otimes |\pi\,(1p_{3/2})^4(1p_{1/2})^1; J=1/2\rangle \tag{2.21}$$

where we can see that the removal of a proton from the $1p_{3/2}$ orbit in the $1/2^-$ ground state in odd-mass nitrogen isotopes cannot populate the neutron component of the first 2^+ state in neutron-rich even-even carbon isotopes, but can only populate the proton component.

It is worth saying, however, that the removal of the proton from the $1p_{1/2}$ orbit in the $1/2^-$ ground state $^{A+1}$N will populate the 0^+ ground state in ^{A}C. In this particular case, the spectroscopic factor is expected to be close to 1, as discussed previously in 2.2.2.2, since we are removing the only proton populating the $1p_{1/2}$ orbital. However, when a proton is knocked out from the $1p_{3/2}$ orbital, and the 4 remaining protons in the $1p_{3/2}$ and $1p_{1/2}$ orbitals couple to a 2^+ state, which happens in 5 out of 8 times, the spectroscopic factor is proportional to the proton amplitude:

$$\begin{aligned} C^2S\left(0^+_{gs}\right) &\approx 1 \\ C^2S\left(2^+_1\right) &\approx \beta^2\, 4\,\frac{5}{8} = \beta^2\,\frac{5}{2} \end{aligned} \tag{2.22}$$

Using the Equation 2.18 that connects the spectroscopic factors with the cross sections, we can derive a similar relathionship between the experimental cross section of the ground state and the first 2^+ state:

$$\frac{C^2S\left(2^+_1\right)}{C^2S\left(0^+_{gs}\right)} \approx \beta^2\,\frac{5}{2} \quad \Rightarrow \quad \frac{\sigma_{exp}\left(2^+_1\right)}{\sigma_{exp}\left(0^+_{gs}\right)} \approx \beta^2\,\frac{5}{2}\frac{\sigma_{th}\left(2^+_1\right)}{\sigma_{th}\left(0^+_{gs}\right)} \tag{2.23}$$

Let's not forget that, when mixing two states, we also obtain two mixed states, and therefore a second 2^+ excited state of mixed-symmetry character between pure proton and pure neutron excitations is expected:

$$\begin{aligned} |2^+_2;\, ^{\mathrm{A}}\mathrm{C}\rangle = &-\beta\; |\nu\,(sd)^n; J=2\rangle \otimes |\pi\,(1p_{3/2})^4; J=0\rangle \\ &+\alpha\; |\nu\,(sd)^n; J=0\rangle \otimes |\pi\,(1p_{3/2})^3(p_{1/2})^1; J=2\rangle \end{aligned} \tag{2.24}$$

In this case, the proton amplitude being α and following a similar derivation we can conclude that the experimental cross section would be proportional to α^2. While there is a relatively small contribution of proton excitations in the first 2^+ state, the second 2^+ state is expected to be dominated by the proton component.

If we assume a relatively weak mixing, the energy of the mixed-symmetry states remains similar to the energy of the unperturbed states, which can be estimated by comparison with ^{14}C and ^{18}O (see Figure 1.3), located at 7.012 and 1.982 MeV and caused mostly due to proton and neutron excitation respectively. Hence, the second 2^+ state we are interested in is to be expected around 7 MeV, as discussed by Wiedeking *et al.* [14].

2.5 Reaction mechanism

We can distinguish two main types of nuclear reactions according to the time frame of the interaction: direct reactions and compound-nucleus reactions. In compound-nucleus reactions, beam particle and target nuclei fuse into a highly excited nucleus, so-called *compound nucleus*, that remains bound long enough (10^{-16} - 10^{-18} s) for its excitation energy to spread out among its nucleons. Therefore, its decay mode does not depend on the entrance channel.

Direct reactions, on the other hand, are quick processes (10^{-22} s) that happen in a single step involving just a few nucleons in the nuclear surface while the others are largely unaffected, behaving as spectators. Due to the much shorter time scale of the interaction, momentum transferred and excitation energy are relatively small and hence this reaction mechanism only populates low-lying excited states.

The products of a direct reaction depends on what type of reaction is observed: the most common reaction is *elastic* scattering, when the beam and target nuclei remain in their ground state. If one or both nuclei become excited, it is then *inelastic* scattering. We can also have *break-up* reactions, when the beam particle is fragmented in different lighter nuclei, and *transfer* reactions, widely mentioned in the introduction, when one or several nucleons are transferred from one nucleus to the other. However, the most important type of direct reaction for this work are *knock-out* reactions, in which one or more nucleons are removed from the beam particle.

2.5.1 One-nucleon knockout reactions

Direct reactions that transfer or remove a single nucleon are excellent experimental tools to probe single-particle orbitals and orbital occupancies. In particular, single-nucleon knockout reactions have high sensitivity to produce hole-states. Due to the nature of the reaction, the momentum distribution of the knockout residue allows to determine the orbital angular

momentum of the nucleon removed from comparison with reaction calculations based on the eikonal method (see Section 2.5.1.1).

In exotic nuclei near the neutron dripline, with large neutron excess and small neutron separation energies, weak binding effects can make the wavefunction of one or more neutrons to be extended, sometimes far beyond the range of the strong force forming neutron halo. The peripheral character of knockout reactions that makes them specially sensitive to the external part of the nucleons wavefunction, can provide insight on how the long-range components of the nucleon-nucleon interaction influence nuclear structure.

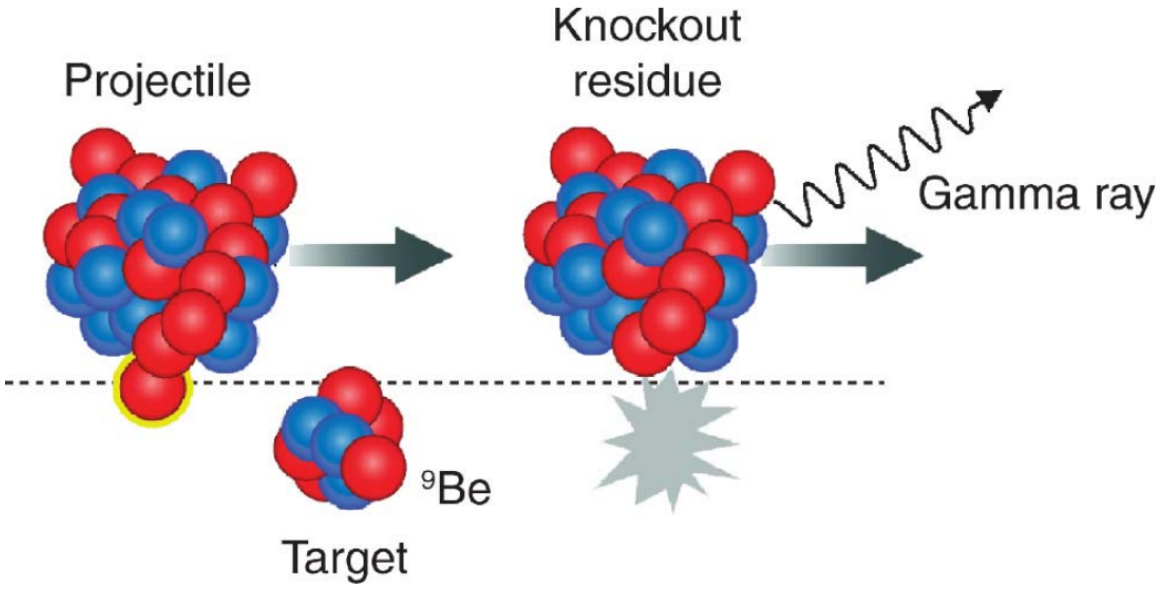

Figure 2.9: Diagram of a one-nucleon knockout reaction on a beryllium target, whereby a single nucleon is removed from the beam particle in a peripheral collision with the target nucleus. Taken from [42].

One-nucleon knock-out reactions are traditionally classified in two main groups: elastic breakup or diffraction and inelastic breakup or stripping (see Figure 2.10). In the former, the target remains in the ground state while the removed nucleon is emitted in forward direction. In the later, the removed nucleon is absorbed by the target, leaving the target nucleus in an excited state.

The relative importance of each process depends on the beam energy. At high beam energies, the single-nucleon knockout yield is dominated by stripping reactions, whereas at lower energies, ~ 50 MeVA, both contributions are similar.

It is worth mentioning that there is a third reaction mechanism, called Coulomb dissociation, by which a nucleon can be removed from the projectile due to Coulomb interactions with the target. However, since the targets are traditionally chosen with low atomic number Z, the one-nucleon removal yield due to Coulomb dissociation is very small in comparison with diffraction and stripping, and therefore its effect is negligible in the cross sections.

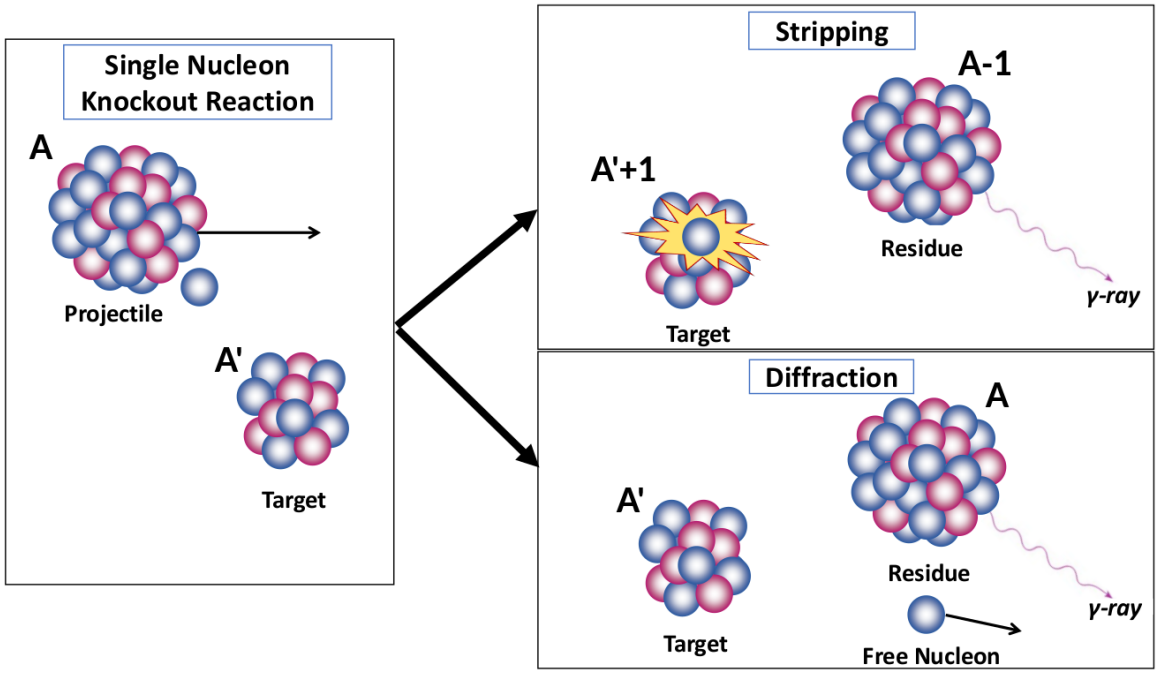

Figure 2.10: Schematic representation of the different types of single nucleon knockout reactions: inelastic breakup or stripping (top right) and elastic breakup or diffraction (bottom right).

2.5.1.1 Reaction formalism

One-nucleon knockout reactions in inverse kinematics are often described using the few-body Glauber method [43], which is based on the eikonal approximation and the adiabatic or sudden approximation:

- **eikonal approximation:** assumes that both incoming and outgoing particles are traveling through the medium following a straight path. The wavelength of the projectile, λ, should be much shorter than the target potential range, α, i.e. $\alpha/\lambda \ggg 1$.
- **adiabatic or sudden approximation:** assumes that the internal motion of the system during the reaction is small compared to the motion of its centre of mass. The energy of the scattered particle, E', ought to be a lot higher than the potential depth, V_0, i.e. $E' \ggg V_0$.

These approximations are fully justified for our experimental case, due to the high beam energy ($\beta \approx 0.7$) and the fact that all particles are scattered in forward direction. Under these conditions, the eikonal wavefunction can be written as:

$$\psi_k^{+/-}(\vec{r}) = e^{i\vec{k}\vec{r}} S^{+/-}(b) \tag{2.25}$$

for incoming (+) and outgoing (-) particles, where $\vec{r}$ is the vector between core and valence nucleon in the projectile and b is the transverse component of $\vec{r}$, can be understood

as the impact parameter. The scattering matrix $S^{+/-}(b)$ describes the scattering of the incoming/outgoing particles, and is defined as:

$$S^{+/-}(b) = e^{i\chi^{+/-}(b)} \tag{2.26}$$

where $\chi^{+/-}(b)$ is the eikonal phase, expressed as:

$$\chi^{+/-}(b) = \frac{1}{k}\int_{-\infty}^{0} U_{opt}^{+/-}(\vec{r})dz \tag{2.27}$$

where v is the relative velocity between projectile and target and $U_{opt}^{+/-}(\vec{r})$ are the optical potentials describing the elastic scattering of nucleon and core with the target. The simplest description of this optical potential is the $t\rho$ or $t\rho\rho$ approach, that in the optical limit of the Glauber theory can be written as follows:

$$\chi^{+/-}(b) = \frac{1}{k}\int_{0}^{-\infty} q\tilde{\rho}_p(q)\tilde{\rho}_t(q)f_{NN}(q)J_0(qb)dq \tag{2.28}$$

where $\tilde{\rho}_p(q)$ and $\tilde{\rho}_t(q)$ are the Fourier transformations of the nuclear densities of projectile p and target t respectively, J_0 is the Bessel function and f_{NN} is the nucleon-nucleon scattering amplitude:

$$f_{NN}(q) = \frac{k}{4\pi}\sigma_{NN}(i + \alpha_{NN})e^{-\beta_{NN}q^2} \tag{2.29}$$

being σ_{NN}, α_{NN} and β_{NN} parameters fitted to reproduce nucleon-nucleon scattering data at forward angles.

This theoretical framework allows the calculation of the cross sections corresponding to the removal of a nucleon from a given single-particle quantum state. These single-particle cross sections have contributions from stripping ($\sigma_{stripping}$) and diffraction ($\sigma_{diffraction}$) reactions, while Coulomb dissociation effect is considered negligible. Therefore:

$$\sigma_{knockout} = \sigma_{stripping} + \sigma_{diffraction} \tag{2.30}$$

Once the scattering matrices S_c and S_n of core and nucleon are known, it is then possible to calculate the stripping cross sections as:

$$\sigma_{stripping} = \frac{1}{2J+1}\int \sum_m \langle\psi_{Jm}||S_c|^2\left(1 - |S_n|^2\right)|\psi_{Jm}\rangle db \tag{2.31}$$

where an integral over all impact parameters is made for the probability that the core survives the reaction ($|S_c|^2$) and the valence nucleon is absorbed ($1 - |S_n|^2$). Following a similar reasoning, the cross section for diffractive breakup may be found by

$$\sigma_{diffraction} = \frac{1}{2J+1} \int \sum_{m} \left| \langle \psi_{Jm} | |1 - S_n S_c|^2 | \psi_{Jm} \rangle \right|^2 - \sum_{m,m'} \left| \langle \psi_{Jm'} | 1 - |S_n S_c| | \psi_{Jm} \rangle \right|^2 db \quad (2.32)$$

2.5.2 Quasi-Free Scattering Reactions

In general, quasi-free scattering (QFS) or a quasi-elastic reactions are direct reactions where a bound nucleon, either a proton or a nucleon, is removed by a high-energy particle (100 to 1000 MeV) from a nucleus ${}^{Z}A$. They are therefore a type of knockout reactions with some specific characteristics.

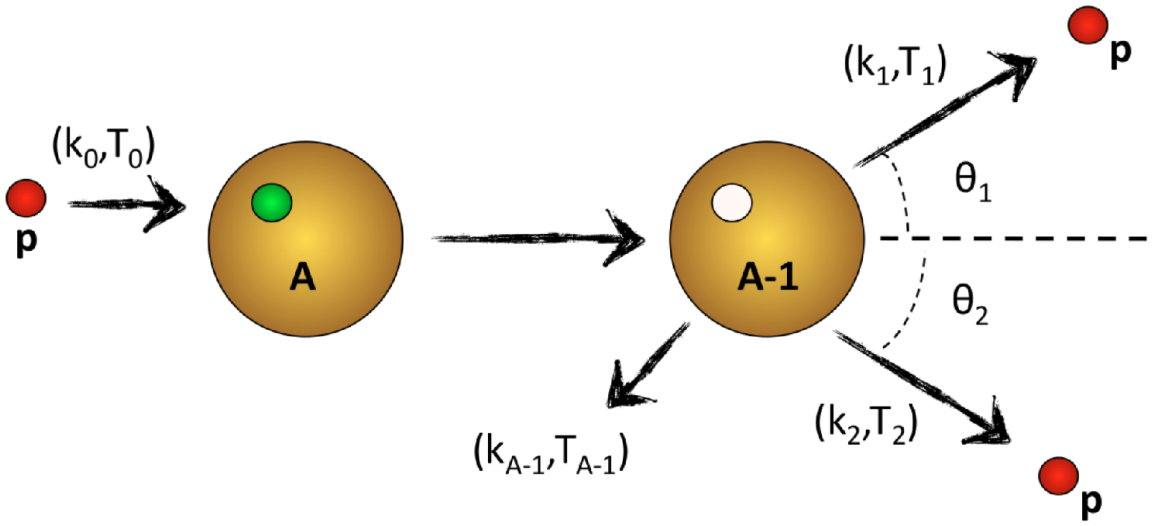

Figure 2.11: $(p, 2p)$ quasi-free scattering kinematics. (k_0, T_0) represents the momentum vector and kinetic energy of the incoming projectile respectively., (k_{A-1}, T_{A-1}) is the momentum vector and kinetic energy of the the residual fragment and (k_1, T_1) and (k_2, T_2) for the ejected protons. Original taken from [44].

The first studies of this type of reaction were back in the early 50's at the Lawrence Berkeley Laboratory by O. Chamberlain and E. Segré, where they impinged 340 MeV protons on a lithium target and observed paired protons scattering at ∼90°. This is in fact one of the classical signatures of the QFS reactions.

Depending on the character of the nucleon removed, examples of QFS reactions in inverse kinematics can be $(p, 2p)$ and (p, pn), where a proton from the target removes a nucleon from the beam particle. Both particles are emitted in the same plane (φ ∼180°) and with an opening angle of 90° (θ ∼90°), as both have the same mass.

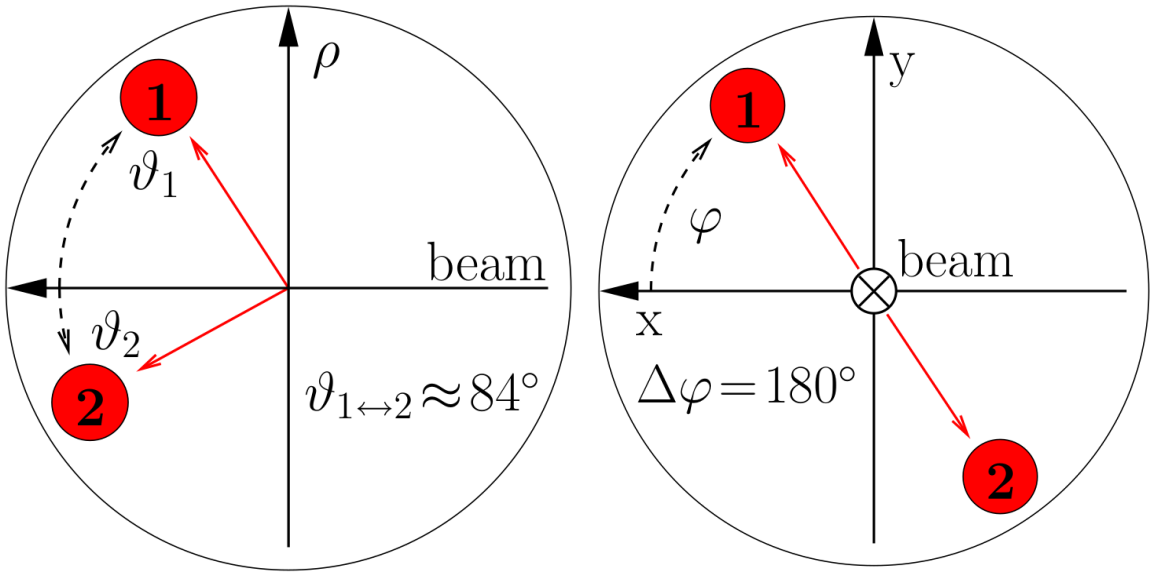

(a) Polar angular correlations (b) Azimuthal angular correlations

Figure 2.12: Theoretical angular correlations for QFS protons. The sum of the azimuthal angles should be 180° while in the polar plane the protons scatter at ≈84°. Figures taken from [45].

2.6 Current knowledge on neutron-rich carbon isotopes

The motivation of this experiment intendsto locate and identify the mixed-symmetry second 2^+ excited state in even-mass neutron-rich carbon isotopes, namely ^{16}C, ^{18}C and ^{20}C. This will be done by probing the structure of such nuclei populating bound and unbound states via quasi-free scattering (p,2p) reactions induced by ^{17}N, ^{19}N and ^{21}N beams. This mixed-symmetry second 2^+ is expected to be unbound and therefore, likely to decay through neutron emission towards ^{15}C, ^{17}C and ^{19}C respectively.

This scenario makes the level scheme of even-mass neutron-rich carbon isotopes ^{16}C, ^{18}C and ^{20}C due to direct population from (p,2p) relevant to our analysis. The level scheme of odd-mass neutron-rich carbon isotopes ^{15}C, ^{17}C and ^{19}C due to possible population from the one neutron decay channels from ^{16}C, ^{18}C and ^{20}C respectively is also important. In the following, the latest work on these nuclei and the corresponding level scheme will be presented.

2.6.1 Even-mass neutron-rich carbon isotopes

2.6.1.1 ^{16}C

Spectroscopy of ^{16}C has been extensively investigated via fusion-evaporation reactions [14], one-proton knockout [17], inelastic scattering [25, 46], one-neutron transfer [16] and two-neutron transfer reactions [47, 48]. These works allowed to identify four γ-ray transitions amongst the bound states of ^{16}C, as seen in the level scheme presented in Figure 2.13.

In the latter work by Balamuth *et al.* [48], bound states in ^{16}C have been accessed via ^{14}C$(t,p)^{16}$C transfer reaction in order to probe $(sd)^2$ configurations. The good agreement between experimental excitation energies and (t,p) transfer strengths and theoretical predictions for positive parity states of ^{14}C and ^{16}C are deemed as $(sd)^2$ two-neutron states coupled to ^{12}C and ^{14}C cores respectively [49]. This is a consequence of the virtual identicality in the $2s_{1/2}$-$1d_{5/2}$ splitting in ^{13}C and ^{15}C.

Regarding the unbound states, the first experimental evidence on the population of the unbound states in ^{16}C was the observation in 1977 of the 2_1^+ state at 6.11 MeV by Fortune *et al.* via (t,p) reaction [47]. More recently, Satou *et al.* used one neutron knockout reactions to populated unbound states below 7 MeV [50], and the reconstruction of the fragment momentum distribution allowed the spin and parity identification. Finally, H. G. Bohlen *et al.* used three neutron transfer reaction ^{13}C(^{12}C,^{9}C)^{16}C, where the states above 7 MeV were observed for the first time [51].

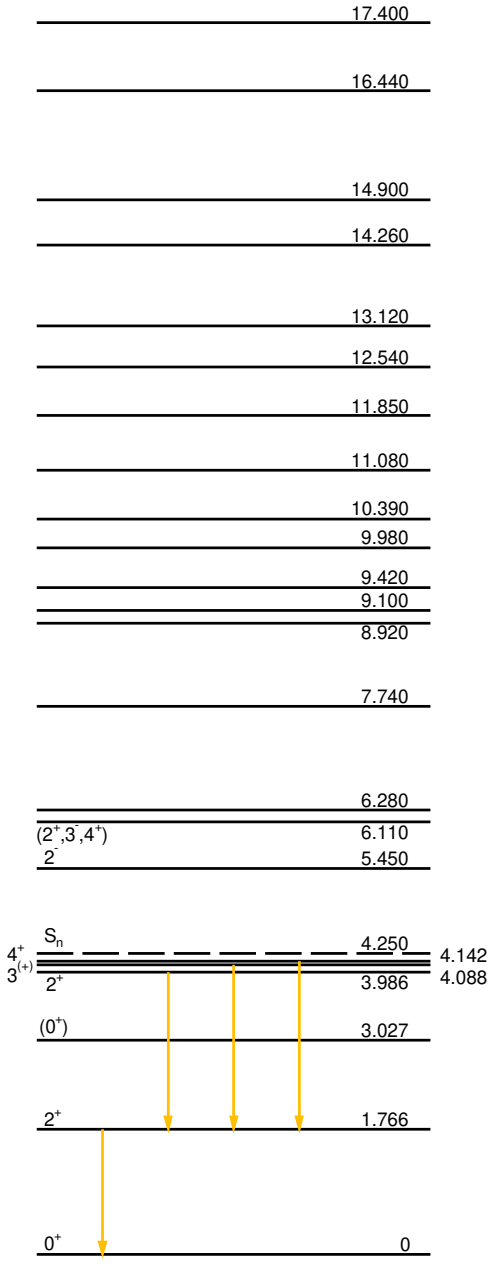

Figure 2.13: Complete level scheme of ^{16}C

2.6.1.2 ^{18}C

The low-lying structure of ^{18}C has been studied in recent experiments through pion charge exchange [52], fragmentation [12, 53], inelastic scattering [20], one neutron removal [54] and one proton knockout [21, 55]. However, current knowledge is limited to 4 γ-ray transitions, 3 of them first observed by Stanoiu *et al.* [12], while the 2.5 MeV transition was observed by P. Voss *et al.* [21]. Unfortunately, there is no information on the unbound states of ^{18}C.

Of particular interest is the previous study of ^{18}C via one proton knockout reactions [55] done at GSI using the same R^{3}B/LAND set up used in this work. Bound and unbound states in ^{18}C were analysed with the purpose of studying two-neutron correlations. It allowed to confirm the structure of ^{18}C as a core of ^{14}C plus four valence neutrons arranged in strongly correlated pairs in the *sd* shells.

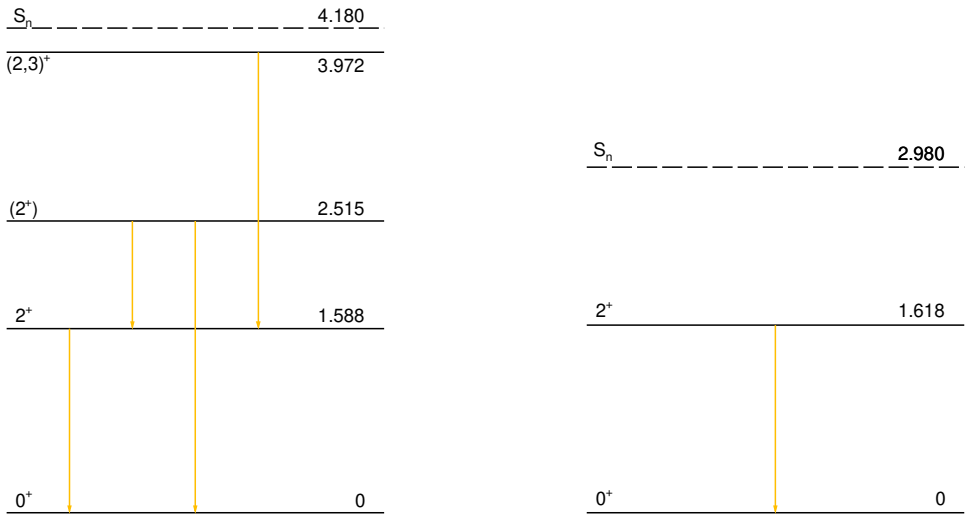

(a) ^{18}C (b) ^{20}C

Figure 2.14: Complete level schemes of ^{18}C (left) and ^{20}C (right).

2.6.1.3 ^{20}C

At the time of writing very little is known about ^{20}C. A few experiments have been performed recently, including fragmentation [12], two proton knockout reaction [15] and inelastic scattering [56] studies but only the first excited state has been observed so far, identified as a 2^+ and located at at 1.618 MeV [15].

This observation, however, was enough to extend the study of the systematics of the energies of the first 2^+ states in neutron-rich carbon isotopes up to N=12. This suggests that the N=14 subshell gap observed in oxygen isotopic chain is no longer present in neutron-rich carbon isotopes due to the reduced proton-neutron tensor and neutron-neutron interaction [12].

2.6.2 Odd-mass neutron-rich carbon isotopes

2.6.2.1 ^{15}C

A large body of experimental efforts was devoted to study the level scheme of ^{15}C, including fusion-evaporation [57, 58], two neutron transfer (t,p) [59–61] and (α,2p) [62, 63], one neutron transfer (d,p) [64–66] and (^{13}C,^{12}C) [67, 68] and charge exchange two proton removal. These works show very good agreement locating the only bound excited state at 740.0(15) keV with spin and parity assignment of $5/2^+$, thanks to angular distribution measurements by Cecil *et al.* [64].

The opposite happens for the unbound states, where a significant number of resonant states has been observed beyond the neutron separation threshold, most of them where observed for the first time almost 50 years ago, by Garrett *et al.* [57] in 1974 via the ^{9}Be(^{7}Li,p)^{15}C reaction. Despite angular distributions measurements in one and two neutron transfer reactions were helpful to identify the J^π and the spectroscopic nature of some of these states, there is no firm spin and parity assignment for the unbound states beyond 6 MeV yet (see Figure 2.15).

2.6.2.2 ^{17}C

The spectroscopy of ^{17}C has been the focus of a number of experimental studies using very different approaches: three neutron transfer reaction [51], fragmentation [12], proton inelastic scattering [46, 69], one neutron removal [54, 70, 71], β-delayed γ-ray spectroscopy measurement [72] and one neutron transfer reactions [8]. The excitation energies provided by these references show an excellent agreement locating the first and second excited states in ^{17}C at 0.217(1) and 0.332(2) MeV. Transverse-momentum distributions from knockout fragments measured by Kondo *et al.* [54] and angular distributions of protons arising from (d,p) transfer reactions observed by Pereira-Lopez *et al.* [8] confirmed $3/2^+$, $1/2^+$ and $5/2^+$ assignments for the ground state and the first and second excited states respectively.

Concerning the unbound states, different works were able to observe several states beyond the low neutron separation energy of ^{17}C at 734 keV. A three neutron transfer reaction study [51] located 10 states above the neutron separation energy, with only definitive identification of the $9/2^+$ state at 3.10 MeV. A proton inelastic scattering experiment [50] has observed states at 2.20, 3.05 and 6.13 MeV. A β-delayed neutron study [72] reported levels at 2.71, 3.93, 4.05, 4.78 and 5.08 MeV, the first three assigned to $1/2^-$, $3/2^-$ and $(5/2^-)$. Three unbound states were found by one neutron knockout of ^{18}C [73] at 2.74, 3.03 and 4.03 MeV, but only the first one has been assigned to be $J^\pi = 1/2^-$ (see Figure 2.15).

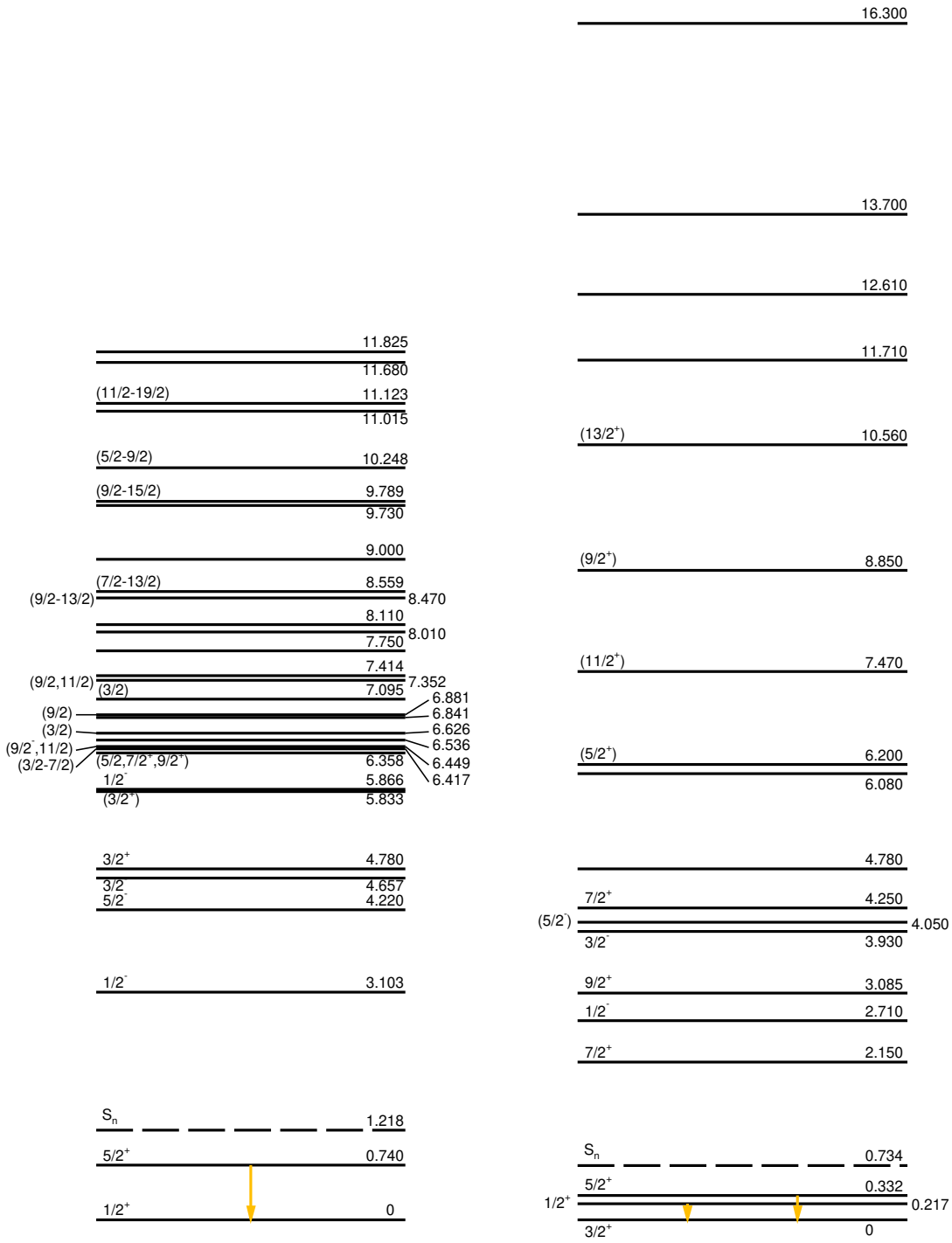

(a) ^{15}C (b) ^{17}C

Figure 2.15: Complete level scheme of ^{15}C and ^{17}C

2.6.2.3 ^{19}C

The low-lying states in ^{19}C have been investigated via fragmentation [53], proton inelastic scattering [56, 69], one neutron knockout [74] and one proton knockout [75]. However, only a two γ-ray cascade was observed, corresponding to states at 209 and 283 keV [56] with no definite spin and parity assignment yet.

In addition, two unbound states are known: one resonance at 1.46 MeV was observed by proton inelastic scattering and identified as $5/2^+$ by angular distributions [69], while 1p2n removal reactions showed evidence of an unbound state at 653 keV [76], very close to the neutron separation energy of 580 keV.

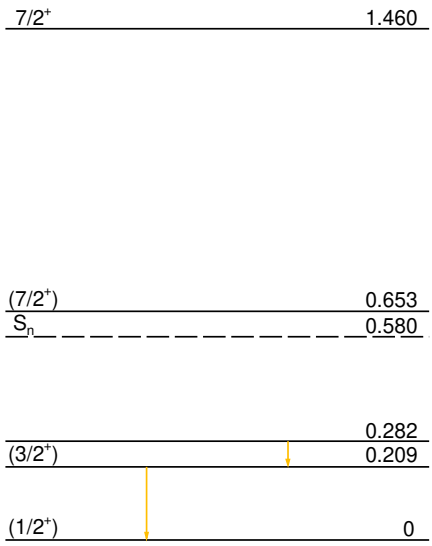

Figure 2.16: Complete level schemes of ^{19}C

Chapter 3

Experimental Details

3.1 Experimental Overview

The experiment S393 took place in August 2010 using the R^3B/LAND setup at GSI, Helmholtzzentrum für Schwerionenforschung in Darmstadt, Germany, where states in ^{16}C, ^{18}C and ^{20}C are populated via quasi-free scattering $(p, 2p)$ reactions from ^{17}N, ^{19}N, and ^{21}N beams bombarding a CH_2 target.

The R^3B/LAND set up allows to study reactions in inverse kinematics via Coulomb excitation and quasi-free scattering reactions at relativistic energies, by performing triple and even quadruple coincidences on an event-by-event basis by requiring a registration of incoming particles, an outgoing fragment, the produced neutrons and/or γ rays (see Figure 3.1).

The secondary beam particles are identified before reaching the target area via time-of-flight and energy loss measurements using the last focal plane of the fragment separator S8, the Position detector POS and the Position-Sensitive Pin Diode (PSP) detectors, while the Right-Up-Left-Down detector (ROLU) is used as a veto detector to control the spot size of the beam. The trajectory of both the incoming beam and fragments is measured with 2 pairs of double sided silicon strip detectors (DSSSDs or SSD), one before and one after the target. Four of them are built together into a box-like geometry around the target dedicated for angular measurements.

The trajectories of the outgoing heavy products are bent by the dipole magnet ALADIN according to their A/Z ratio towards the fragment arm, comprised of two fiber detectors (GFI) that provide only x position, and the Time of Flight Wall (TFW), which provide measurements of both x and y positions as well as time for velocity measurements. Since neutrons are insensitive to the magnetic field, neutrons evaporated from the decaying systems

are detected with the Large Area Neutron Detector (LAND) located at 12.5m on the zero-degree arm.

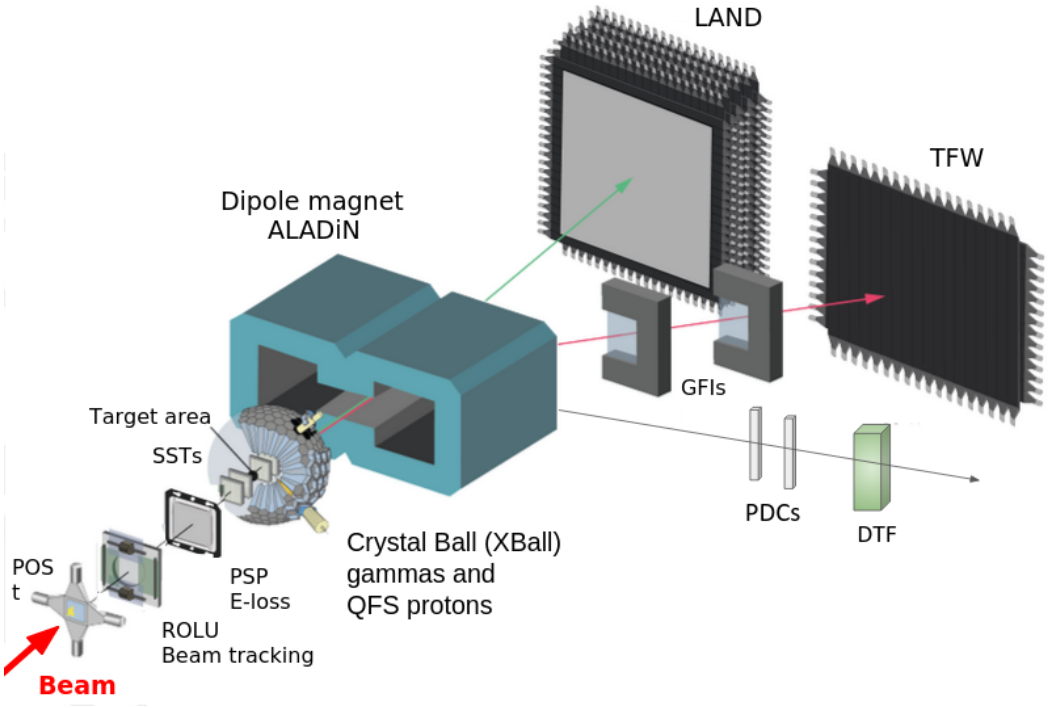

Figure 3.1: R^3B/LAND setup. Energy loss, beam tracking and time detectors can be seen at the left-hand side followed by Crystal Ball γ-ray detector array, surrounding the target. After ALADIN, neutron, fragment and proton arms are shown on the right-hand side. Picture taken from [77].

In order to accurately determine the cross sections of the $(p, 2p)$ reactions, data was collected with a second target of pure carbon so the yield due to reactions with C nuclei in the CH_2 target could be subtracted. Besides, in order to estimate additional spurious reactions from the in-beam detectors, a run with no target (MT) was recorded.

3.2 Beam production

In this experiment the in-flight technique for the beam production was used at the GSI accelerator facility in Darmstadt (see Fig. 3.2). A primary beam of ^{40}Ar was used, initially accelerated to an energy of $\approx$ 11.5 AMeV and partially stripped of its electrons at the Universal Linear Accelerator (UNILAC). Then the $^{40}Ar^{+11}$ ions were injected into the synchrotron for heavy ions called SIS18 (named after the combination of its name in German: *SchwerIonenSynchroton* and its maximum magnetic rigidity, 18 Tm). Here, the ions underwent a further acceleration up to 490 AMeV. The primary beam was then extracted in the form of two-second spills and transported into FRagment Separator (FRS), where it impinged on a 4011 mg/cm^2 Be production target with an intensity of 6×10^{10} particles per second.

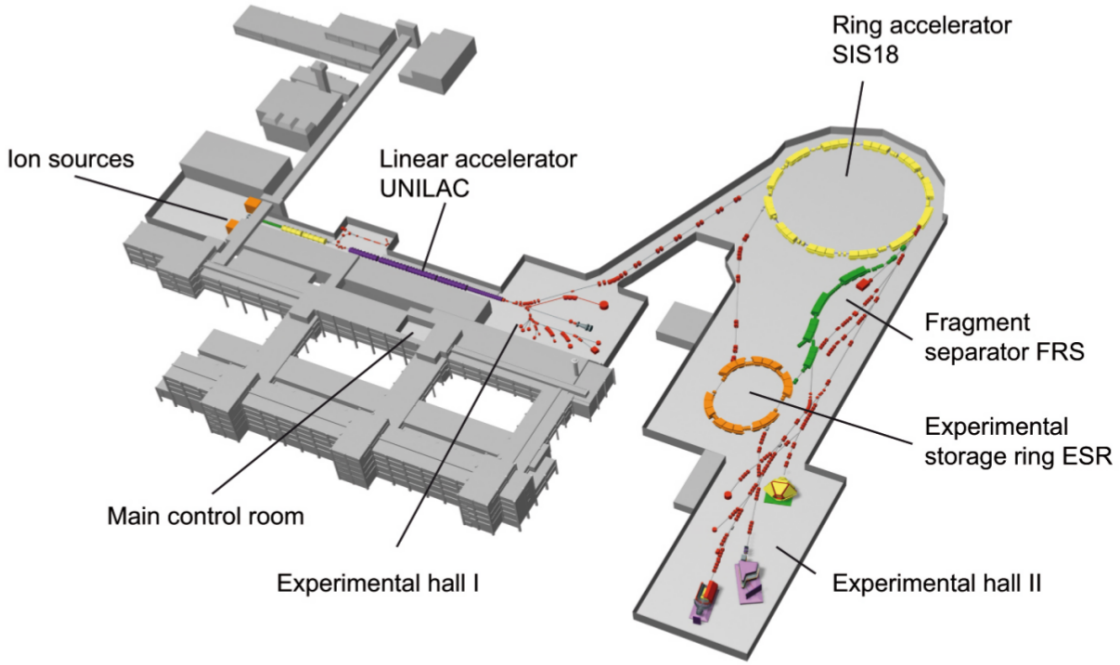

Figure 3.2: Layout of the GSI radioactive beam facility. A stable primary beam is accelerated by UNILAC and SIS18 before impinging the production target at FRS, where the secondary beam of radioactive ions are selected and transported to the Cave C in the experimental hall II in which the R^3B/LAND setup setup is located.

The FRS is a high-resolution forward spectrometer intended for the production, analysis and selection of radioactive ion beams (see Fig. 3.3). The production target is placed at its entrance, where a wide range of different radioactive nuclei are produced by fragmentation reactions. Among these nuclei, the isotope of interest are selected and transported by a series of dipole and quadrupole magnets and delivered to the experimental area. Here the dipole magnets separate the beam species of interest depending on the mass-to-charge ratio A/Z satisfying the relation:

$$B\rho \propto \frac{A}{Z}\beta\gamma \tag{3.1}$$

where B is the magnetic field, ρ the curvature of the trajectory through the field, β the velocity of fragments and γ the Lorentz factor. The use of six different magnetic rigidity settings allowed to select different radioactive ion beams and study the reactions induced with different nuclei.

The different quadrupole and sextupole magnets are intended to focus the transported ions and control the beam profile in x and y direction.

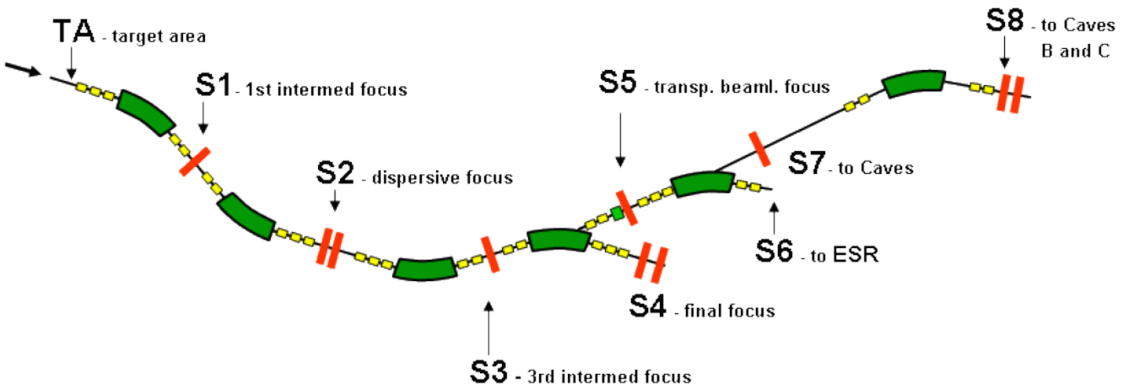

Figure 3.3: Schematic representation of the FRagment Separator (FRS) used at GSI to select the radioactive nuclei of interest produced by fragmentation at the production target placed at the entrance (target area, TA) and transport them to the experimental area (Cave C in our case, in S8). Dipole magnets (green) are used to separate the fragments and quadrupole magnets (yellow) are intended to control the profile the beam in x an y. At S2 a wedge-shaped degrader can be placed to enhance beam selection.

3.3 Beam-tracking detectors

3.3.1 POS

It is the first detector of the R3B/LAND setup. It allows to calculate the beam velocity of the incoming/outgoing particles by providing the stop/start signal to measure the time-of-flight from S8 to POS and from POS to TFW. It is composed of a square-shaped plastic scintillator sheet coupled by a light guide to four PMTs that provide time and amplitude information (see Fig. 3.4). Its active area is (5.5 × 5.5) cm^2 and 2 mm thick for the S393 experiment.

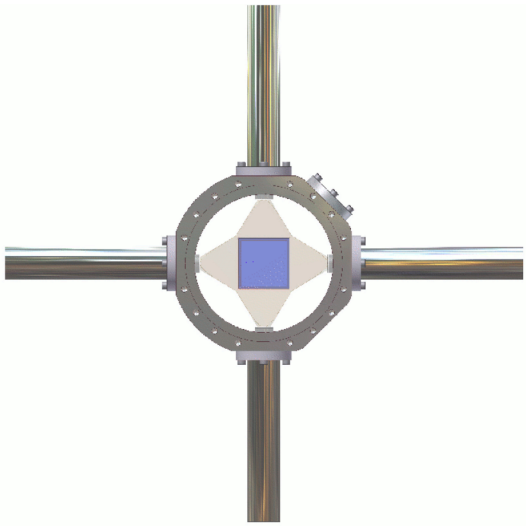

Figure 3.4: Scheme of the POS detector. Taken from [78]

3.3.2 ROLU

Called after its name in German *"Rechts-Oben-Links-Unten"* (right-up-left-down) is a detector array comprised of four movable plastic scintillators each coupled to a PMT (see Fig. 3.5. Each scintillator is 5 mm thick and has an active area of (5 × 5) cm^2. ROLU is designated to define the beam-spot size acting as a veto signal for all particles hitting the scintillators. POS in anticoincidence with ROLU plays an important role as the spill-on trigger.

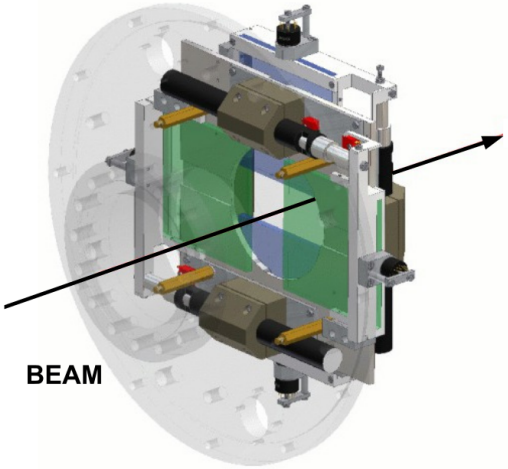

Figure 3.5: Layout of ROLU (left). Taken from [78].

3.3.3 Position Sensitive Pin (PSP)

The Position Sensitive Pin silicon diode is a 300 μm square-shaped plate with an active area of (4.5 x 4.5) cm^2. It has four anodes located close to the corners on the horizontal sides of the plate (see Figure 3.6) that record position tracking signals and a single cathode located in the middle of the upper side of the plate that records energy loss of the ion. The energy resolution is 1% and position resolution of 0.02 cm. For this experiment only the energy-loss measurements in combination with time-of-flight measurements from S8 and POS were used for the incoming particle identification.

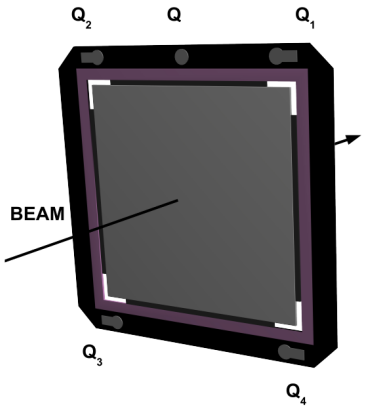

Figure 3.6: PSP detector. Taken from [79].

3.4 SSDs

The purpose of this array of detectors is to track the X and Y position of charged particles and heavy fragments. They also provide information on energy loss.

These double-sided silicon strip detectors have each an active area of 72x40 mm^2 and a thickness of 300 μm (see Fig. 3.7). One side of a detector corresponds to the horizontal plane and the other one to the vertical plane (s and k). The junction side (p-side) is called s-side while the ohmic side (n-side) is called k-side. The former has a larger dimension, a read-out pitch of 110 μm and an implantation pitch of 27.5 μm. It has 2560 strips and every fourth one is connected to a read-out channel, (640 channels in total). The k-side is 40 mm long and its implantation pitch is 104 μm. Each of the strips on this side are read out individually (384 channels). The total number of strips in each SSD is 1024.

In this analysis these detectors are used primarily in coincidence with TFW to identify the charge of the outgoing particles.

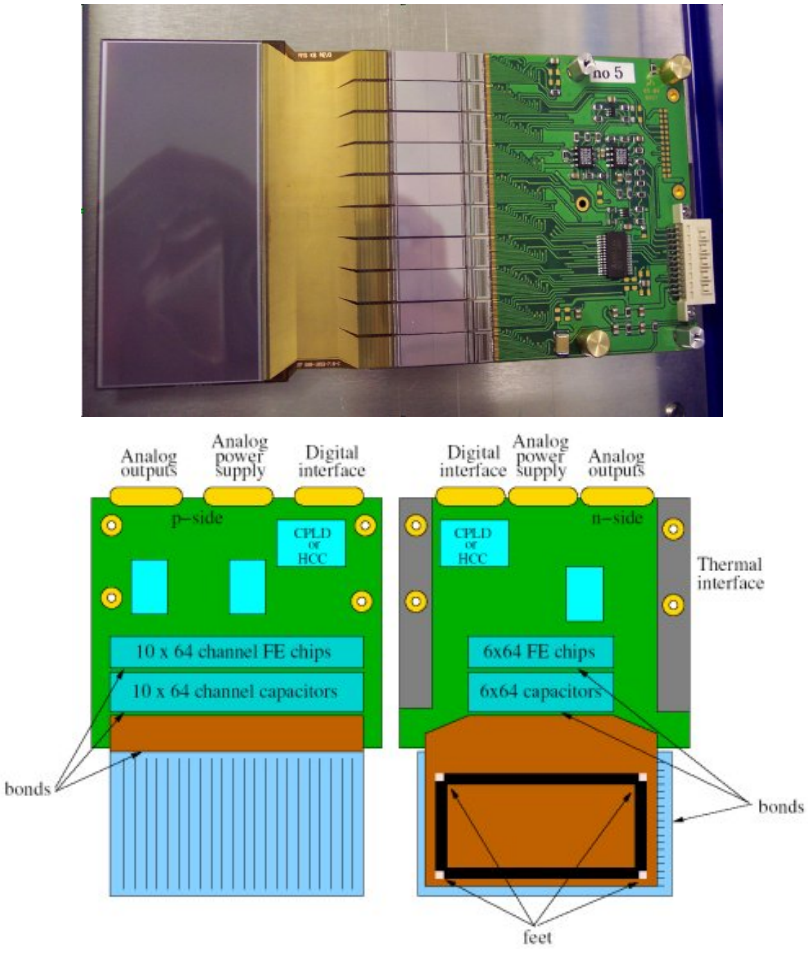

Figure 3.7: Top: photo of a SSD detector. Bottom: Layout of the p-side (left) and the n-side (right) of a SSD.

3.5 Crystal Ball

The target area is enclosed by Crystal Ball (XB), a detector array that allows high-efficiency measurements of the high-energy γ-rays from the deexcitation of fragments and high energy protons.

Crystal Ball is formed by 162 NaI(Tl) crystals coupled to PMTs and arranged in a $\sim 4\pi$ configuration of a 90 cm diameter sphere around the target (see Fig. 3.8). The crystals have four different shapes. 12 are regular pentagons and 150 crystals classified into three different irregular-hexagon shapes (see F. Wamers thesis for more details [45]). Each crystal has an opening angle of 14°. The identification of the protons is possible due to an upgrade of a secondary readout channel added in 64 forward-focused crystals. For this reason, the crystal signals are readout twice. The first reading is done at the first anode for the γs, and the second reading at the final dynode of the PMT for the protons.

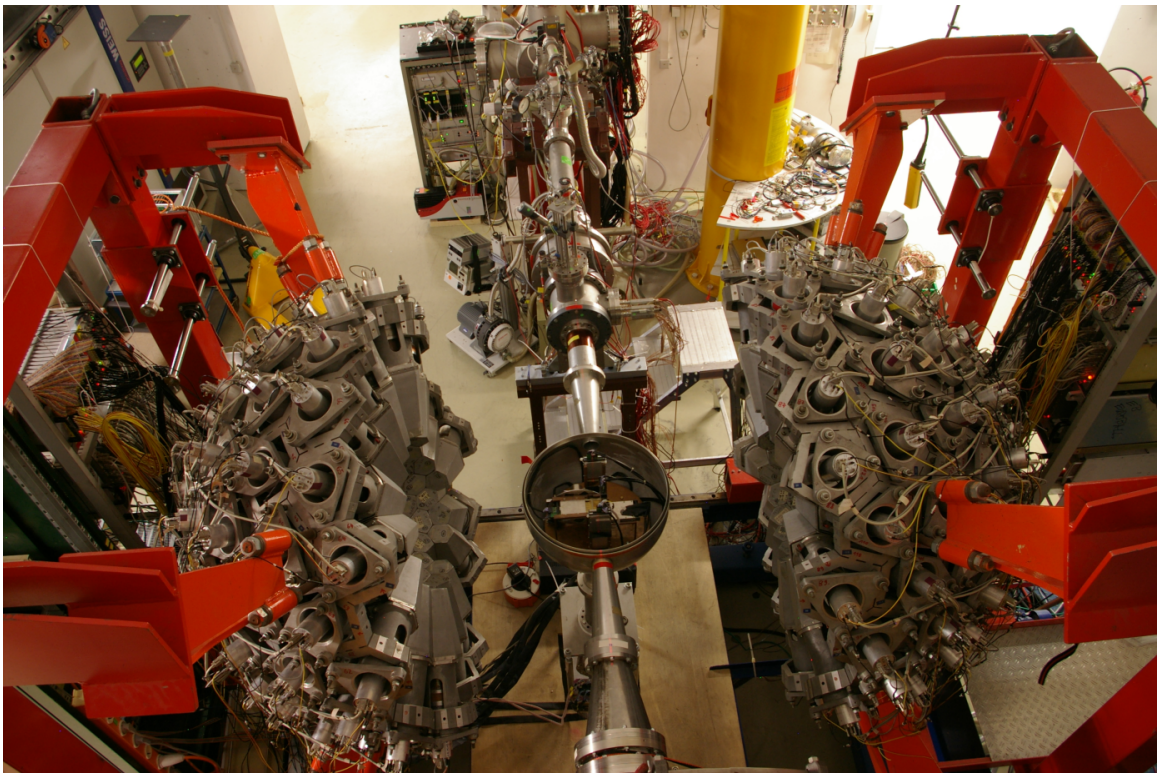

Figure 3.8: Photograph of Crystal Ball opened. The beamline and opened target chamber can be seen. Taken from [79]

Both the γ and proton branches have the capability of recording energy signals by using charge-to-digital (QCD) converters. For the case of the γ branch, it also allows recording time signals due to the coupling of a Constant Fraction Discriminator (CFD) and a Time-to-Digital converter (TDC). The time signals of several crystals work as a general trigger for XBall.

3.6 ALADIN

After the target area, DSSSDs and Crystal Ball, comes ALADIN (A Large Acceptance DIpole MagNet) (see Fig. 3.9), which as its name suggests, is the dipole magnet that separates the reaction products and bends the charged particles, namely the heavy fragments and the protons, according to their magnetic rigidities. ALADIN is filled with helium.

It has a maximum magnetic field of 1.6 T and a maximum $B\rho_{max} = 18$ T·m by 8°. The angular acceptance is ±60 mrad. Although the maximum current is 2500 A, above 1900 A there is a non-negligible saturation effect, where the magnetic field and current are no longer linearly correlated.

Figure 3.9: Photograph of ALADIN.

3.7 Downstream detectors

3.7.1 GFIs

The fibre detectors (GFIs) (Grosse FIberdetektor) are designated to measure the trajectories of heavy fragments behind ALADIN. Both GFIs are designated to track the x-direction of the particles although one can be rotated 90° in order to track the y-direction. For the s393 campaign, both GFIs were used to track the x-position.

Each GFI has an active area of (50 × 50) cm^2 and is comprised of 480 scintillating fibres. Each fibre is 50 cm long and has a square cross section of (1.0 × 1.0) mm^2. The detector provides a position resolution of ∼1 mm and a geometrical efficiency of 89% for charges Z≥3 and a very low resolution for Z≤3. Each fibre is read out at both ends. However, for this experiment, only one end was used. This end is connected to a Position-Sensitive PMT (PSPM), which has a 16 mesh dynodes and a grid of anodes with 16 wires in one direction and 18 wires each correlated to a fibre that allows the position measurements on the PSPM and to the beam.

3.7.2 Time of Flight Wall

The purpose of Time of Flight Wall (TFW) is intended to identify the outgoing charge particles by energy loss and time-of-flight measurements.

It is comprised of 32 scintillating paddles arranged in two layers orthogonal to the beam direction (see Fig. 3.10). Each paddle is coupled to two PMTs on ADC. One layer is formed by 18 vertical paddles of 147 cm and the other one by 14 horizontal paddles (189 cm) each of a 10.4 cm width and a thickness of 0.5 cm with an active area of 147 x 189 cm.

ToF measurements allow to extract β velocity of heavy fragments from the first detector in the direction of the beam (POS) and the TFW. Since a particle traverse both panels, for a single hit, TFW provides 4 signals, two corresponding to the vertical hit paddle and two for the horizontal one. Hence, ToF measurements are obtained by calculating the mean of these four time signals. Rough position measurements of the hits are possible by calculating the time difference between both ends of the hit paddle or alternatively, by calculating the ratio of the energy loss measurements of both ends. Allows A/Z measurements. The signals are digitised with an ADC for energy loss and a TDC for the time measurement.

Figure 3.10: Time of Flight Wall

3.7.3 LAND

Large Area Neutron Detector (LAND) is a time-of-flight (TOF) detector designated for neutrons with an efficiency above 94% for neutrons of 400 MeV or higher [80], allowing 3D tracking, velocity and energy loss measurements.. LAND measures energy loss and position of neutrons.

LAND is comprised of 10 planes with 20 alternating iron and organic scintillating 5-cm paddles each. Each paddle has a layered structure comprised of alternating iron and scintillating sheets in order to optimise the detection efficiency. Each sheet is 5 mm thick except for the outer layers, which are both 2.5-mm-thick iron sheets. The planes are arranged in such a way that the paddle orientation in the next plane is perpedicular to the previous one. This is what enables LAND to give X and Y positions of the orthogonally incident neutrons as seen in Figure 3.11. Since the neutrons are insensitive to the magnetic field, these go straight to the 0° line, where LAND is located at 12.5 m from the target.

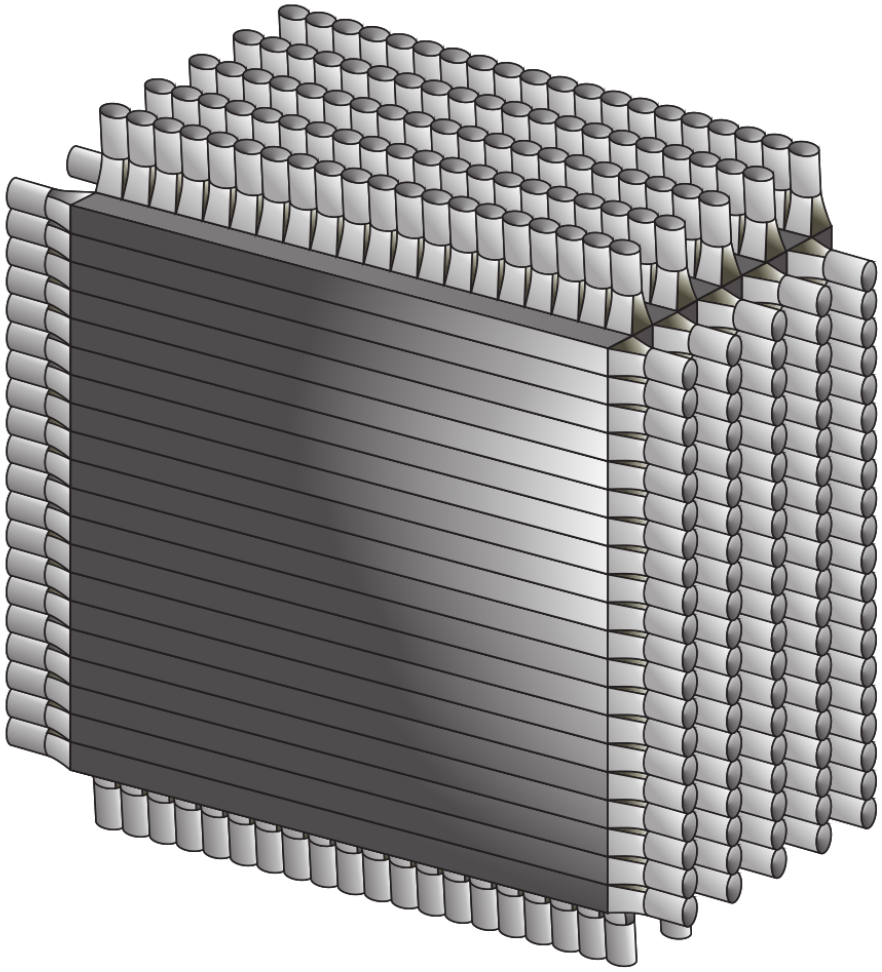

Figure 3.11: Illustrative LAND detector scheme. Although here are only 5 panels shown it consists of ten panels of scintillating paddles. Taken from [81].

3.8 Data Acquisition

In order to have readable information obtained from the interaction of particles with the detection devices , it is firstly converted into electrical signals and then digitised and finally, written and stored into data files by the Data Acquisition System (DAQ). Given the large volume of data obtained in an experiment, a system of logic criteria is implemented in order to determine what signals will be considered as an event of interest and what is useless information or noise to be discarded. Therefore, selecting a set of events combining valid signals from different detectors to identify the reaction channels of interest, and hence, optimise the storage space.

The Data Acquisition System of the R^3B/LAND setup is called the Multi Branch System (MBS). Data is recorded on an event-by-event basis and stored in files with a data format developed at GSI, called List Mode Data (lmd), which are later converted to ROOT files

in a process called *unpacking* by using the land02 software developed by H. Johansson [82]. Due to the high-rates (10^5 ions/spill), the Data Acquisition System was configured in such a way that the arriving events were sorted into different trigger patterns (Tpat), associating a different Tpat value to each event depending on the combination of different valid signals (understanding as valid signals those within the given time window and above the thresholds of the corresponding detector) that are comprised in that particular event.

The valid signals are identified by the associated trigger (called Trigger Bit or Tbits), which is a boolean value that indicates whether that detection system (or a combination of them) was hit and is producing a valid signal in a particular event.

In general, depending on the physics to be analysed, only some TBits are taken into account. For this reason, Table 3.1 presents those trigger patterns that are relevant to the present analysis. For the identification of incoming and outgoing ions the Fragment Tbit is used. It is defined by a coincidence of the trigger from POS in anti-coincidence with ROLU plus a trigger from the TFW. In addition, XBSum trigger is the reaction trigger for the QFS reactions and indicates deposited energy in XBall above a predefined threshold. The time signals from crystals (up to 16) are combined and converted into a leading edge discriminator and then combined with a logical OR. Finally, Neutron Tbit selects a possible neutron hit in LAND. It requires a coincidence of POS!ROLU, a trigger from the TFW and from LAND.

	Tbit n	Tpat $2^{(n-1)}$	Aim	Early pile-up	late-trigger kill	POS!ROLU	TFW	XB SUM	LAND Mult
Min. bias	1	1	Good beam (GB)			x			
Fragment	2	2	GB and hit in TFW	x		x	x		
XBall Sum	4	8	XBall hit	x	x	x	x	x	
LAND	8	128	neutron hit on LAND	x		x	x		x

Table 3.1: Main triggers of S393 for this analysis and triggers required for each one of them.

In this experiment, triggers (or Tbits) can be sorted in two different categories. The first one, called *on-spill*, accounts for those trigger signals in coincidence with a valid signal of the beam delivery given by the FRS monitor system. Some are in coincidence with a trigger signal.

The second one, *off-spill* triggers are those signals in anti-coincidence with a trigger signal from the FRS, useful mainly for the calibration of detectors. These Tbits are recorded in those no-signal time intervals between a spill of beam and th next spill of the beam.

In order to reduce the dead time of the DAQ and optimise storage space, for certain Tpat values that come with very high yields only a fraction of the events is recorded. For such a

purpose, a downscaling (DS) factor n is defined, in such a way that only the n^{th} event with the same Tpat is recorded. Reaction trigger bits are always n=1 so they are not downscaled, i.e. they are all recorded.

Chapter 4

Data analysis

In the previous chapter the experimental setup and all the detection subsystems comprised were presented. This chapter will describe the analysis techniques used to extract results from this experiment seeking answers that motivated this work.

The goal of this work is to study ^{17,19,21}N(p,2p)^{16,18,20}C* reactions. Therefore the first step in the analysis would be the identification of the incoming nuclei of interest, followed by the identification of the outgoing fragment in order to select the channel of interest. In addition, analysis of the protons and prompt γ rays detected in Crystal Ball will provide information on the nature of the reaction and the excitation of the fragment. Finally, it will be outlined how neutron and fragment data is combined to produce relative energy spectra that will enable the discussion of unbound states (see chapter 5 for results).

4.1 Beam particle ID

The impingement of the ^{48}Ar primary beam on the Beryllium production target will create a broad range of different isotopes that need to be identified in order to select the right secondary beam to study the reactions of interest. To this end, we use the particle identification plots (PID) (see Figure 4.1). The y-axis corresponds to the charge of the particle Z and the x-axis is the mass-over-charge ratio , A/Q, that is determined as the track of the particle through the FRS dipole magnets, where the $B\rho$ were nominal values, as described by the Bethe-Bloch equation:

$$-\frac{dE}{dx} = \frac{4\pi Z^2}{m_e c^2 \beta^2} \frac{N_a Z \rho}{M_u} \left(\frac{e^2}{4\pi\epsilon_0}\right)^2 \left[ln\frac{2m_e v^2}{I} - ln\left(1-\frac{v^2}{c^2}\right) - \frac{v^2}{c^2}\right] \tag{4.1}$$

where x is the path travelled by the particle, m_e and e the electron's rest mass and charge

respectively. ρ is the density of the target, M_u the molar mass, ϵ_0 the vacuum permittivity, I the beam excitation potential, , N_a the Avogadro's number, c the speed of light, v the velocity of the particle and $\beta = v/c$.

To obtain the charge, we use the energy loss recorded before the target in the PSP, which is proportional to the square of the charge state Q. Since the ions coming from the FRS are fully stripped, the proton number Z and the charge state Q are equal and can be easily measured.

The resulting incoming PID plot is presented in Fig. 4.1 for setting 4, where each blob represents a different incoming isotope.

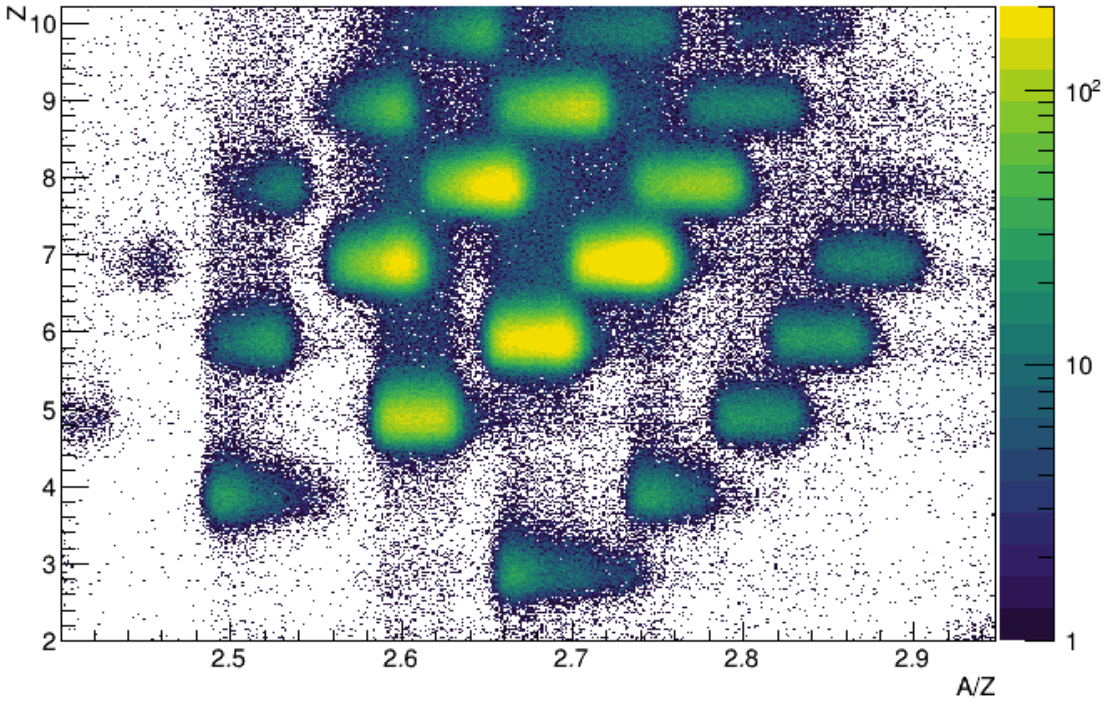

Figure 4.1: Incoming PID plot, presenting the mass-over-charge ratio A/Z, determined using the tracking information of the particle through the FRS dipole magnets where the $B\rho$ are nominal values, versus the proton number Z, extracted from the energy loss recorded in the PSP before the target. Each blob represents a different incoming isotope.

4.2 Recoil ID

For the identification of the outgoing isotopes, a two-step process is carried out. Firstly, we identify the charge of the isotope of interest using a combination of energy loss and time-of-flight measurements. Secondly, we perform mass spectrometry for the charges of interest previously selected in order to gate on the masses of interest. In the present subsection the procedure will be unfolded in detail.

4.2.1 Charge Identification

In order to determine the charge of the isotopes of interest, we use two detection systems after the target that record energy deposition, namely the SSDs and the TFW, which measure energy loss. For the latter, the calibration was performed by Christoph Caesar [83]

For the SSDs, once the baseline subtraction is carried out, energy and position of traversing particles are extracted. Charge varies with the position within a single strip, hence the energy depends on the position. According to M. Holl [80], the position of the hits seem to have a shift towards the edges of the strip. Hence, a correction for this effect should be performed in order to get the actual energy and position. For this purpose, a gainmatching routine customised for each run written by M. Holl was applied. It corrects the different gains of the strips by fitting a Gaussian distribution to the energy loss at different positions. The outcome is the inverse of the mean of the distribution. Finally, the energy loss is plotted against the position within a strip as shown in Figure 4.2. Only the k side was taken into account since it has significantly better resolution than the s side for both Ss03 and Ss04. The description of the whole correction procedure can be found in detail in [80].

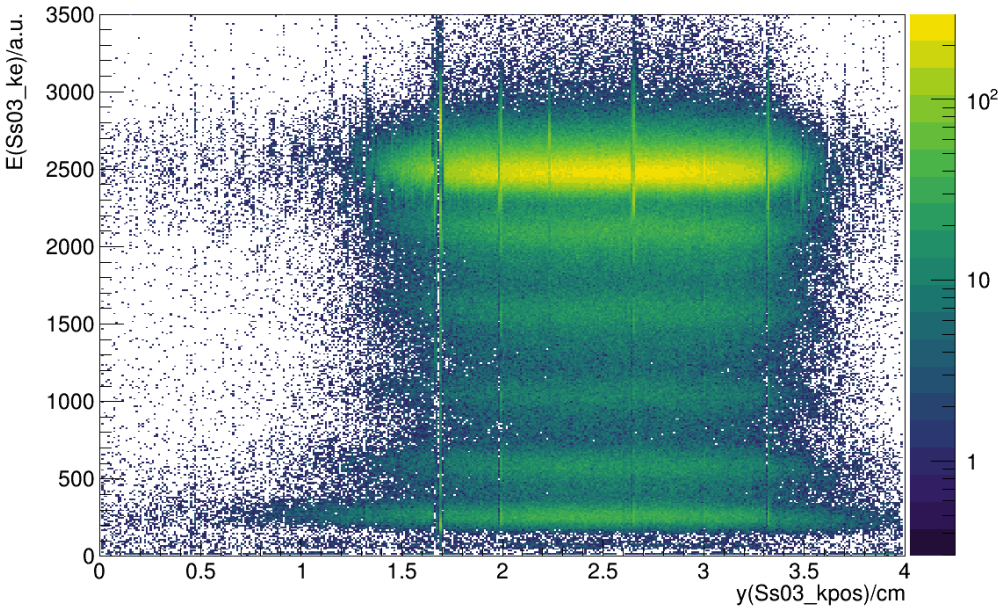

Figure 4.2: Ss03 k-side after gainmatching for run 427.

Once the gainmatching correction is performed, the identification of the outgoing fragments can be carried out by combining the information recorded by the TFW and DSSSDs after the target. The PID plots shown in Fig. 4.3 and top row of Fig. 4.5 are produced by the energy recorded from the TFW on the y-axis and the k-side of the first DSSSD detector after the target (Ss03_k) on the x-axis for data collected from ^{17}N (Fig. 4.5 left), ^{19}N (Fig. 4.3 and Fig. 4.5 middle) and ^{21}N (Fig. 4.5 right) beams.

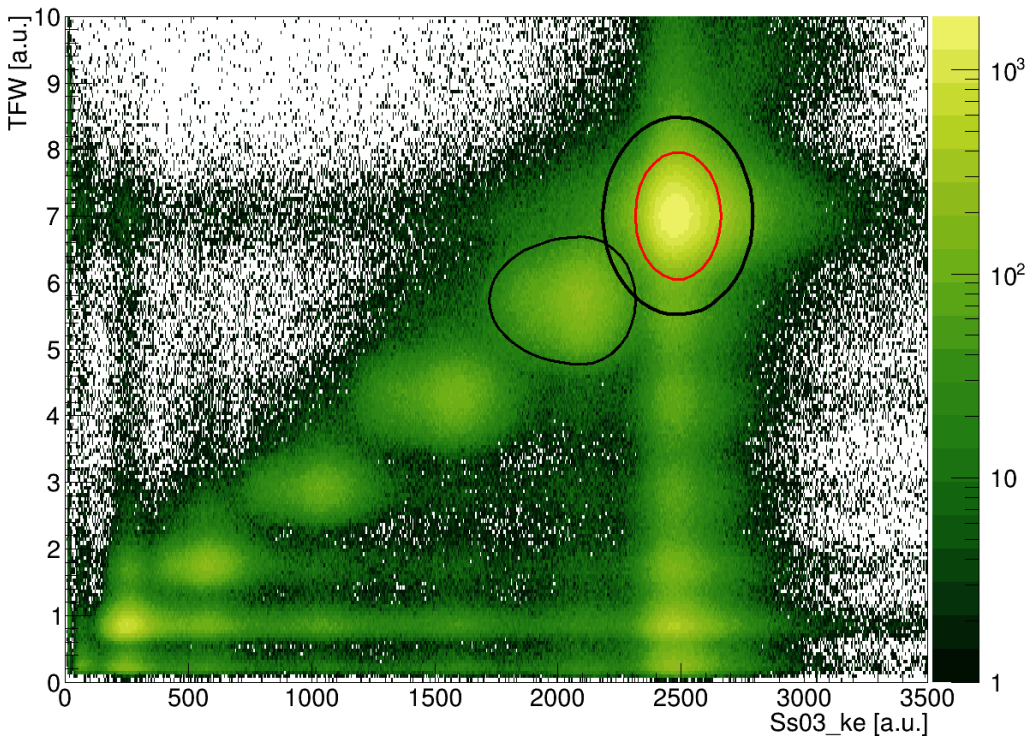

Figure 4.3: Outgoing fragment charge identification plot for setting 4, where the energy observed in the TFW is plotted versus the versus the energy recorded in the front side of the first DSSSD after the target (Ss03_k).

This intermediate step before the mass spectroscopy consists of charge selection. For this purpose, two graphical cuts are required to select Z=6 and Z=7 recoils. The selection of Z=6 recoils is the semi-symmetrical ellipse located around the coordinates (6, 2000) in Figures 4.3 and 4.5. The gate for Z=7 fragments is located at around the coordinates (7, 2500) and it corresponds to the unreacted ions from the incoming beam, which has been assumed as a close approximation to the actual incoming ions as explained in detail by J. Kahlbow [84]. In these plots, the outer ellipse marked in black is the graphical cut applied to the data. The inner ellipse indicated in red is the gate used for definitive charge identification, i.e. only the events lying within those limits are selected when imposing Z=6 or Z=7 conditions later in the analysis.

For the ellipse reconstruction, first, the centre of the ellipses for each charge has to be determined. For this, we set limits on the area of interest on the outgoing PID plot, where both the Z=6 and Z=7 lie, and then perform a projection on both axes and fit each peak to a normal distribution in order to obtain the parameters, namely the mean μ_{Ss03_k}, μ_{TFW} and the standard deviations σ_{Ss03_k}, σ_{TFW} on x- and y-axis. The centre of the ellipses will be provided by the centroid of those projections (μ_{Ss03_k}, μ_{TFW}), while the width a and height b parameters of the ellipses will be typically twice the standard deviation, as indicated in Table 4.1.

		$Z=6$	$Z=7$	
a (x-axis)	left	3.5	2	$\cdot\sigma_{Ss03_k}$
	right	2		
b (y-axis)		2	2	$\cdot\sigma_{TFW}$

Table 4.1: Width and height control parameters for the elliptical charge gates.

However, it is worth noting that an asymmetric ellipsoidal cut is applied to the $Z = 6$ charges due to the break-up contamination in the in-flight trajectory that elongates the different charges along the y-axis . In order to construct these asymmetric ellipse we use two half ellipses with the same centre and height, but longer width on the left sided half. The control or nominal ellipse parameters are shown in Table 4.1, following those used by Ina Syndikus [85]. A clear evidence of the in-flight break-up phenomenon of the unreacted beam from the Ss03 to TFW can be clearly appreciated on the vertical line along E_{Ss03}=2500 a.u.

In addition, several concentrical ellipses with different sizes, shown in Fig. 4.4, were generated in order to allow flexibility when selecting different charge gates and test their impact on the γ spectra and the cross section measurements. The second largest ellipses in these sets correspond to the black ellipses presented in Figure 4.3 and described by the parameters in Table 4.1, the other ellipses are drawn using the multiplication factors in Equation 4.2.

$$M = [1., 1.2, 1.5, 2., 0.9, 0.8, 0.7, 0.5] \tag{4.2}$$

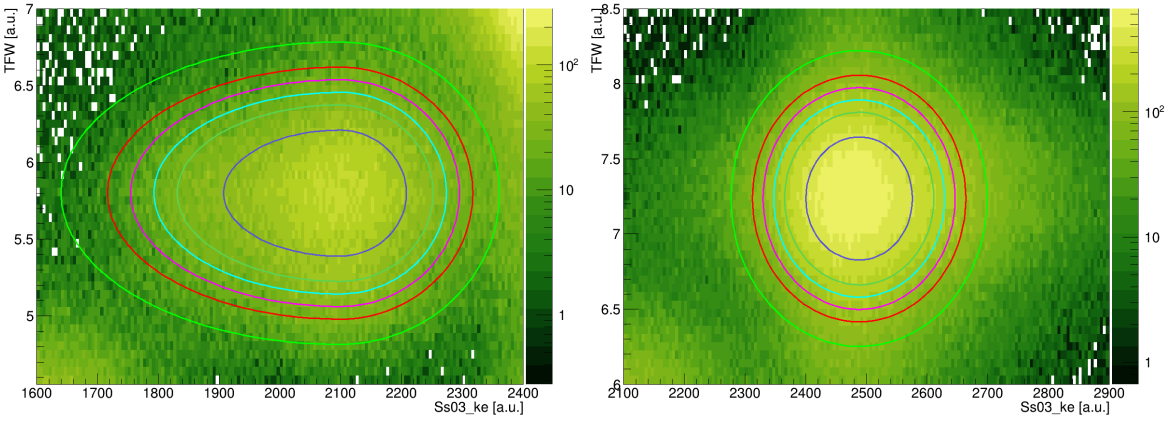

Figure 4.4: Different gates available for both charge Z=6 (left) and Z=7 (right). Red gates correspond to the ellipse defined by parameters listed in Table 4.1, while the rest are scaled according to the parameters in Equation 4.2 (ellipses 1.5 and 2 times larger not shown).

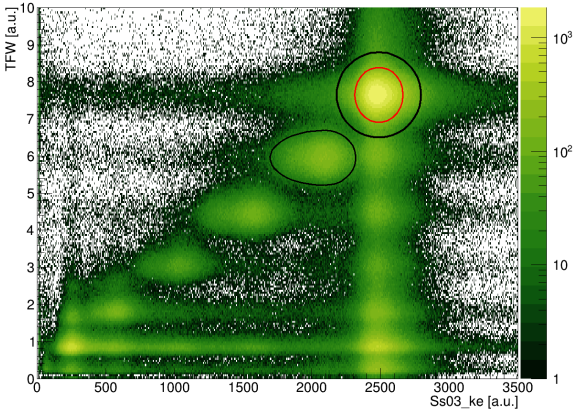

(a) Charge ID for recoils produced from ^{17}N beam

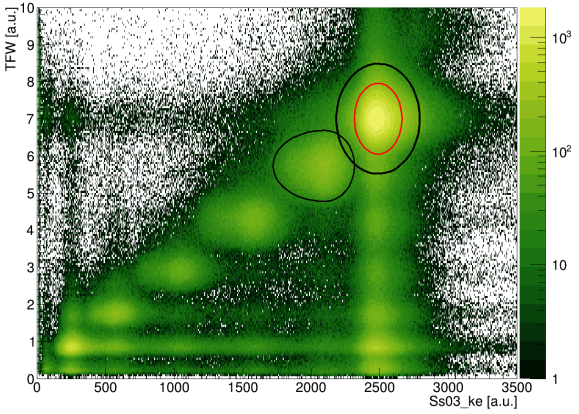

(b) Charge ID for recoils produced from ^{19}N beam

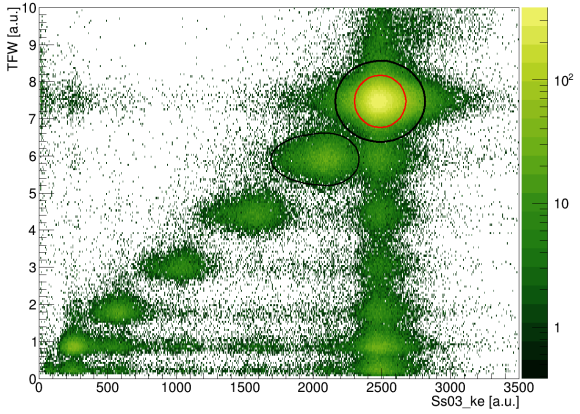

(c) Charge ID for recoils produced from ^{21}N beam

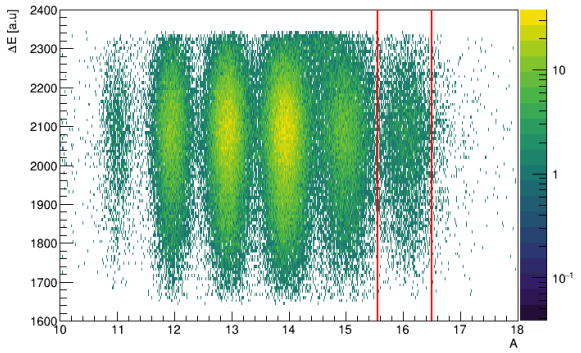

(d) Mass selection for ^{16}C

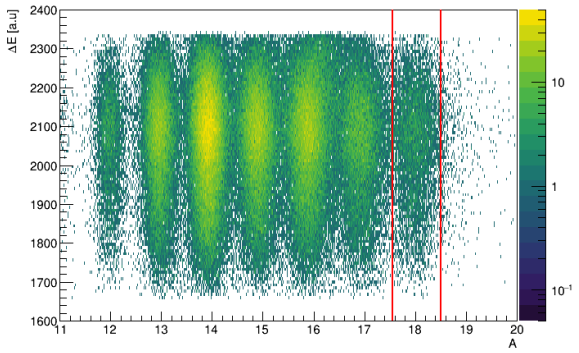

(e) Mass selection for ^{18}C

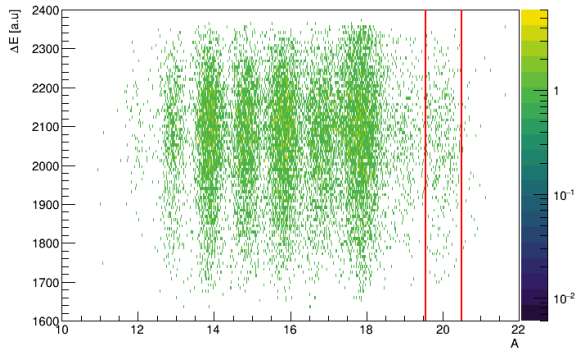

(f) Mass selection for ^{20}C

Figure 4.5: Outgoing and mass ID plots

4.2.2 Mass Spectroscopy

Subsequently, the mass spectroscopy was performed in order to separate the isotopes of interest. To identify the outgoing isotopes, the mass of the fragments of interest has to be determined. For this purpose, *Ralf's Tracker*, a customised software created by Ralf Plag for the R^3B experimental data under the land02 framework [86], was used. This programme uses position and time data from different detectors of the whole setup in order to reconstruct velocity and flight path of the fragments by combining position and time with ALADIN's magnetic field according to Equation 3.2.

Depending on the mass A, the velocity β measured from the target to the TFW, and the mapping of the magnetic field B, the magnetic rigidity $B\rho$ can be extracted for a given trajectory and current I. The x-component is extracted from the GFIs and since no information on the y-component is available, as mentioned in Section 3.7.1, it is then obtained from the TFW. The calibration of the tracker depends on the real position of the detectors at the time of the experiment. The reconstructed track searches for a minimum in the distance between the fragments impinging on the detectors calculated by the *Tracker* and the actual positions recorded by the detectors.

The mass identification plots are shown in the bottom row of Figure 4.5 and in Figure 4.6 where it can be appreciated that the masses are well separated with minimum overlap between neighbouring masses.

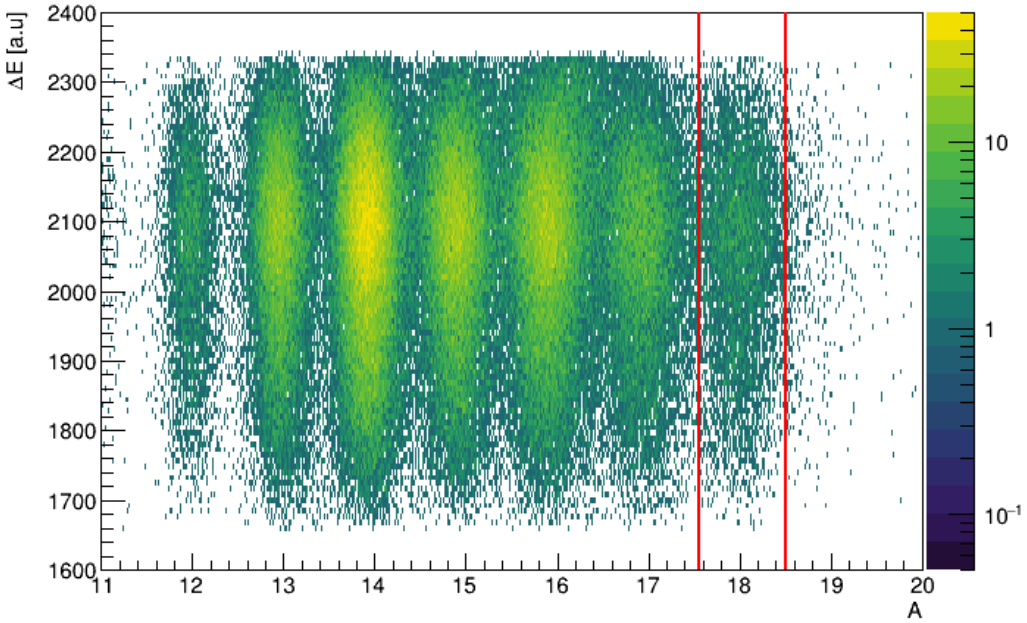

Figure 4.6: Outgoing fragment mass identification plot for charge $Z = 6$ stemming from the ^{19}N beam. The red lines exemplify a mass selection on $A = 18$.

4.3 Protons

As mentioned in Section 3.5, Crystal Ball (XBall) double energy readout allows the discrimination between protons and γ rays. In addition, the position of the detecting crystal will provide information on the scattering angle. However, the position is randomised within the full active area of the crystal before extracting the associated θ and ϕ angles. The energy needs to be calibrated and addback reconstructed (see Section 4.4.1 regarding the addback method applied, in addition γ rays also require to be Doppler corrected, see Section 4.4.2). A comprehensive description of these procedures will be provided in the following subsections.

First, the signals produced by XBall need to be sorted into protons and γ rays. Due to their higher energy deposition in the crystals, the PMTs cannot resolve the energy deposited by protons with the energy readout intended for γ rays and are recorded as infinite values. Therefore, overflow values in the γ readout are deemed as proton hits.

Next step is the calibration of the Crystal Ball readouts. For such a purpose, the proton signal is calibrated using muons from the cosmic radiation measured off-spill during the experiment and in calibration runs intended to measured background cosmic rays. The energies recorded in these runs is then compared to cosmic-ray simulations. Further details on these calibrations can be found on Ronja Thies Masters dissertation [87].

4.3.1 Scattering angles

The position of the detecting crystal will provide information on the scattering angles: θ and ϕ. For that purpose, the hit position of the incoming beam on the target and the direction of the beam and fragment are disregarded, and we assumed the γ rays are emitted from a fragment in the centre of the target moving in the Z direction. In this regard, it is worth saying that the scattering angle of the fragment is never more than $0.8°$, and its effect will cancel out due to the rotational symmetry around the Z-axis and sufficient statistics.

However, the maximum resolution that the detector can achieve corresponds to the minimum solid angle that the crystal covers with respect to the target. Since the active area of a crystal covers a rather large solid angle, the resolution does not allow to determine precisely the position of a hit within a single crystal. Therefore, in order to have realistic and continuum angular distributions, the hit positions are randomised over the whole active area of the crystal fired. Both the polar angle θ and the azimuthal angle ϕ in the laboratory frame can be determined by the well-known geometrical locus of the crystals. Once this is done, the angles of the fired crystals are sorted in new designated arrays for θ and ϕ.

4.3.2 Angular correlations

In order to select certain reaction channel, we need to apply some gates on characteristic observables of that channel. A way to guarantee we have QFS $(p, 2p)$ reactions is studying the proton angular correlations, which are expected to have well known and defined distributions. Protons from knockout reactions, on the other hand, do not show any particular distribution and can be emitted at forward angles escaping detection in XBall.

As mentioned in the Section 2.5.2, for pure QFS processes we expect two protons scattered in opposite directions in ϕ with an opening angle θ of nearly 90° between them. Fig. 4.7 shows the opening angle distribution of events where exactly two protons were observed in coincidence with a ^{18}C recoil. The mean value of the distribution is 82.4°, consistent with predictions for QFS.

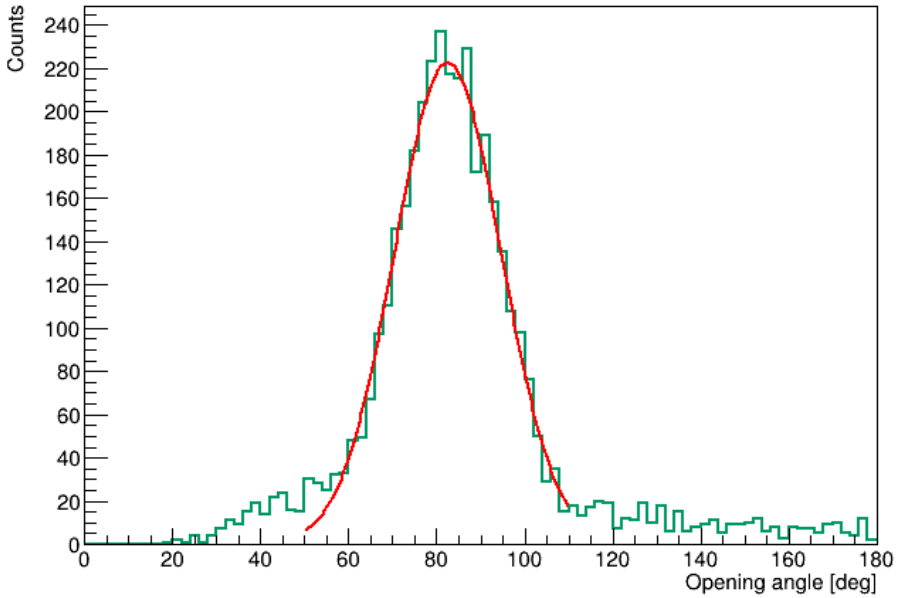

Figure 4.7: Opening angle between the two protons scattered in the QFS reaction for exactly two protons and XB Sum Tbit

Therefore, as an evidence of the QFS events, proton angular correlations were studied. Besides, we also need to differentiate between the QFS reactions with the protons (H atoms) from the knockout reactions with the C atoms. Figure 4.8 present the azimuthal (top) and polar (bottom) angular correlations. The azimuthal angles ϕ show back-to-back scattered protons and the polar angles θ exhibit the protons opening scattering angle at around $\Delta\theta \sim 90°$, which is a touchstone for these reactions at this energy range. The correlations shown are for setting 4 with the CH_2 target.

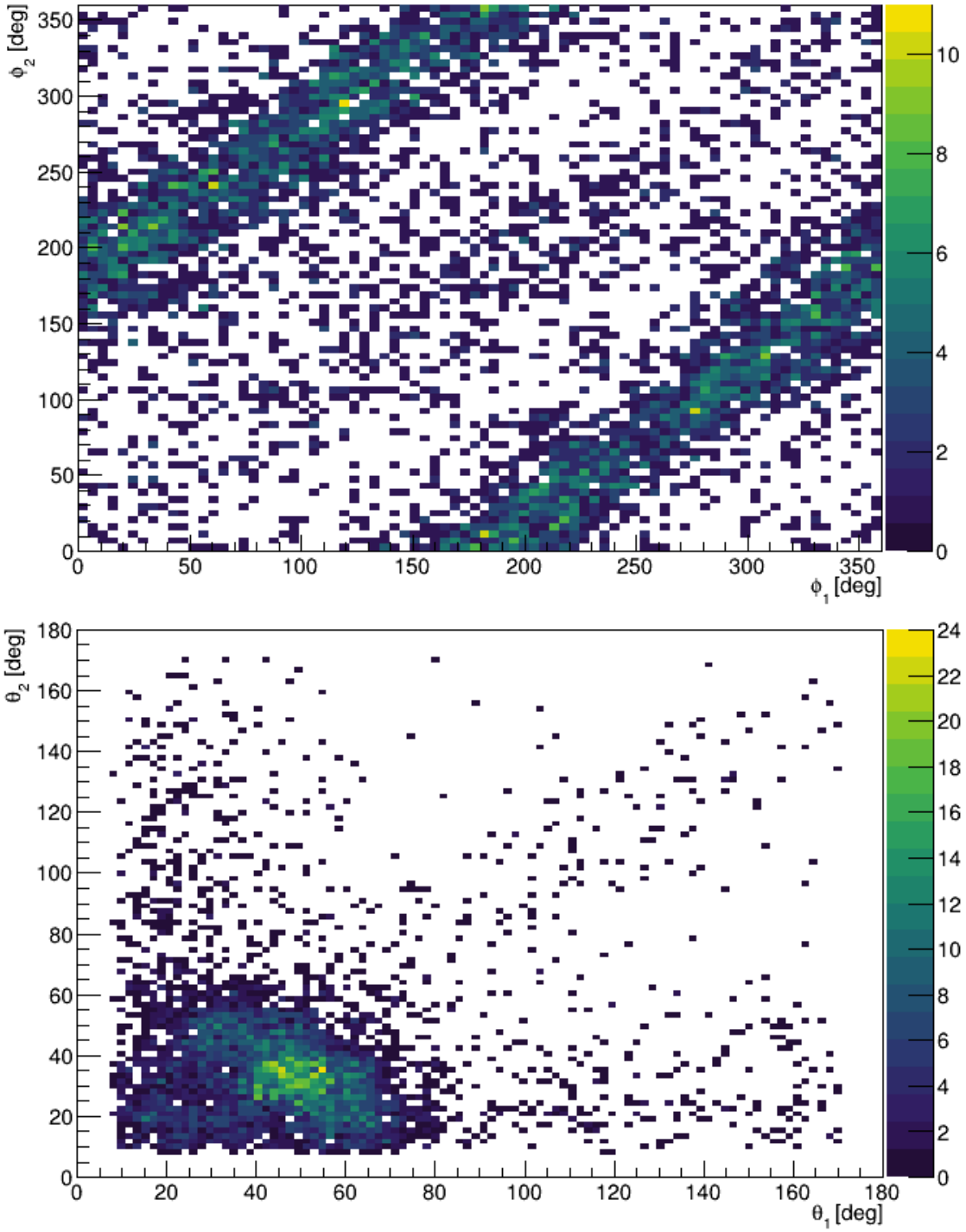

Figure 4.8: Angular correlations in the laboratory frame for the two protons observed in coincidence with a ^{18}C fragment, following the QFS $^{19}N(p,2p)^{18}C$ reaction on the CH_2 target. The azimuthal distribution ϕ (top) shows the expected back-to-back scattering, while the polar angles θ (bottom) shows the scattered protons at $\Delta\theta \sim 90°$.

4.4 γ Rays

In order to study the bound states, the γ-ray spectra were analysed. The energy calibration of the γ rays for the S393 experiment was performed in a single-crystal basis similarly as the calibration of the protons (see Section 4.3) using ^{60}Co, ^{56}Co, ^{22}Na and ^{88}Y. Since these sources were the only ones available at the time, calibration was performed up to 3.3 MeV, extrapolation of this calibration to higher energies has therefore higher systematic uncertainties.

The time dependency of the energy from the prompt γ rays stemming from the reaction products was analysed for all the settings. Most of the γ rays detected accumulate in a $\sim$40 ns window around $t = -180$ ns, as observed in Fig. 4.9. Therefore, a time window for prompt emission was defined from $t_{min} = -200$ ns to $t_{max} = -160$ ns (depicted in red) for all settings. Walk effects are not observed due to the CFD used in every single crystal (see Section 3.5) .

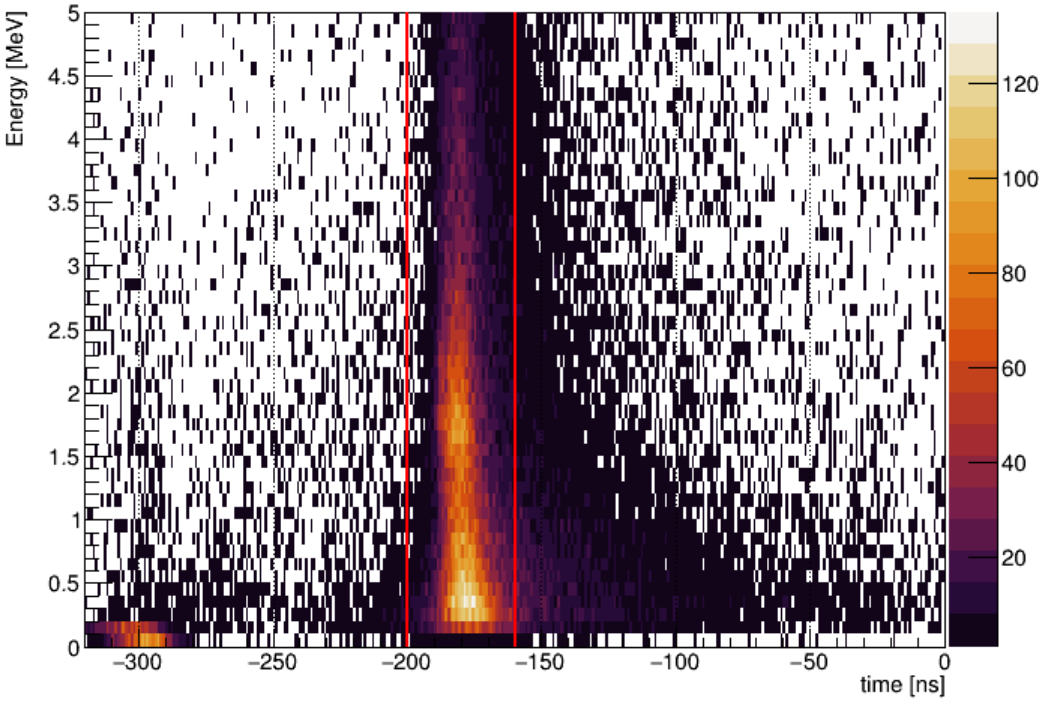

Figure 4.9: XBall γ-ray energy over detector time.

4.4.1 Addback

Ideally an incoming particle, whether it is a proton or a γ ray, will interact with a single crystal depositing its full energy, therefore the resulting signal will be proportional to its energy. However, sometimes the energy is not deposited in a single crystal but in several

(this is specially true for high energy γ rays due to Compton scattering), resulting in the total energy being splitted in different signals. In order to take this into account , a process called addback is applied to reconstruct the total energy of the incoming particle, improving the photopeak efficiency.

There are different addback methods, the difference between them lies in the criteria used to decide the crystals whose signal should be added to a given hit. The most common addback routines are described here:

- **First neighbour addback:** only energies deposited in neighbouring crystals are summed to the hit energy (Figure 4.10, left).
- **Second neighbour addback:** energies observed in first neighbour crystals and next neighbour crystals are summed to the hit, see middle schematic in Figure 4.10.
- **Cluster addback:** adds the energies in neighbouring crystals, then keeps adding energies if they are next a previously added crystal and within a predefined addback range, see right schematic in Figure 4.10.
- **Calorimeter mode:** all signals are summed, regardless of where the energy deposition was. This method was not used in the present analysis, because it assumes the γ-ray multiplicity is never higher than one, which is not the case.

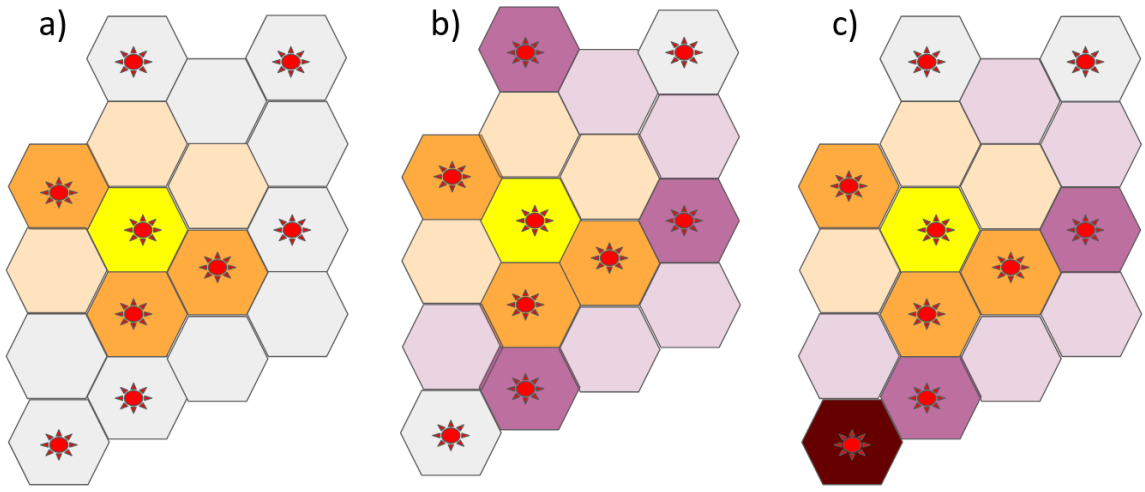

Figure 4.10: Different addback methods considered. Hexagons represent crystals and red stars depict a valid signal -above the threshold. Crystals in yellow crystal represent the highest energy deposition. In first-neighbour addback (a) only the immediate neigboring crystals (orange) are scanned for signals and are summed up to the hit. In the second neighbour addback, nearest (orange) and the second-nearest (purple) signals to the centre are added to the total energy of the hit. Cluster addback (c), following the same approach from b), the algorithm continues so forth under the condition that the next signal has to be immediately contiguous and remain within the defined addback range.

In all these addback methods, after the protons and gammas are discriminated, the energies are sorted in decreasing order. The addback routine will then take the highest energy and deem it as a hit. Afterwards, it will look for the crystals that belong to this hit according to the addback method used. The energies in those crystals will be summed up to the hit. They are above an 80 keV threshold set to avoid adding noise to the γ rays, and flagged as a used energy in order to make sure it is crossed out of the list and it is not used again in case any of those crystals falls within the addback range of another hit. Finally, the addback-reconstructed energy is associated to the scattering angles θ and ϕ corresponding to the highest energy deposition. This addback routine is applied again to the next highest energy still unused, scanning proton hits before moving to γ rays in order to remove proton noise from the γ spectra, although it was observed that the effect of proton addback was negligible.

In Figure 4.11, I. Syndikus [85] shows the difference between the different addback methods when applied to ^{16}C cascade from the 4^+ (1.762 and 2.374 MeV γ rays from the $2^+ \rightarrow 0^+$ and $4^+ \rightarrow 2^+$ respectively). We can see that the main difference is that the sum peak at 4.136 MeV increases when using second neighbour addback, but first neighbour addback and cluster addback yield pretty similar results. This suggests that extending the addback range to a second row of neighbours does not have a significant effect on the photopeak integrals, but increases the risk of artificially reducing the multiplicity by adding two distinct γ rays together as a single if they are observed closed to each other. Therefore, a first neighbour addback routine was written and used in the present analysis.

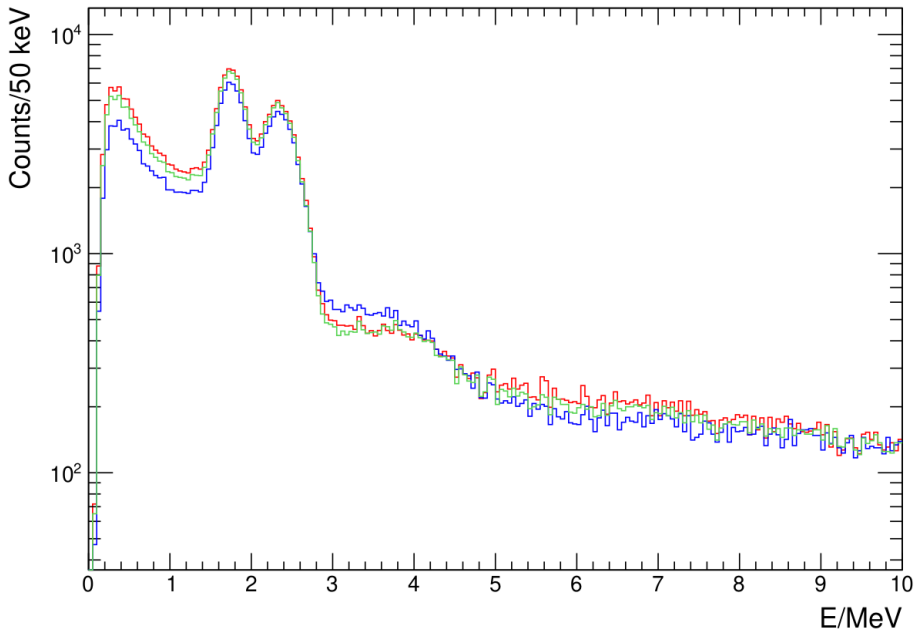

Figure 4.11: Spectrum of ^{16}C with first neighbour addback (red), second neighbour addback (blue) and 2-step cluster addback (green). There is a clear increase in the sum peak at 4.1 MeV for the second neighbour addback.

In order to have a clear understanding of the performance, this addback routine was applied to a ^{60}Co calibration run in which the source was located on the right side of Xball. Figure 4.12 shows ^{60}Co γ spectrum with no addback in blue and with first neighbour addback routine discussed previously in red. We can see that the addback-reconstructed spectrum reduces the background at lower energies (between 0.1 and 1 MeV) while increasing the integral under the γ peaks. That is because the addback reconstructs scattered γ rays that deposited their energy in 2 or more crystals, and therefore uses 2 or more low energy signals (0.1-1 MeV) to reconstruct the full photopeak energy, enhancing the photopeak efficiency and peak-to-background ratio.

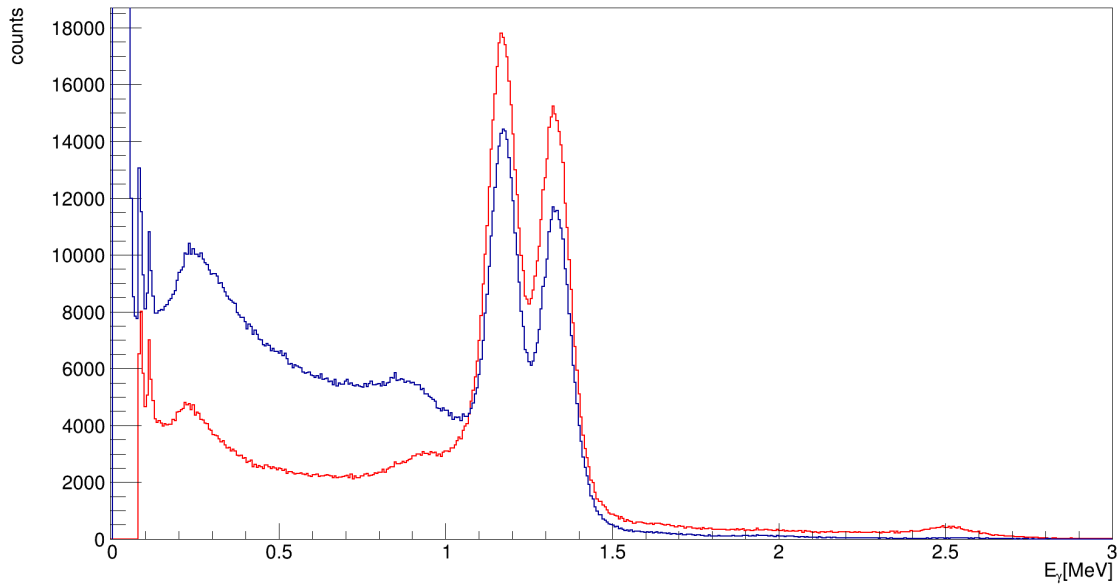

Figure 4.12: Spectrum of the ^{60}Co with no addback (blue) and with the addback applied (red).

4.4.2 Doppler correction

The energy observed in the laboratory for a γ ray must be corrected as it is affected by the Doppler shift, due to the velocity of the emitting nucleus with respect to the detector. For a nucleus travelling at a velocity β and emitting a γ ray observed in the detector as E_{lab}, a Doppler correction should be computed as follows:

$$E_{cm} = E_{lab} * \gamma(1 - \beta \cdot \cos(\theta_\gamma)) \tag{4.3}$$

where E_{cm} is the energy in the centre-of-mass and θ is the angle of emission with respect to the path of the emitting nucleus, as it can be seen on the Equation 4.3. Energies E_{cm} for forward scattered γ rays will be $E_{lab} > E_{c.m}$ while for back scattering will be $E_{cm} > E_{lab}$. As mentioned earlier, the scattering angle for the addback reconstructed energy corresponds to the centre of the cluster, thus the highest energy deposition in the cluster.

4.5 Neutrons

The neutrons evaporated carry the information required to study the unbound states. In the current work, one-neutron evaporation channels are analysed using the corresponding relative energy spectra which are reconstructed by the invariant mass method.

4.5.1 Neutron Shower Algorithm

Neutrons can produce a shower of secondary particles that needs to be identified and tracked back to the initial neutron hit. This task is performed by the shower algorithm implemented in the land-02 software package [88], returning θ, ϕ and β of the neutron from the energy, position and time measurements recorded in LAND. In this section, the relevant details of this shower algorithm will be briefly outlined.

LAND is located at the 0° line, and therefore the magnetic field of ALADIN ensures that charged particles are deflected and only uncharged particles hit LAND: neutrons and γ rays. Helpfully, γ rays and neutrons can be identified using time of flight measurements, as indicated in Figure 4.13. Since there is a small but not negligible chance of a γ ray producing secondaries, the shower algorithm searches for secondaries within a short time window and a small cone behind the first hit.

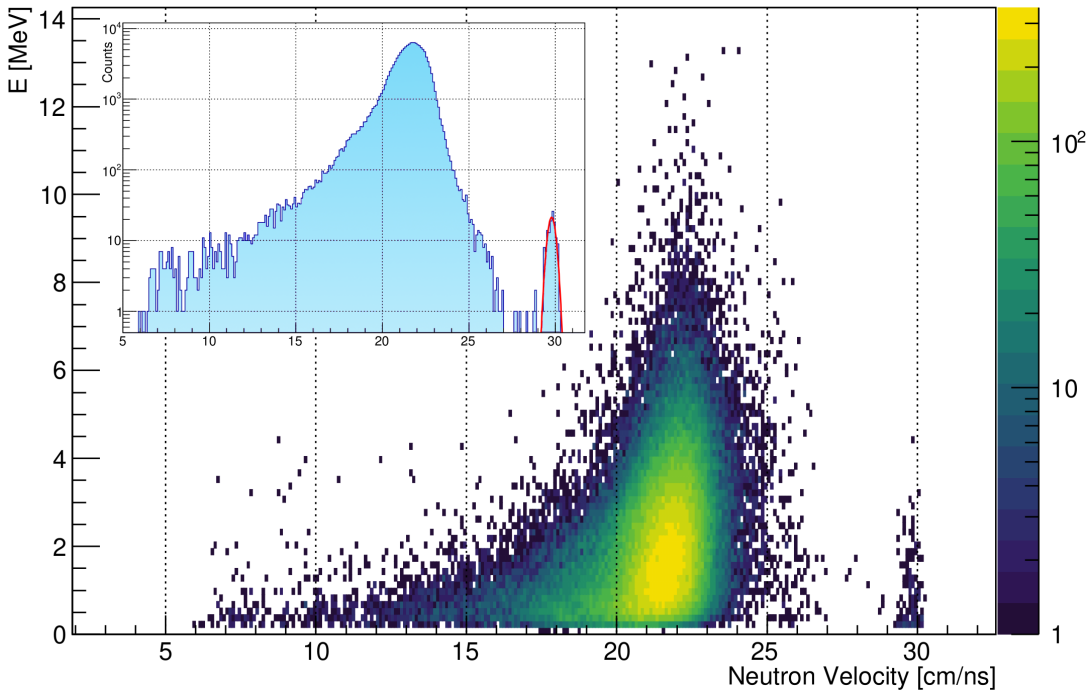

Figure 4.13: Neutron energy deposition vs neutron velocity, the inset shows the projection on the velocity axis where we can see the neutron distribution is found around 22 cm/ns and the γ peak can be observed at the speed of light (30 cm/ns), which is due to photons coming from the target.

Primary hits are the most important to characterize a neutron, as they carry the time and position information required to extract the scattering angles θ and ϕ, and the velocity β. In addition, the number of primaries provides the neutron multiplicity. Hence, the most sensible task is assessing which hits are primaries and how many there are in an event-by-event basis. This task is done by the following procedure: the first hit is assigned as a primary and remaining hits are scanned for secondaries. If by the end of this process there are still remaining hits that have not been assigned to a shower, the fastest is identified as primary and a search for secondaries starts. This process is repeated until all hits are sorted as primary or secondaries. Finally, if the neutron multiplicity is bigger than one, the distance between all secondary hits and the primaries is checked to ensure the secondary hits are assigned to the nearest primary hit.

Regarding the secondary search, for given hit to be designated as a secondary belonging to a determined neutron shower characterized by a certain primary hit, it has to meet the following conditions:

- All hits within a sphere determined by the time resolution of LAND, σ_t, and the speed of light are deemed as secondaries, since causality cannot be established between those hits.
- The distance between the secondary candidate and the primary has to be no larger than the maximum distance R_{cyl}.
- The time interval between the secondary candidate and the primary hit must be shorter than T_{max}.
- A cylindrical cut is applied on the positions of the secondary candidates, defined by a length in the beam direction, Z_{max}, a length opposite to the beam direction, Z_{min}, and a radius R_{cyl}. A hit is considered a secondary if it is located within this cylinder and the velocity required to reach its position from the primary hit location is smaller than the speed of light.
- The velocity required to connect the secondary candidate with the primary hit is smaller than v_{Fermi}, which is the velocity associated with the Fermi momentum of a nucleon inside a nucleus, and the relative distance between them hits is negative (meaning that the secondary travelled in a backward direction). This condition is called '*backward Fermi*'.
- The last condition checks if the neutron undergoes forward elastic scattering by comparing the momentum that associates the two neutrons to the momentum of a forward scattering process.

These parameters for the secondary search, presented in Table 4.2, are the standard parameters in the land02 software package and have a direct impact in the identification of primary neutrons and therefore in the neutron multiplicity. They have been optimised in such a way that the neutron multiplicity is not artificially decreased by misidentifying a primary as a secondary nor increased due to fake primary hits.

Neutron shower parameters	
distance between target and LAND	1250.0 cm
neutron time resolution σ_t	0.8 ns
secondary neutron radius r_{sec}	50.0 cm
neutron time T_{max}	10.0 ns
cylinder min. length in beam direction Z_{max}	40 cm
cylinder max. length in beam direction Z_{min}	-12.0 cm
cylinder radius R_{cyl}	29 cm
neutron Fermi velocity v_{Fermi}	8.0 cm/ns

Table 4.2: Neutron shower algorithm parameters.

4.5.2 Neutron Detector Response

The response of a detector to a monoenergetic source provides information such as the distribution of the energy over the channels of the detector according to the gain and energy resolution. The resolution function depends on different variables such as the threshold, the high voltage (HV) and, more particularly, the neutron shower algorithm.

A Monte Carlo Event Generator designed for LAND (LEG) is used to simulate the detector response matrices for each channel of interest and allows to extract the dependency of the resolution with the reconstructed relative energy (see Section 4.6 for details on the relative energy), shown on Fig. 4.14. This simulation uses actual data of hits recorded by LAND and was developed at TU Darmstadt by D. Rossi. LEG discriminates between the generated neutrons and the simulated ones.

The detector response matrices obtained are normalised to the number of simulated events. These matrices depend on the beam velocity and mass of the decaying nucleus. Since the aim of this work is to reconstruct the real energy, the reconstructed relative energy is used as a parameter of the response in order to obtain the detector response matrix, which is determined by real neutron data from calibration runs. Usually the experimental response is based on that of each detector in a whole setup. A neutron trigger was used (LAND Tbit) and no acceptance cut was seen in the fragment distribution.

In order to obtain the response matrix for a given one-neutron channel, one has to plot one neutron generated vs. one neutron tracked (g1t1). After the matrix of a channel of interest is obtained, a Y-Projection is computed at regular steps of 50 keV in order to fit

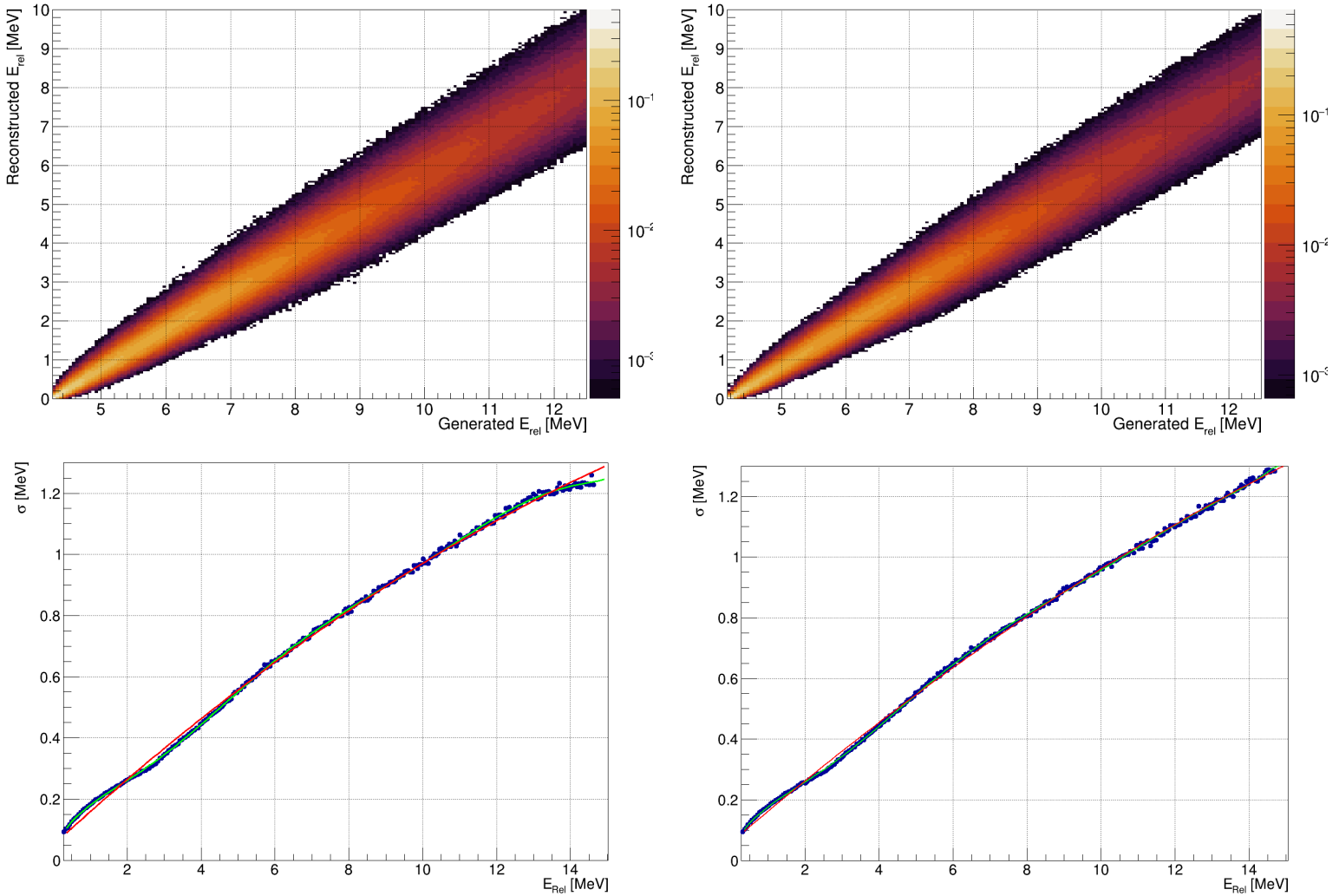

Figure 4.14: Top panels: LAND response matrices for $^{16}C \rightarrow ^{15}C+n$ (left) and $^{18}C \rightarrow ^{17}C+n$ (right). Bottom: Resolution of the tracked energy in function of the generated relative energy for $^{16}C \rightarrow ^{15}C+n$ (left) and $^{18}C \rightarrow ^{17}C+n$ (right).

the reconstructed energy obtained. The standard deviation (σ) of each fit was subsequently plotted vs. the relative energy and then fitted to different curves: linear, polynomial order 2 and higher order polynomials. In Figure 4.14 (bottom panel) the resolution is plotted against the energy for ^{15}C+n (left) and ^{17}C+n (right) respectively. In both cases, a linear fit is drawn in red and a higher order polynomial in bright green. In both cases, the higher order polynomial was chosen since it describes the correlation more accurately. This parameterisation of the standard deviation with the relative energy will later be used when fitting resonances to the experimental relative energy spectra (see Section 4.8.1).

LAND coverage is of $\approx$ 80 mrad and since all reaction particles in inverse kinematics are forward-focused due to the Lorentz boost. The acceptance of LAND is 100% for neutrons of up to $\sim$3 MeV but decreases at higher energies [88]. The combined effect of the efficiency and the acceptance was obtained by performing the integral of the projection of the full range of the matrix over the Y-axis. It can be divided in two parts. The first one is the slightly increasing segment for low energies up to $\sim$2.7 MeV, where the acceptance is 100% (see Figure 4.15). Above this energy not all neutrons evaporated hit LAND since the neutron scattering angle increases as the relative energy increases, explaining the exponential decrease observed.

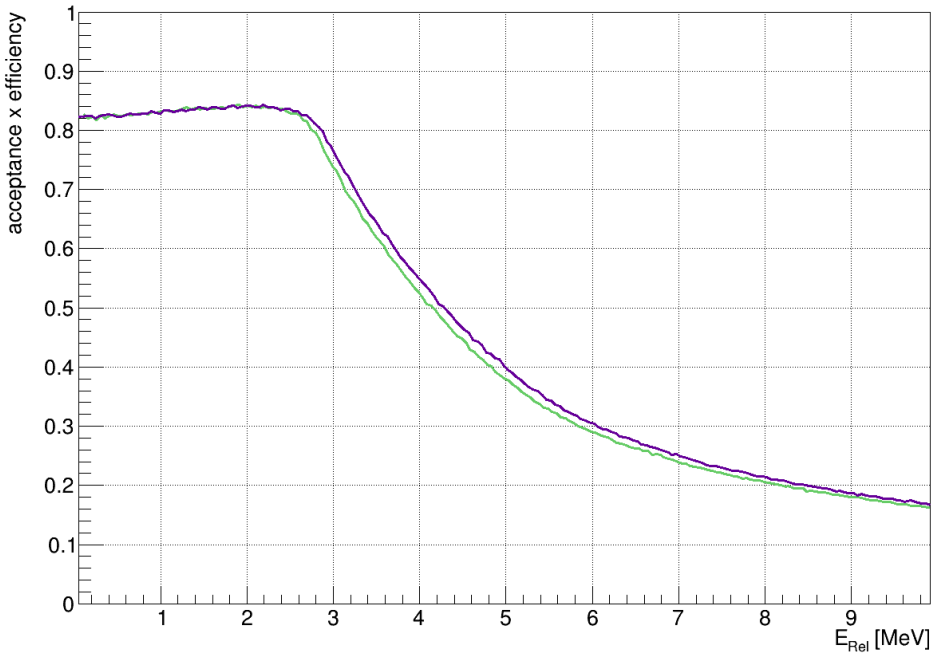

Figure 4.15: Efficiency × acceptance of LAND for $^{15}C + n$ (violet) and $^{17}C + n$ (green)

The efficiency of LAND is affected by the broken paddles. In this experiment, those that were broken are listed in Table 4.3 and were also deactivated on the LEG simulation for the efficiency calculation (see Section 3.7.3).

plane	1	1	2	6	6	9	9	9	10
paddle	1	20	19	6	13	1	12	20	all

Table 4.3: List of broken paddles of LAND. Plane 10 worked correctly, however, the readout was carried out by TacQuila and was not considered for this analysis.

4.6 Invariant-mass method

In order to reconstruct the unbound state and to determine its excitation energy, the invariant-mass method is suitable for such task, previously used in several works on unbound states [55, 83, 89]. The invariant mass M_{inv} of a system formed by n particles is a physical quantity that remains constant under Lorentz transformations and can be described via the square of the total four-momentum of the system:

$$M_{inv}^2 = \left(\sum_j P_j\right)^2 = E_{tot}^2 - P_{tot}^2 = \left(\sum_j^N E_j\right)^2 - \left(\sum_j^N p_j\right)^2 \tag{4.4}$$

where P_i are the total four-momentum, E_{tot} and P_{tot} are the total the total energy of the system and the total three-momentum respectively, E_j and p_j are the total energies and momenta of the system's constituents. From Equation 4.4 it follows

$$M_{inv} = \sqrt{\sum_j^N m_j^2 + \sum_{j\neq k}^N E_j E_k - \sum_{j\neq k}^N p_j p_k cos\vartheta_{jk}} \tag{4.5}$$

using the relativistic equations of energy $E_j = \gamma_j\, m_j\, c^2$ and momentum $p_i = \gamma_j\, m_j\, \beta_j\, c$ on Equation 4.5, the invariant mass can be expressed as:

$$M_{inv} = \sqrt{\sum_j^N m_j^2 + \sum_{j\neq k}^N \gamma_j\gamma_k m_j m_k (1 - \beta_j\beta_k cos\vartheta_{jk})} \tag{4.6}$$

The relative energy is obtained by subtracting the masses at rest of the decay fragments:

$$E_{rel} = M_{inv} - M_0 = \sqrt{\sum_j^N m_j^2 + \sum_{j\neq k}^N \gamma_j\gamma_k m_j m_k (1 - \beta_j\beta_k cos\vartheta_{jk})} - \sum_j^N m_j^2 \tag{4.7}$$

If a nucleon is knocked out from a deeply bound state, and the excitation energy of a residual hole-state is above a particle separation threshold, the system will break into fragments.

Finally, in order to determine the excitation energy, we compute:

$$E^* = E_{rel} + S_n + E_\gamma \tag{4.8}$$

Experimentally, in order to reconstruct the initial and final state of the four-momentum vectors, making use of complete-kinematics measurements performed with the R^{3}B setup, we need the state of charge Q, the mass identification of the final state charged particles. Also, the velocities β_j and the relative scattering angles ϑ_{jk} are needed in order to determine the kinetic energy and the three-momentum of the initial and final state particles.

4.6.1 Velocity Correction

The velocity of the fragment, β_{fra}, and the neutron, β_n, as well as the relative angle between them are necessary for the reconstruction of the relative energy spectra. Therefore, these were calculated. The velocity distribution of the neutron has a tail towards lower energies, so it is fitted for energies up to 2.7 MeV where the acceptance of LAND begins to decrease (see Fig. 4.16).

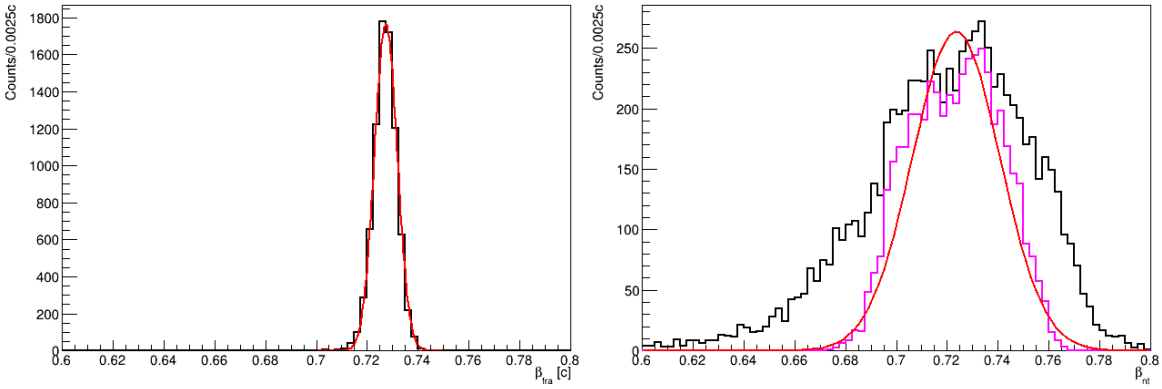

Figure 4.16: Left: Fragment velocity of ^{17}C . Right: Neutron velocity distribution shown in black. The pink line shows the velocity distribution of the neutrons below 2.7 MeV for which the velocity is fitted. Red line in both plots shows the Gaussian fit.

Fragments are bent by ALADIN and pass through the GFI detectors, which induce additional energy loss. Neutrons on the other hand, do not pass through any additional detectors after the SSDs after the target and go directly to LAND. Consequently, the velocity of the fragments was corrected to ensure that the mean velocities β_{fra} and β_n were the same after the neutron evaporation. In Figure 4.17 the relative energy plot is shown before and after the velocity of the fragment was corrected.

4.7 Crystal Ball simulations

The simulations for XBall were performed using R3BRoot [90], which is a simulation and analysis framework built for the R^{3}B setup.

R3BRoot is written in C++ and based on ROOT and Geant4 as particle transport engine.

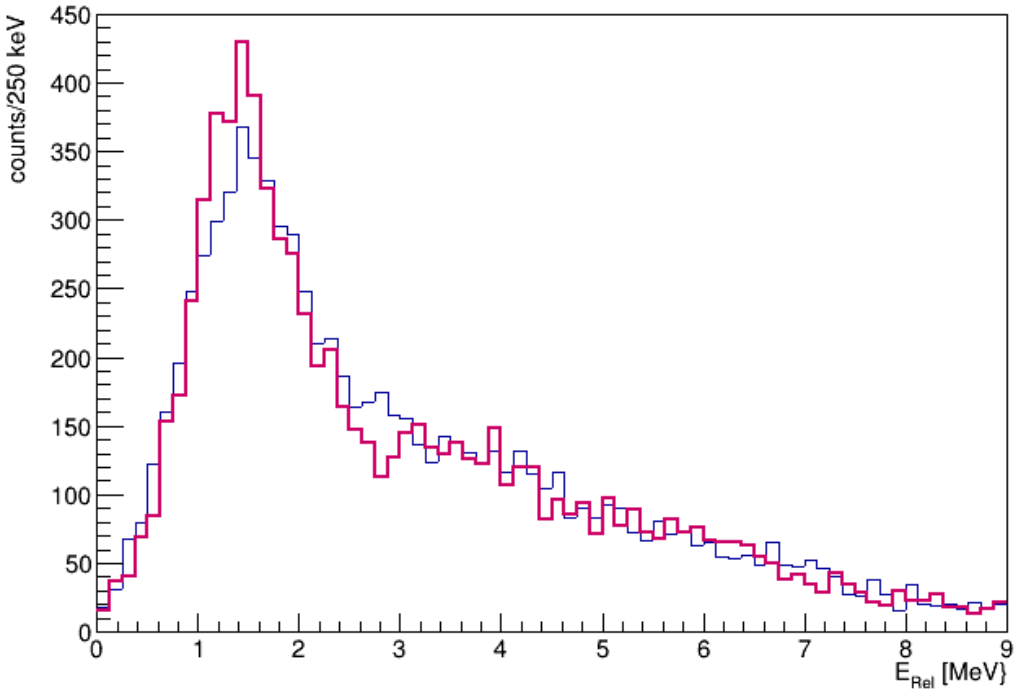

Figure 4.17: Comparison between the relative energy spectrum for ^{15}C + n before the velocity correction (blue line) and after the correction (red) for the CH_2 target .

It is object oriented and based on tasks, that allow the user to perform calibrations, data analysis, parameter generation and simulations. In this work only the simulation features of this framework were used.

4.7.1 Crystal Ball γ- Response

For the γ response, a code developed by I. Syndikus was used [85]. This code is an extension of the one developed by V. Panin [89], based on L. Chulkov's Fortran code for quasifree-scattering reaction simulations, which calculates the kinematics of the QFS process and simulates the internal momentum of the proton within the target. For this simulation the internal momentum follows a Gaussian distribution centered at 112 MeV/c. This software firstly generates the quasifree (p,2p) pair and secondly, a γ cascade part is added to the simulation coming from excited states (see Fig. 4.18).

These primary particles are ejected from a reaction point, that is randomised inside the target geometry (thickness and material) used during the experiment. For the calorimeter response, each crystal resolution was measured from calibration runs. This resolution is then added to the simulation and scaled accordingly, so each crystal has its own response to gammas in a realistic way. These gammas are then treated as experimental data, with the same addback routine.

For the efficiency calculations, the raw V. Panin quasifree code generates the knockout

pair, and then the addback routine for protons gives the number of events with two well-identified clusters. The efficiency of the detector for (p,2p) reactions is then :

$$\epsilon_{Xball} = \frac{N_{(p,2p)}}{N_{total}} \tag{4.9}$$

with $N_{(p,2p)}$ the number of events with two protons and N_{total} the total number of (p,2p) reactions generated.

First the resolution of each crystal has to be obtained. For this purpose, calibration data from a ^{60}Co source was used. The resolution is individually scaled as

$$R = R_{1MeV}/\sqrt{E} \tag{4.10}$$

The code for the resolution calculations was written by G. García-Jiménez [91]. The simulated γ rays of obtained are shown for ^{17}C in Fig. 4.18.

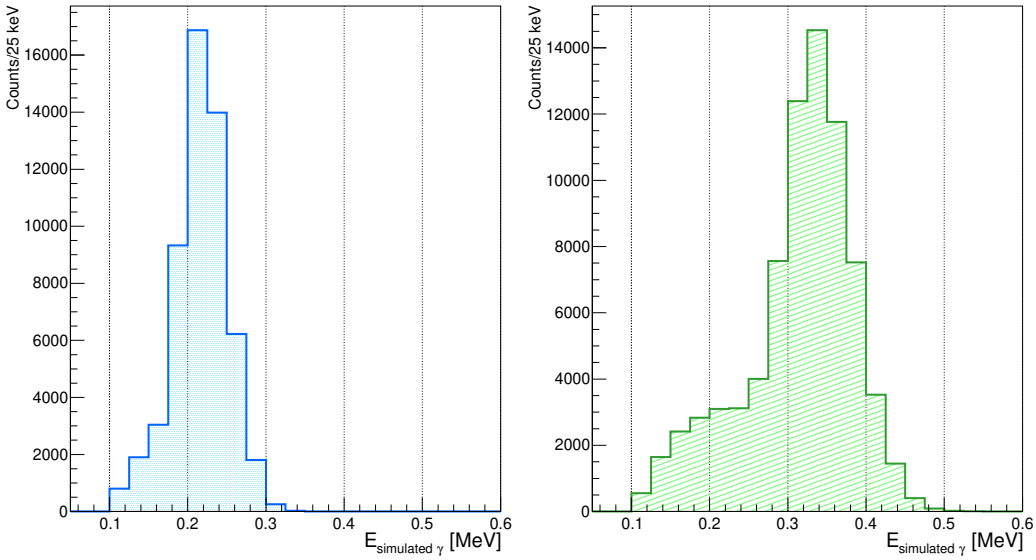

Figure 4.18: Simulated γ rays of the first (217 keV) (left) and second (335 keV) (right) excited states of ^{17}C. Compton scattering can be appreciated mainly in the 335- keV γ at around 0.2 MeV

4.7.2 Crystal Ball proton response

In order to calculate the exclusive cross sections, the efficiency of detecting two protons in Crystal Ball needs to be considered, For this purpose, simulations for QFS processes were performed for (p,2p) reactions as follows:

$$\epsilon_{2p} = \frac{N_{2p}}{N_{total}} \tag{4.11}$$

where N_{2p} represents the total of outgoing events with two protons and N_{total} the total number of events.

For this calculation, a total of 1×10^5 events were simulated. To make the simulation as realistic and comparable to the experimental results as possible, the same thresholds were used for the simulated protons and the protons from the experiment. Angular correlations performed with the simulated data are shown in Fig. 4.19.

The calculation of the two-proton events is performed by using the first-neighbour addback method (see Section 4.11) as described in Section 4.4.1, where the total energy of a single proton is taken by summing up the deposited energy in adjacent crystals above the thresholds shown in Table 4.4.

	$E_{threshold}[MeV]$	ϵ_{2p} [%]
^{17}N(p,2p)^{16}C* $\rightarrow^{15}$C+n	30	69.7(3)
^{19}N(p,2p)^{18}C* $\rightarrow^{17}$C+n	30	69.6(3)
^{21}N(p,2p)^{20}C* $\rightarrow^{19}$C+n	15	67.4(3)

Table 4.4: Efficiency to detect two protons in XBall obtained by simulations performed on R3BROOT along with the threshold energies used in both the S393 experimental data and the simulations.

It must be noted that the simulation employed to extract the two-proton efficiencies listed in this table does not include the SSDs and the target wheel. An estimation of the systematic error due to the use of different libraries and thresholds is not available yet.

4.8 Fit Procedures

4.8.1 Resonances: Breit-Wigner shape

In physics, resonant states are often described by a non relativistic Breit-Wigner distribution, named after G. Breit and E. Wigner for their nuclear resonance formula [92]. Therefore it seems appropriate for the description of the neutron unbound states discussed in this work:

$$BW(E; E_r, \Gamma) = \frac{\Gamma}{(E_r + \Delta - E)^2 + \Gamma^2/4} \tag{4.12}$$

where E_r is the energy of the resonance, Γ is the width of the resonance.

Resonant states follow this distribution, but a broadening effect due to the detector resolution must be taken into account, which usually takes the form of a Gaussian distribution:

$$G(E; E_r; \sigma) = \frac{1}{\sqrt{2\pi}\sigma} e^{-\frac{(E - E_r)^2}{2\sigma^2}} \tag{4.13}$$

where E_r is again the location of the resonance and σ is the resolution of our measurements, which in this case was extracted as function of energy from LAND neutron detector response matrices as indicated in Section 4.5.2.

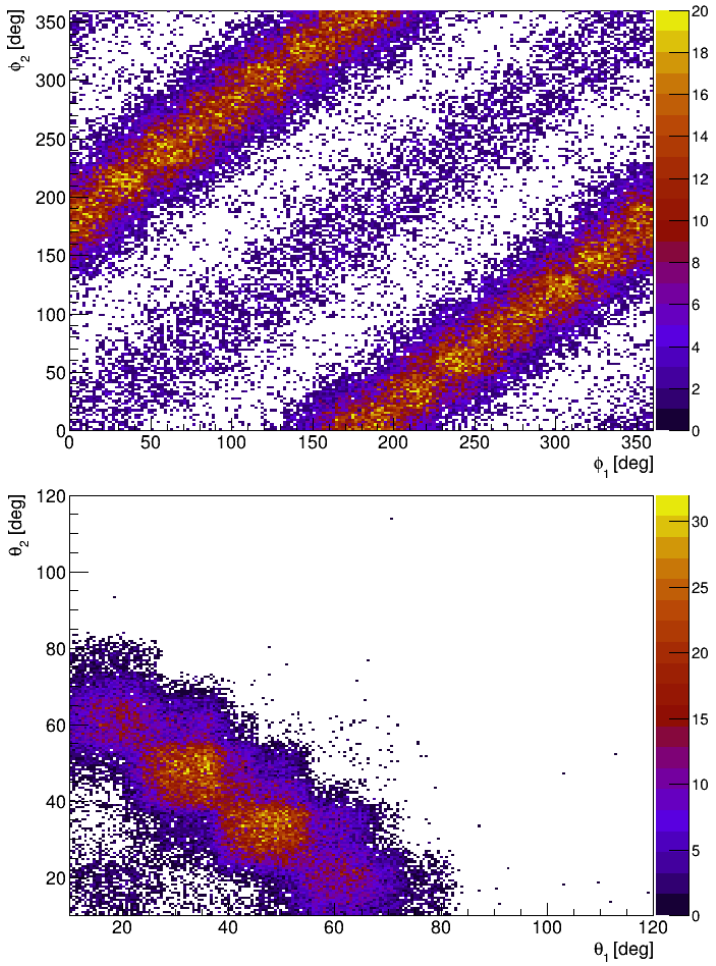

Figure 4.19: Crystal Ball response for the two protons generated with the Panin-Chulkov code. Angular correlations in the laboratory frame for the two simulated protons coming out from the $^{19}N(p,2p)^{18}C$ reaction are shown. The azimuthal distribution ϕ (top) shows the expected back-to-back scattering, while the polar angle correlation shows the expected peak at $\sim 80°$, signature of a quasifree knockout.

The distribution that results from the resolution broadening of the original Breit-Wigner shape of the resonance has the form of a convolution integral and is known as Voigt distribution:

$$V(E;E_r,\Gamma,\sigma) = BW * G = \int_{-\infty}^{\infty} BW(E';E_r,\Gamma)\, G(E';E_r;\sigma) = \\ = \int_{-\infty}^{\infty} \frac{\Gamma}{(E_r+\Delta-E')^2+\Gamma^2/4}\, \frac{1}{\sqrt{2\pi}\sigma} e^{-\frac{(E'-E_r)^2}{2\sigma^2}}\, dE' \tag{4.14}$$

The position E_r and width Γ of the resonance need to be extracted by fitting a Breit-Wigner distribution with an energy-dependent width using LEG.

4.8.2 Minimum χ^2 and Likelihood Methods

In order to calculate the number of reactions that populate the unbound states, we first need to find a test model that helps us describe quantitatively the experimental data. There are different approaches and some of them will be outlined in this section. The notation used is based on Baker and Cousins [93], which goes as follows:

n_i= the number of experimental events in the ith bin.

y_i= the number of events predicted by the model to be in the ith bin.

$N = \sum_{i=1}^{N} = n_i$ is th total number of events

Generally, a fitting procedure is comprised of a series of steps. the parameters that best describe the experimental data should be determined. Afterwards, the uncertainties of the results need to be calculated in order to estimate the confidence interval. And lastly, we need to test how well the prediction describes the data, this last step is called *goodness of fit* and it is usually probed by the use of χ^2. Although there are several method for the calculation of the χ^2, all agree in the minimisation of the χ^2, χ^2_{best}. A point at issue that might occur with this method is when the fit routine stops at a local minimum and does not find a global one. The goodness-of-fit is probed by calculating the reduced χ^2 defined by:

$$\chi^2_{reduced} = \frac{\chi^2_{gof}}{\text{NDF}} \tag{4.15}$$

where NDF is the degrees of freedom of the fit, namely difference between the number of bins to be fitted and the number of parameters in the fit. For this estimator, a value of $\chi^2_{reduced} \approx 1$ means it describes in a good approximation the experimental data. $\chi^2_{reduced} < 1$ might indicate there is an overestimation of the experimental uncertainties or too many parameters that might be fitting fluctuations and if it is $\chi^2_{reduced} \gg 1$ it means the model does not describe the experimental data correctly.

For the present analysis, several χ^2 estimators were calculated. The difference between one another lies mostly on how the errors are calculated:

Neyman's χ^2_N uses the uncertainty based on the sample data, where $\Delta n_i = \sqrt{n_i}$.

$$\chi^2 = \sum \frac{(n_i - y_i)^2}{n_i} = \sum \frac{(n_i - y_i)^2}{(\Delta n_i)^2} \tag{4.16}$$

Pearson's χ^2_P take the errors based on the parent distribution, *i.e.* the model prediction y_i.

$$\chi^2_P = \sum_{i=1}^{N} \frac{(n_i - y_i)^2}{y_i} \tag{4.17}$$

In both scenarios, the uncertainties are assumed as a Poisson distribution for a sample so large that it can be deemed as a normal distribution and thus, $(\Delta n_i)^2 = n_i$ and $(\Delta y_i)^2 = y_i$ prevail. Notwithstanding, it must be kept in mind that the relative energy spectra in the present analysis are reconstructed for the pure H target, which is a subtraction of the C target, and empty target histograms from that of CH_2. Therefore, it was found that the most accurate way to estimate the uncertainties is calculating them separately and then carry out a propagation of errors. Said that, n_i in Equation 4.16 is then the propagation of the errors from the CH_2, C and empty target relative energy spectra.

Alternatively to the χ^2 method, the *likelihood* methods are also useful to test how good a determined distribution describes a statistical sample. The starting point would be the Poisson probability (Eq. 4.8.2):

$$P_P(y,n) = \prod_{i=1}^{N} \left(\frac{(y_i)^{n_i}}{(n_i)!} \cdot e^{-yi} \right) \tag{4.18}$$

if we then compute its natural logarithm we obtain the value of the χ^2:

$$\ln P = \sum_{i=1}^{N} (n_i \cdot \ln(y_i) - y_i) + c \tag{4.19}$$

$$\chi^2 \simeq -2 \cdot \ln(P) \tag{4.20}$$

Chapter 5

Results

In this chapter the results of the analysis outlined in the previous section are presented and discussed. It will begin by explaining the procedure for reconstructing the relative-energy spectra of pure H_2 target and how the different sources of background are accounted for. Next subsection will explain the fitting procedure used to locate the resonances, putting emphasis on the discussion of the choice of fitting method and fitting parameters, and how the exclusive cross sections have been extracted from those fits. Finally, the resulting spectra for one neutron evaporation channels $^{16}C^{\star} \rightarrow ^{15}C+n$ and $^{18}C^{\star} \rightarrow ^{17}C+n$ will be presented and discussed in the light of the current knowledge and state of the art theoretical predictions.

5.1 Relative-energy spectra

The most suitable target for the study of (p,2p) QFS would be a pure proton target as it would remove background from other reactions channels. However, H_2 was not available for this experiment. Instead, two different targets were used separately for each beam setting in independent designated runs: a polyethylene target, CH_2, and a pure carbon target, C (see Table 5.1 for details).

Table 5.1: Incoming beam and target properties.

Beam	Energy	Thickness [g/cm^2]		Density ρ [g/cm^3]		Area density τ [cm^{-2}]	
	[MeV/A]	CH_2	C	CH_2	C	CH_2	C
^{17}N	438	0.458	0.558	0.92	1.84	1.97×10^{22}	2.80×10^{22}
^{19}N	430	0.923	0.935	0.94	1.84	3.97×10^{22}	4.69×10^{22}
^{21}N	422	0.923	0.935	0.94	1.84	3.97×10^{22}	4.69×10^{22}

The polyethylene target, CH_2, is chosen to study the (p,2p) quasi-free scattering reactions with the protons, H_2, inside the target. The pure carbon target, C, is used to reproduce the reactions coming from the carbon nuclei, also present in the CH_2 target, and account for this source of background by subtracting its contribution from the CH_2 relative-energy spectra.

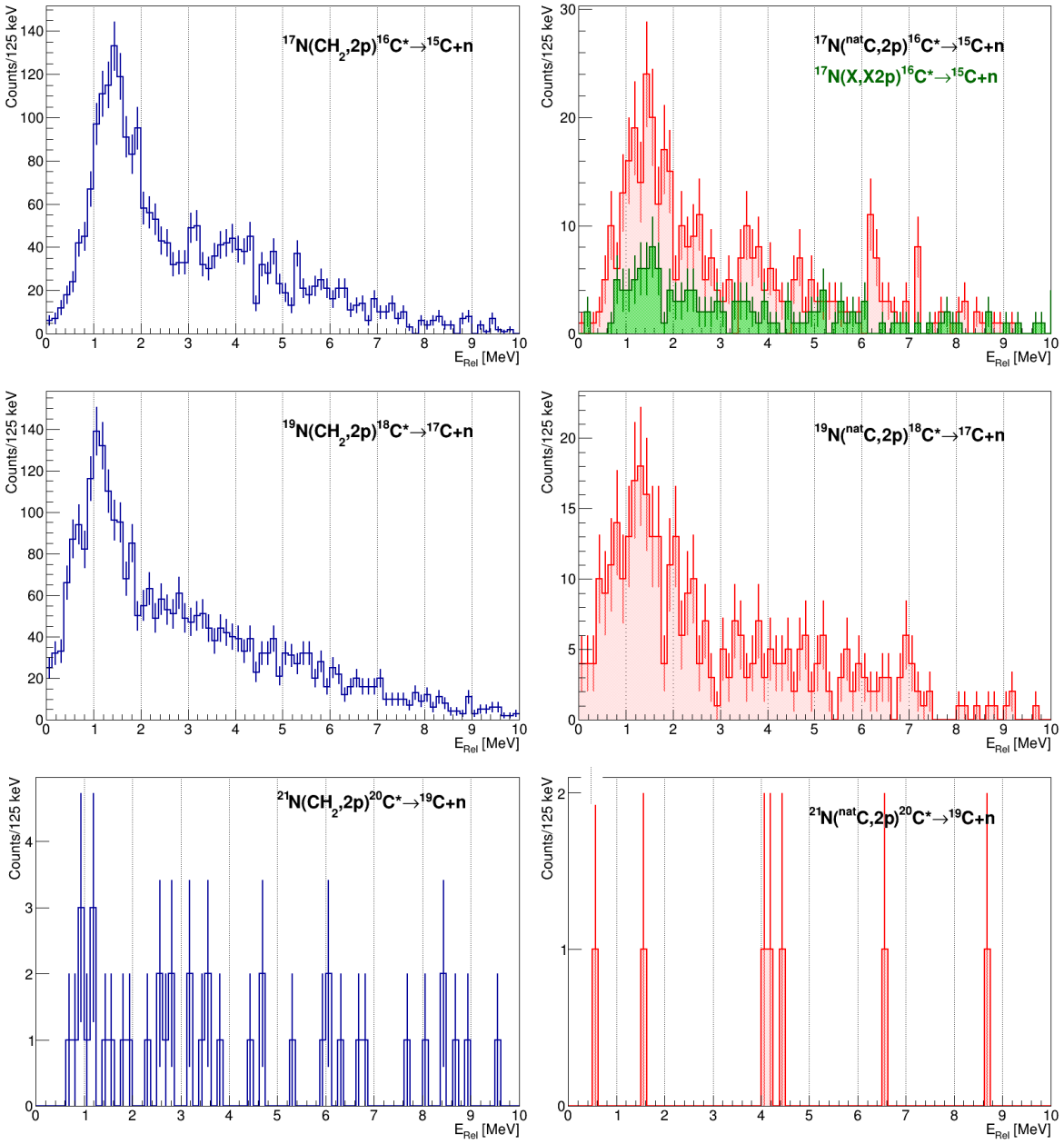

Figure 5.1: Relative-energy spectra recorded with CH_2 (blue), pure C (red) and no target (green) with ^{17}N (top), ^{19}N (middle) and ^{21}N (bottom) beams, requesting positive identification of the incoming beam of interest and the observation of ^{15}C, ^{17}C and ^{19}C respectively as outgoing fragments in coincidence with two protons in XBall and a neutron in LAND. Error bars are purely statistical.

Figure 5.1 presents the relative-energy spectra, with statistical error bars, for CH_2 and C targets measured with ^{17}N (top), ^{19}N (middle) and ^{21}N (bottom) beams for outgoing ^{15}C, ^{17}C and ^{19}C fragments in coincidence with two protons in XBall and one neutron in LAND. The empty-target relative-energy spectrum for ^{15}C+n recorded under the same conditions is also shown.

The aforementioned background subtraction is performed as follows:

$$N_{H_2} = N_{CH_2} - \frac{I_{CH_2}}{I_C} \cdot \frac{\tau_{CH_2}}{\tau_C} N_C \tag{5.1}$$

where N_{H_2}, N_{CH_2} and N_C are the number of events in the relative-energy spectra for the reconstructed H_2 target, CH_2 and C targets, respectively. Similarly, τ_{CH_2} and τ_C are target area densities of the CH_2 and C targets, whose values are listed in Table 5.1. I_{CH_2} and I_C are the number of incoming events in the corresponding run, estimated from the selected events in the corresponding particle identification plot corrected by the downscaling factors.

In addition, data were collected in the absence of target (MT target) in order to pinpoint the spurious reactions that take place in a detector in the beam line, so we can subtract its contribution from the data collected with the CH_2 and C targets:

$$N^{corr}_{CH_2} = N_{CH_2} - \frac{I_{CH_2}}{I_{MT}} N_{MT} \qquad N^{corr}_{C} = N_C - \frac{I_C}{I_{MT}} N_{MT} \tag{5.2}$$

where N_{MT} is the number of events in the relative-energy spectra for the empty target run and I_{MT} the number of incoming events in said run. Hence, replacing N_{CH_2} and N_C by $N^{corr}_{CH_2}$ and N^{corr}_{C} in Equation 5.2, N_{H_2} becomes

$$N_{H_2} = N_{CH_2} - \frac{I_{CH_2}}{I_C} \cdot \frac{\tau_{CH_2}}{\tau_C} N_C - \left(1 - \frac{\tau_{CH_2}}{\tau_C}\right) \frac{I_{CH_2}}{I_{MT}} N_{MT} \tag{5.3}$$

Unfortunately, there were no MT runs available with the ^{17}N beam, and the empty target run with ^{21}N was too short and the poor statistics rendered it unusable. Therefore, Equation 5.3 is only applied for the ^{15}N beam. Despite the lack of a useful empty target run for ^{17}N and ^{21}N, the thicknesses of the pure carbon targets were selected in such a way that the content of C was approximately the same as the content of C in the CH_2 target used with the same beam setting (Table 5.1). This means that the contribution of empty target run would be similar for both targets and cancel out; in Equation 5.3 the term $(1 - \tau_{CH_2}/\tau_C)$ would be close to zero.

Figure 5.2 shows the reconstructed H_2 relative-energy spectra obtained requesting PID of the beam of interest ^{17}N (top), ^{19}N (middle) and ^{21}N (bottom) and the detection of ^{15}C, ^{17}C and ^{19}C respectively, in coincidence with two protons in XBall and a neutron in LAND. Error bars arise from the propagation of the statistical uncertainties in the N_{CH_2}, N_C and N_{MT}.

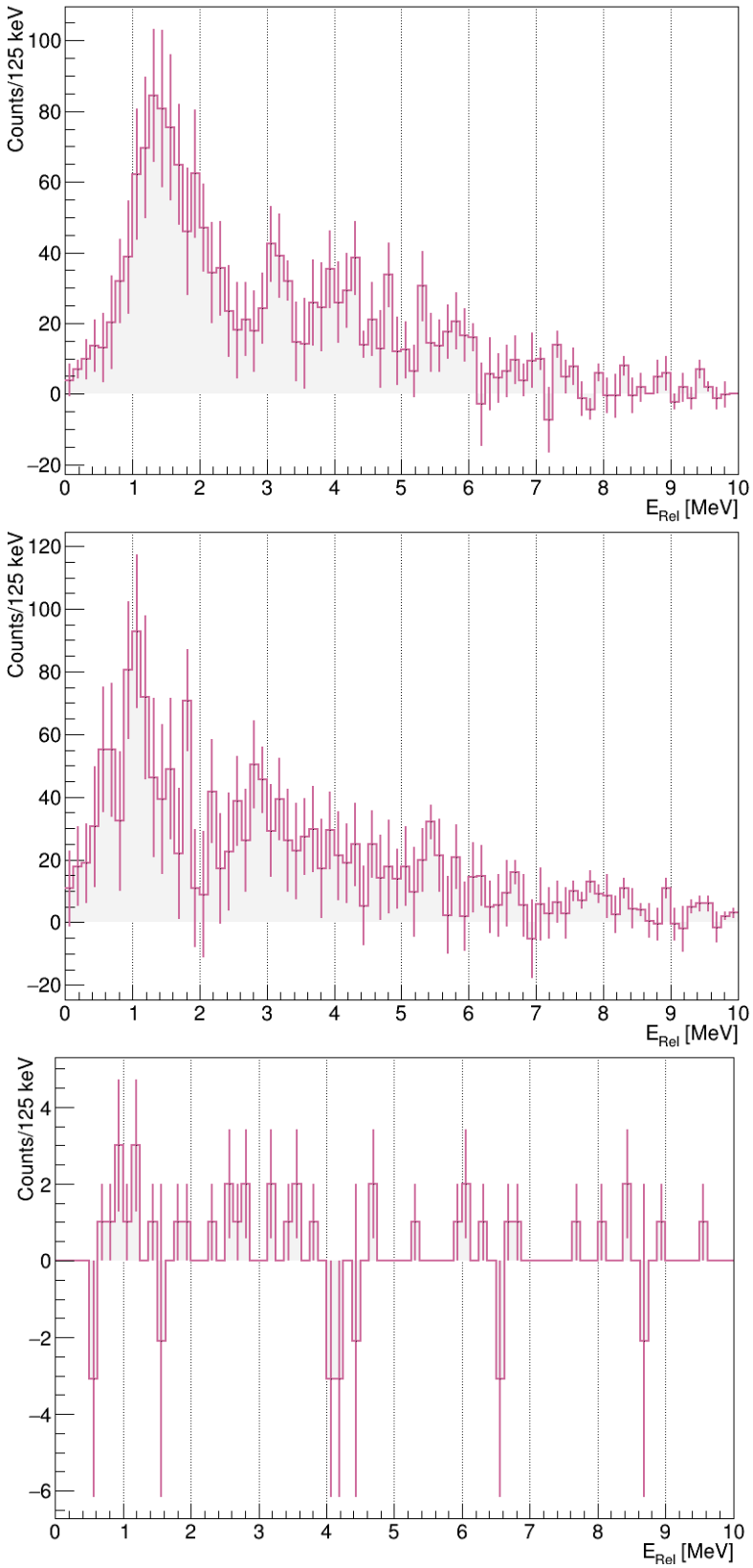

Figure 5.2: H_2 relative-energy spectra requesting positive identification of ^{17}N (top), ^{19}N (middle) or ^{21}N (bottom) as incoming particle and the observation of ^{15}C, ^{17}C and ^{19}C respectively as outgoing fragment in coincidence with two protons in XBall and a neutron in LAND. Error bars arise from the propagation of statistical uncertainties in the CH_2 and C spectra.

It should be noted that although Equations 5.3 and 5.2 are shown mainly to describe the reconstruction of the pure H_2 relative-energy spectra, a similar procedure can also be followed to subtract the background in the γ-energy spectra and reconstruct pure H_2 γ-energy spectra.

5.2 Analysis of the one-neutron evaporation channels

In order to locate the unbound states in even-mass neutron-rich carbon isotopes ^{16}C and ^{18}C, the relative-energy spectra obtained in previous section is scanned looking for resonances, previously described in Section 4.8.1. Results will be presented in the following sections. It is worth mentioning that these fit parameters were constrained to positive values in order to protect their physical meaning for further discussion.

In addition, the relative energy spectra were fitted with four different methods to evaluate the goodness of fit: Neyman's χ^2, Pearson χ^2, modified Neyman's χ^2 and likelihood (in the following denoted as χ^2_N, χ^2_P, χ^2_N*, and χ^2_L respectively), in order to verify that the results are not affected by the fitting method. Details on this procedure can be found in Appendix B.

5.2.1 Exclusive cross sections

Once the unbound states have been located, the exclusive cross section to populate a certain resonant state can be calculated with the following equation:

$$\sigma_{excl,target} = \frac{1}{2} \cdot \frac{1}{\tau} \cdot \frac{1}{\epsilon_{2p}\epsilon_n} \cdot \frac{N_{resonance}}{I_{target}} \tag{5.4}$$

where, following the same nomenclature from the previous section, τ is the target density (see Table 5.1) and I_{target} is the number of incoming events for the indicated target. $N_{resonance}$ is the number of events populating the resonant state of interest, which is extracted from the integral of the Voigt function corresponding to such resonance. Finally, ϵ_n and ϵ_{2p} are the efficiencies to detect one neutron in LAND and two protons in XBall respectively. They are both obtained from simulations (for further details see Sections 4.5.2 and 4.7.2, respectively), and shown in Table 4.4.

Since the reconstructed relative-energy spectra in this analysis are done for H_2, as seen in Equations 5.3 and 5.2, a correction by a factor of 2 is needed in Equation 5.4 to obtain the cross sections for H.

5.3 $^{16}C^{\star} \rightarrow ^{15}C+n$

The reconstructed pure H_2 target relative-energy spectrum for the ^{17}N beam, obtained requesting the observation of a ^{15}C fragment in coincidence with two protons and one neutron (see Figure 5.2 top) was fitted to two, three and four resonances.

The similarity of the results obtained for the different approaches, regardless of the number of resonances, allows us to conclude that the results are not influenced by the choice of fitting method (see Appendix B). Therefore, in the present chapter only results obtained with χ^2_N* method will be presented.

Amongst the different minimum likelihood methods, the modified Neyman's chi square method, χ^2_{N*}, is presented. It is the conventional Neyman chi square method (see Section 4.8.2 and Appendix B), but taking the errors as the propagation of the statistical errors of the CH_2 and pure C target (see top panels of Fig. 5.1). The outcome of these fits is presented in Figure 5.3, while the corresponding fit parameters and the associated χ^2_{N*} values are shown in Table 5.2.

The results show that the fits with 2 and 3 resonances produce very similar values of the χ^2_{N*}, while the goodness of the fit worsens with 4 resonances and, in addition, the second and third resonances would need to have their width set to the minimum (0.01 MeV), which is not in line with the physics of the unbound states.

Conspicuously for all fits, regardless of the number of resonances, the position of the first resonance at 1.46(6) MeV is in excellent agreement for the two- and three-resonance fits. Similarly, the position of the second resonance, at 3.88(26) and 3.57(41) for the two- and three-resonance fits respectively, is also in good agreement within one standard deviation. In addition, it is clear that the fits with three and four resonances agree rather well with a resonance around 5.5 MeV. Concerning the widths, we have a similar scenario: excellent agreement for the first resonance with a width of 0.6 MeV, whilst the widths deduced for the second resonance remains within 1.4 standard deviations for fits with two and three resonances and, again, fits with three and four resonances agree within one sigma with a width around 1.5 MeV for the resonance proposed at 5.5 MeV.

In light of these results, the fit with 3 resonances was chosen for further analysis and discussion, due to the low χ^2_{N*} value and the good agreement found for the first two resonances with the two-resonance fit. Therefore, in the following, 3 resonances will be considered: located at $E_{rel,1}$ =1.46(6) MeV, $E_{rel,2}$ =3.57(41) MeV and $E_{rel,3}$ =5.53(88) MeV, with the corresponding widths being Γ_1 =0.63(17) MeV, Γ_2 =1.94(113) MeV and Γ_3 =1.33(246) MeV, respectively.

Table 5.2: Energy E_{Rel} and width Γ measurements obtained by the Neyman's χ^2_{N*} method fitted to different number of resonances for the pure H_2 relative-energy spectra of $^{15}C+n$

Fit	Resonance 1		Resonance 2		Resonance 3		Resonance 4		$\frac{\chi^2}{NDF}$
	E [MeV]	Γ[MeV]	E [MeV]	Γ[MeV]	E [MeV]	Γ [MeV]	E [MeV]	Γ [MeV]	
Two Resonances	1.46(6)	0.58(15)	3.88(26)	2.88(54)					0.711
Three Resonances	1.46(6)	0.63(17)	3.57(41)	1.94(113)	5.53(88)	1.33(246)			0.714
Four Resonances	1.49(40)	0.74(13)	3.07(13)	0.01(68)	4.07(18)	0.01(73)	5.42(44)	1.70(15)	0.735

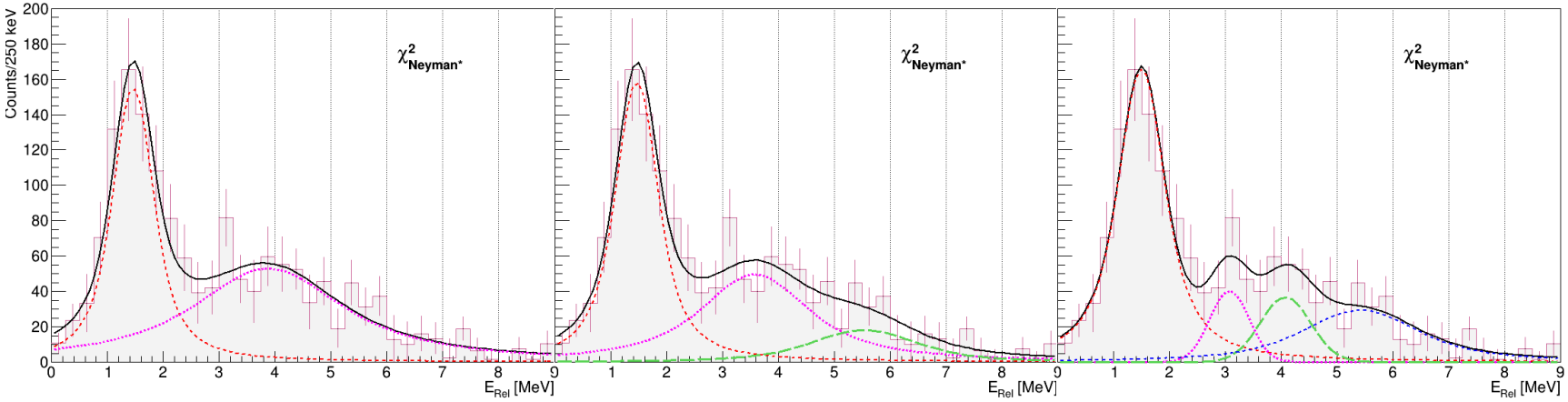

Figure 5.3: H_2 relative-energy spectra requesting identification of ^{17}N as incoming particle and the observation of ^{15}C as outgoing fragment in coincidence with two protons in XBall and a neutron in LAND (same as Figure 5.2 top), fitted to two (left), three (centre) and four (right) resonances described by Breit-Wigner convoluted with a Gaussian. Results of these fits are presented in table 5.2.

5.3.1 γ-gated relative-energy spectrum

In some cases, it can happen that the unbound states of the decaying systems do not undergo a direct decay to the ground state but to an excited state of the resulting fragment. It is therefore required to extract the excitation energies of the observed resonances to assess which of them decay to the ground state and which, if any, populate an excited state in ^{15}C. Any subsequent γ ray needs to be accounted for to accurately convert the position of the resonances in the relative-energy spectrum into excitation energy, as indicated in Equation 4.8 in Section 4.6.

The prompt γ-ray spectrum observed in coincidence with a ^{15}C fragment, two protons in XBall and one neutron in LAND is presented in Figure 5.4, where no clear peak is observed at 740 keV from the first excited state in ^{15}C. This may suggest that no unbound state in ^{16}C decays to the $5/2^+$ state in ^{15}C, yet other reasons that can explain the absence of the 740 keV γ-ray should be considered.

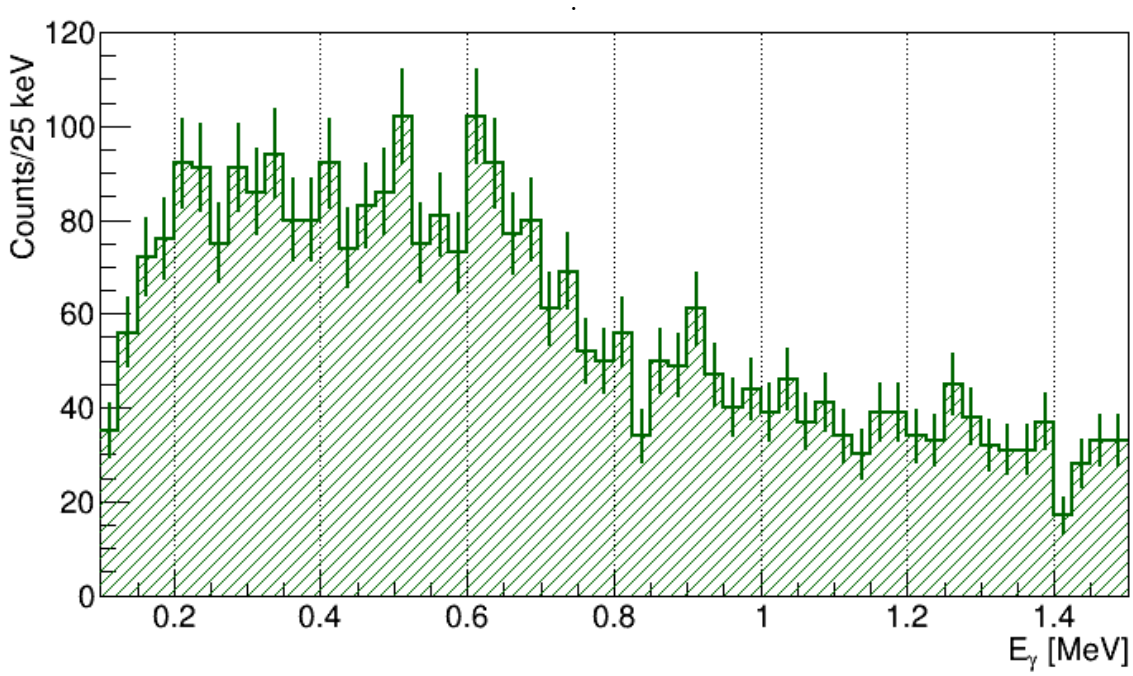

Figure 5.4: Prompt γ-ray spectrum of ^{15}C in coincidence with one neutron and two protons for the CH_2 target. No clear structure is observed at 740 keV from the first excited state in ^{15}C.

The absence of a peak at 740 keV can be understood once we consider the half-life of the first excited state, $T_{1/2}$=2.61 ns. Using the exponential decay formula and the Lorentz boosted half-life, the γ-ray emission time distribution was simulated. Using the average recoil velocity β=0.731c, the associated γ-ray position emission distribution was estimated (see Figure 5.5), whereby the γ rays are emitted far outside the centre of the target as it was assumed when extracting the scattering angle θ, with a large fraction emitted outside XBall and escaping detection altogether.

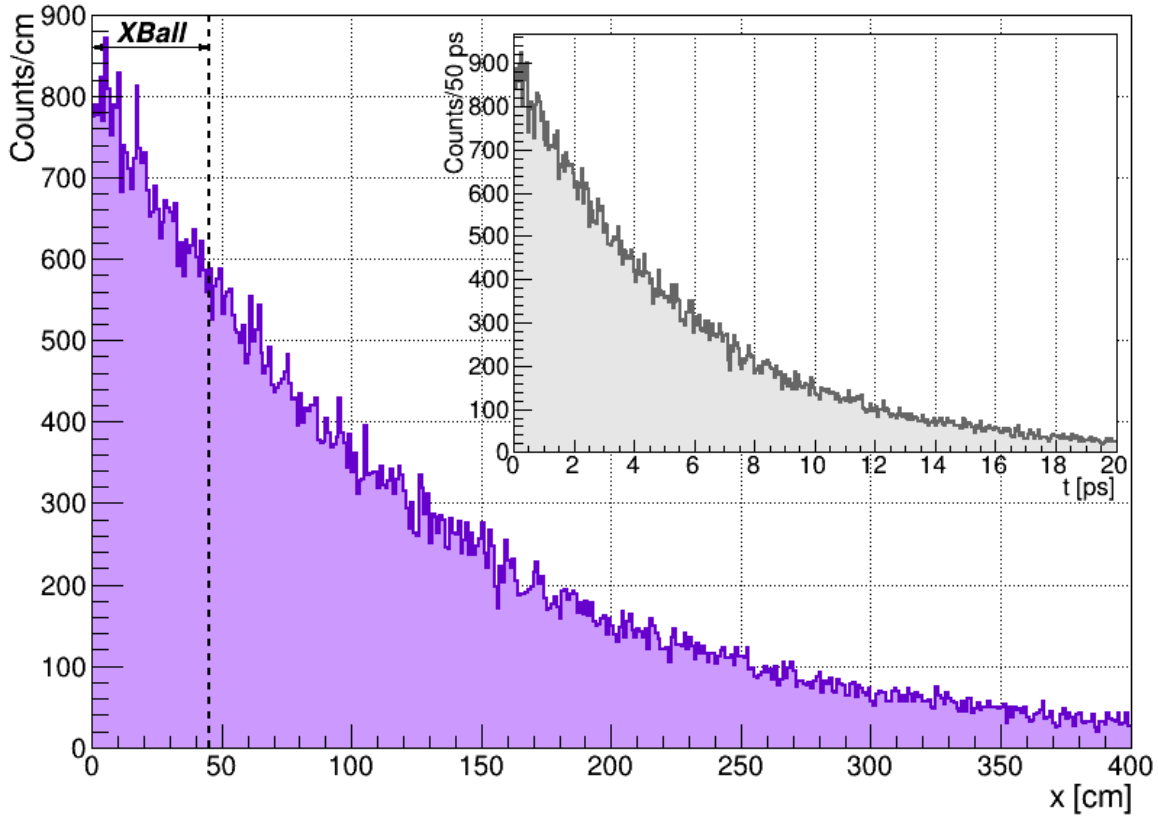

Figure 5.5: Distribution of the position of emission of the 740 keV γ ray coming from the first excited state in ^{15}C, extracted from the simulated time distribution (inset) with hal-life of $T_{1/2}$=2.61 ns and taking β=0.731c as the recoil velocity. The radius of XBall (45 cm) is also shown to highlight the setup limitations to observe long-lived γ-ray transitions.

This large shift in the position of emission of the 740 keV γ ray due to the lifetime results is an important reduction of the γ-ray efficiency. For those γ-rays that can be detected, there is a large underestimation of the scattering angle θ and therefore a wrong Doppler correction, shifting significantly the Doppler reconstructed energy towards lower energies.

In order to disentangle these lifetime effects, a simulation of the detector response to a realistic emission of the 740 keV γ ray was carried out. The lifetime effects were implemented by changing the γ-ray emission position with respect to the target in the Z-axis to follow a distribution governed by the exponential decay law (see Fig. 5.5). The simulation results are presented in Figure 5.6, where we can observe a low-lying structure around 0.15 MeV followed by a plateau that drops at 0.65 MeV. When comparing the simulated spectrum with the experimental prompt γ-ray spectrum of ^{15}C in coincidence with one neutron (see Figure 5.4), we also notice the plateau in the experimental data but the low-energy structure is not clearly seen, although the experimental data present a significant background that may hinder its observation.

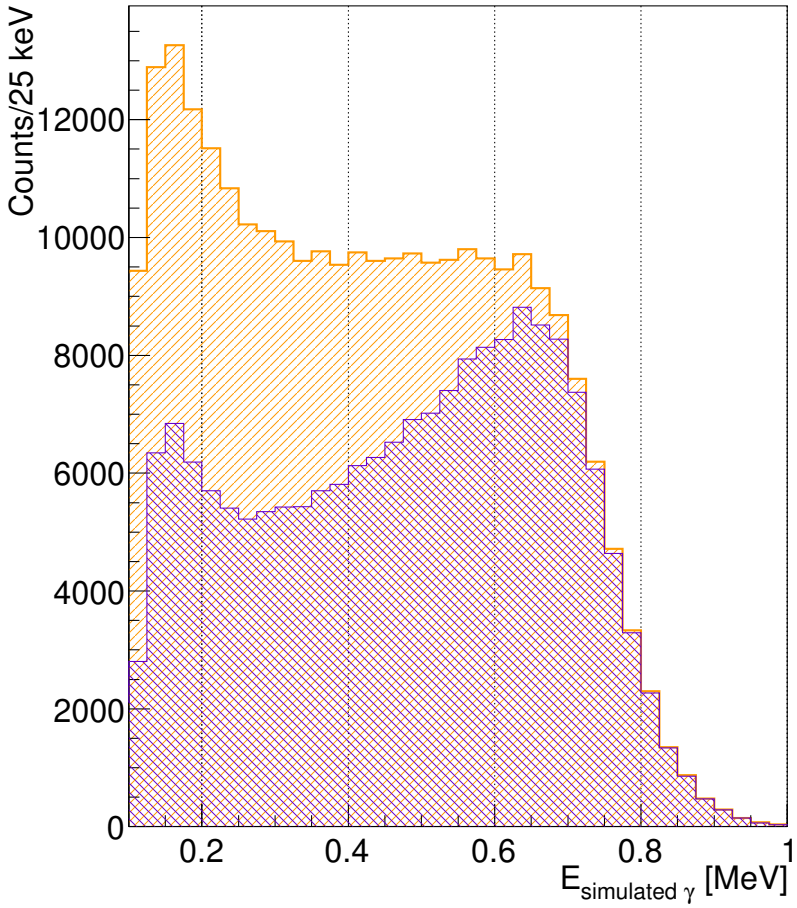

Figure 5.6: Simulation of the first $5/2^+$ excited state (740 keV) of ^{15}C, presented for the full spectrum (orange) and multiplicity $M_\gamma = 1$ (violet).

The nature of the low-energy peak is investigated to assess whether it is due to lifetime effects. The simulation spectra was inspected using several conditions on the distance of the emission point from the target position (see Fig. 5.7). When imposing the emission at short distances (< 10 cm) from the centre of the target, a well defined structure at 740 keV was observed and the peak at low energies disappeared almost completely. On the contrary, when the γ emission point was restricted to the outside of XBall (> 45 cm), only the structure at low energies was observed. This indicates that this low-energy structure is due to lifetime effects. In these cases where the γ ray is emitted at larger distances, the Lorentz-boost will concentrate the hits in the forward cap of XBall ($\theta < 20°$), leading to an underestimation of the scattering angle θ and therefore to a Doppler correction between two and four times smaller than it should be. 98% of the total number of events (10^6) come from within XBall, therefore this structure should be present in the experimental data if there was population of the $5/2^+$ in ^{15}C.

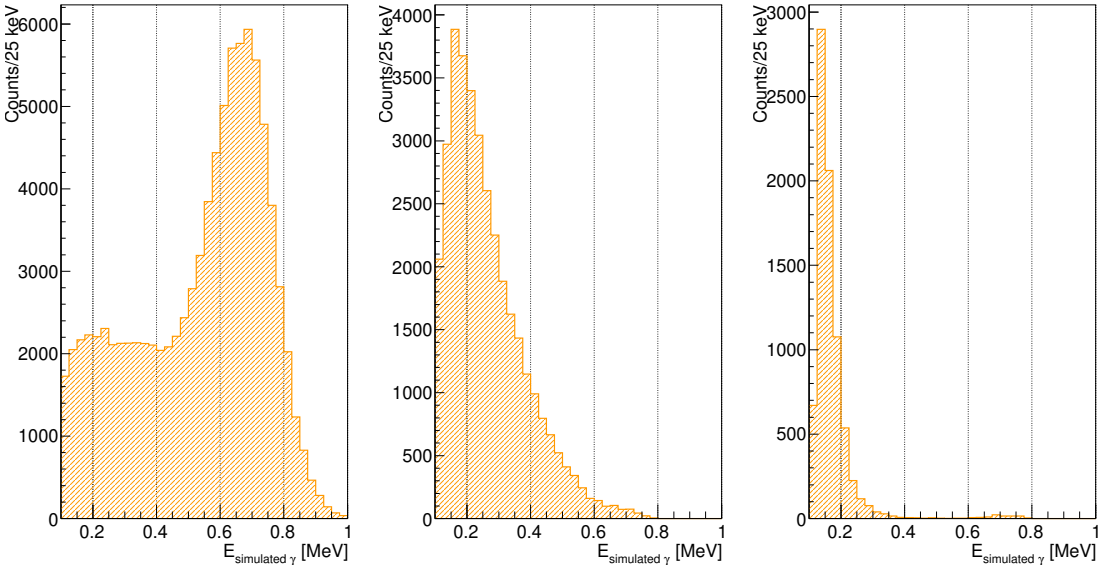

Figure 5.7: Simulated γ energy of the first $5/2^{+}$ excited state (740 keV) of ^{15}C conditioned on the γ emission point: inside XBall and close to the target (< 10 cm)(left); between 30 cm and 45 cm inside XBall (centre); and outside XBall (> 45 cm)(right).

In order to supress the background in the experimental data, the prompt γ-ray spectrum of ^{15}C in coincidence with one neutron was studied for multiplicity $M_{\gamma} = 1$ (see Figure 5.8) and was compared with the simulated spectrum with the same constraint. This comparison reveals similar features in both experimental and simulated spectra. The structure at lower energies and the γ transition at 740 keV were observed in both cases. Additionally, direct population of the first excited state of ^{15}C was investigated in order to compare the simulation with a larger sample of the experimental data. The resulting spectra (see Figure 5.9) is consistent with the γ-ray spectra in coincidence with unbound states in ^{16}C, and compares well with the simulation results. This seems to suggest that a fraction of the unbound states in ^{16}C decays through the first excited state in ^{15}C.

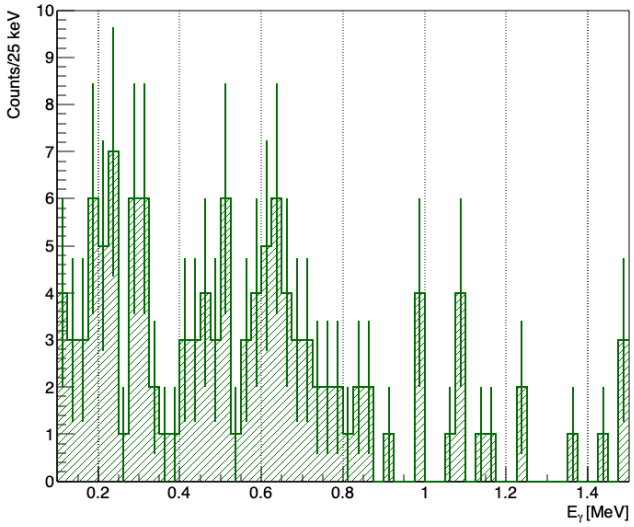

Figure 5.8: Prompt γ spectrum of ^{15}C in coincidence with one neutron and two protons for the CH_2 target constrained to multiplicity $M_{\gamma} = 1$.

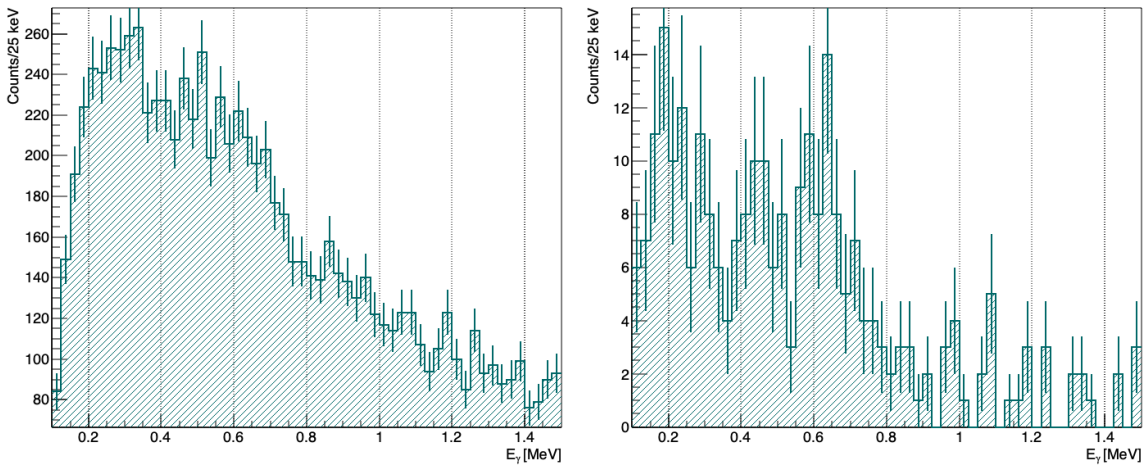

Figure 5.9: Prompt γ-ray spectrum of the direct population of the bound states of ^{15}C in coincidence with two protons for the CH_2 target presented for the full statistics (left) and for multiplicity $M_\gamma = 1$.

The simulation of the first $5/2^+$ excited state in ^{15}C suggests the presence of 740 keV γ rays in coincidence with unbound states in ^{16}C. However, despite the simulation efforts, due to setup limitations it remains extremely challenging to accurately estimate the yield that decays through the first excited state in ^{15}C. The branching ratios from the individual unbound states were not measured, instead the combined branching ratio for all three unbound states observed in this work was estimated to be 15(9)%.

In the following, the discussion will assume all resonances decay directly to the ground state of ^{15}C because of the lack of evidence to pinpoint which unbound(s) state(s) feed the first excited state in ^{15}C.

Finally, the excitation energy of the resonances located at 1.46(6), 3.57(40) and 5.53(88) MeV in the relative-energy spectrum is obtained with respect to the ground state of ^{16}C, resulting 5.71(6), 7.83(41) and 9.78(88) MeV respectively (see Figure 5.10).

It is worth mentioning that these excitation energies indicate that the decay to ^{14}C via two neutron emission is open for all three resonances reported here, since they are all located above the 2 neutron separation energy, as can be seen in Figure 5.10.

5.3.2 Exclusive cross sections

Experimental exclusive cross sections are extracted as indicated in Subsection 5.2.1 for the population of the unbound states observed in this work and presented in Table 5.3, together with their widths and neutron detection efficiency. Uncertainties presented are propagated from errors in target thickness, incoming number of events and proton and neutron efficiencies, but are largely dominated by the yield estimation of each resonant state arising from the statistical uncertainty in fit results.

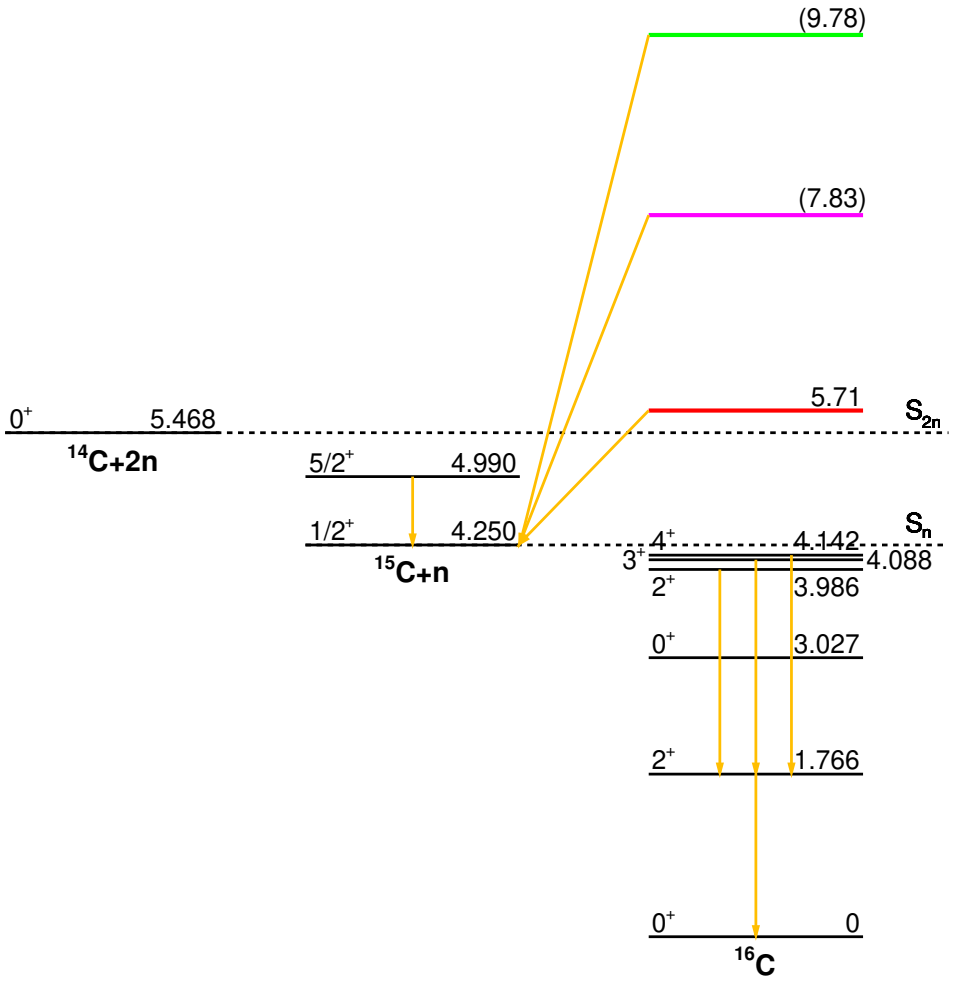

Figure 5.10: Level scheme of ^{16}C, including the unbound states observed in this work at 5.71(6), 7.83(41) and 9.78(88) MeV. Unbound states reported here lie above the one- and two-neutron separation energies represented by dashed lines. It is worth noting that the excitation energies have been extracted assuming direct decay to ^{15}C ground state.

E* [MeV]	E_{Rel} [MeV]	Γ [MeV]	ϵ_n [%]	σ_{exc} [mb]
5.71(6)	1.46(6)	0.63(16)	83.38(4)	1.44(27)
7.83(41)	3.57(41)	1.94(113)	$63.1^{+8.9}_{-8.1}$	1.59(103)
9.78(88)	5.53(88)	1.33(265)	$34.3^{+10.0}_{-6.4}$	0.95(95)

Table 5.3: $^{15}C+n$ cross sections for the population of the unbound states following the $(p, 2p)$ reaction. E represents the excitation energy obtained by summing E_{Rel} to the separation energy of one neutron of ^{16}C, S_n=4250(4) keV.*

It is important to mention that these exclusive cross sections account only for the contribution of the one neutron decay channel. However, we have seen already that the unbound states reported here are all located above the 2 neutron separation threshold, and therefore they are also expected to decay to ^{14}C via 2 neutron emission. Hence, analysis of the 2

neutron evaporation channel is required for an accurate estimation of the exclusive cross sections (work ongoing).

5.4 ^{18}C* $\rightarrow^{17}$C+n

The relative-energy spectrum of ^{17}C+n for the reconstructed pure H_2 target, attained by the selection of the ^{19}N as incoming beam particle and ^{17}C as outgoing fragment in coincidence with two protons in XBall and one neutron in LAND (see Figure 5.2 middle panel), was fitted from two to five resonances in the same way described in the previous section for the ^{15}C+n channel.

In view of the similarity between the outcomes obtained in the fitting tests performed for ^{15}C+n for different goodness-of-fit approaches, when changing from one method to another, in the present section only the outcomes from Neyman's modified χ^2_N* fits are presented. Notwithstanding, the other methods previously described in Section 4.8.2 were also tested, the results are shown in Appendix B.

The energy E and width Γ values obtained with fits using the χ^2_N* are shown in Table 5.5. Figure 5.11 shows the corresponding fits for three, four and five resonances, which hold similar χ^2/NDF values. The first resonance in all the cases matches excellently energy wise. The second resonance for two, three and four resonances agree well within one standard deviation, while for the five-resonance fit, the energy varies within two standard deviations. Apropos for the third resonance in the three- and four-resonance fits its energy changes significantly. So, if we now examine the widths in the three cases with the lowest χ^2/NDF value, the first resonant state is evidently consistent agreeing within one standard deviation. Although the second resonance in the three- and five-resonance fits seems to agree, these values are rather at the minimum limit. In addition, we observe that for the fits with two and three resonances the highest-energy resonance is significantly broad, which has been deemed as an indication of the need for more resonances in order to model the data more accurately. In the case where a fifth resonance was added, the χ^2/NDF value increased, which was the indication that the four-resonance fit, was indeed the best fit.

5.4.1 γ-gated relative-energy spectrum

As it was done for the ^{15}C+n channel, the prompt γ-ray spectrum in coincidence with one neutron decay from ^{18}C, ^{18}C* $\rightarrow^{17}$C+n, shown in Figure 5.12 left and obtained by requesting γ-ray emission within 40 ns of a ^{17}C fragment in coincidence, two protons in XBall and one neutron in LAND, is analysed to assess whether the resonances previously discussed decay to one of the low-lying excited states in ^{17}C instead of directly to its ground state.

Table 5.4: Energy E_{Rel} and width Γ measurements obtained by the Neyman's χ^2_{N*} fit method with two, three, four and five resonances for the pure H_2 relative-energy spectrum of $^{17}C+n$

Fit	Resonance 1		Resonance 2		Resonance 3		Resonance 4		Resonance 5		$\frac{\chi^2}{NDF}$
	E [MeV]	Γ[MeV]	E [MeV]	Γ[MeV]	E [MeV]	Γ [MeV]	E [MeV]	Γ [MeV]	E [MeV]	Γ [MeV]	
2 Resonances	1.02(9)	0.37(31)	2.64(59)	5.55(91)							0.655
3 Resonances	1.05(10)	0.71(35)	2.90(15)	0.01(117)	3.76(133)	6.02(17)					0.581
4 Resonances	1.03(10)	0.81(29)	3.00(20)	1.37(54)	5.31(33)	0.33(178)	7.80(30)	0.01(166)			0.537
5 Resonances	0.98(10)	0.71(25)	1.81(20)	0.01(134)	3.00(18)	0.83(140)	5.18(57)	0.83(135)	7.82(30)	0.01(161)	0.573

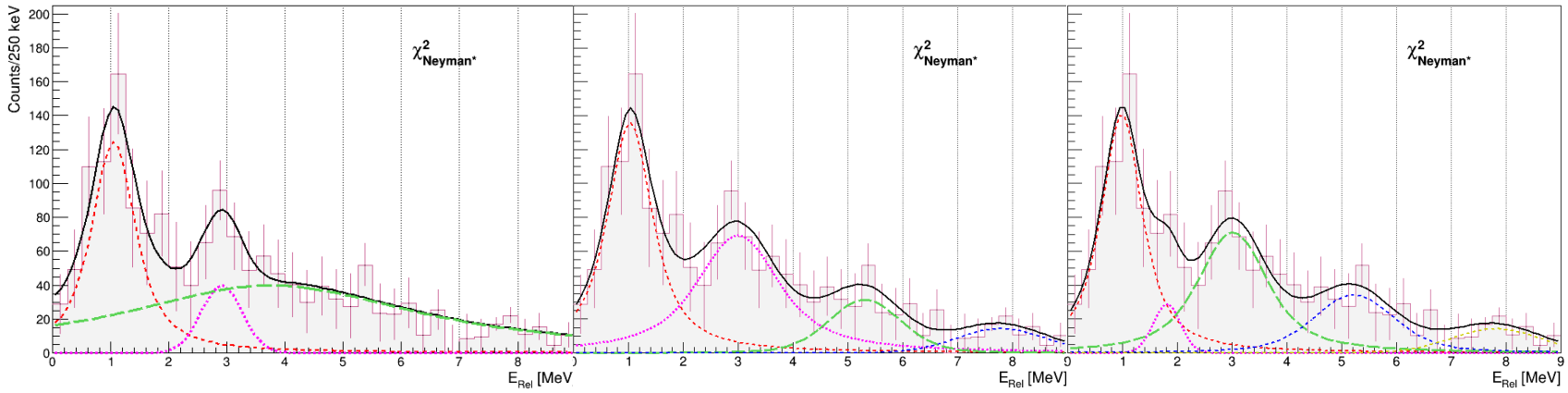

Figure 5.11: H_2 relative-energy spectra requesting positive identification of ^{19}N as incoming particle and the observation of ^{17}C as outgoing fragment in coincidence with two protons in XBall and a neutron in LAND (same as Figure 5.2 centre), fitted to three (left), four (centre) and five (right) resonances described by Breit-Wigner convoluted with a Gaussian. Results of these fits are presented in Table 5.5.

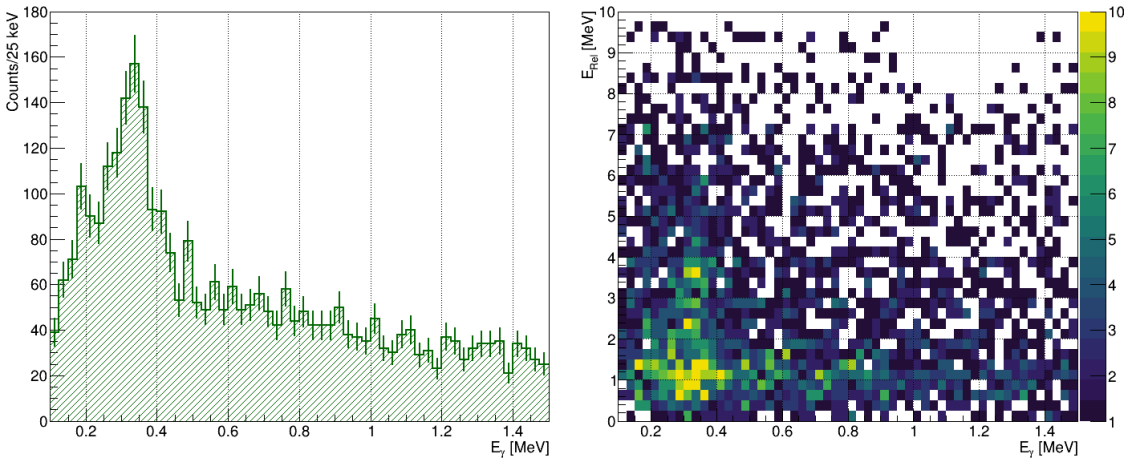

Figure 5.12: Prompt γ-ray energy spectrum (left) of ^{17}C in coincidence with one neutron and two QFS protons for CH_2, and prompt γ-ray spectrum versus relative energy (right) under the same conditions (note it is the same subset of events as Figures 5.2 centre and 5.11). Accumulation of events around 335 keV suggest some resonant states decay to the 2^{nd} excited state in ^{17}C instead of its ground state.

The presence of a clear peak at 335 keV, corresponding to the γ ray from the second excited state in ^{17}C to its ground state, provides convincing evidence that some of the observed resonances decay to the $5/2^+$ state in ^{17}C. In addition, the shoulder at lower energies may be an indication of the 217 keV transition from the $1/2^+$ first excited state to the ground state.

Complementary to this, the 2D plot in Figure 5.12 shows the correlation between γ rays shown in left panel of Fig. 5.12 and the relative energy for the ^{17}C+n events (same conditions) for the CH_2 target. The yellow and light green accumulations observed around E_{Rel}=1, 2.4 and 3.7 MeV (Y-axis) for E_γ=0.335 MeV (X-axis) supports the claim that some of the unbound states in ^{18}C do not decay directly to ^{17}C ground state, but through its second excited state (see level scheme shown in 2.15).

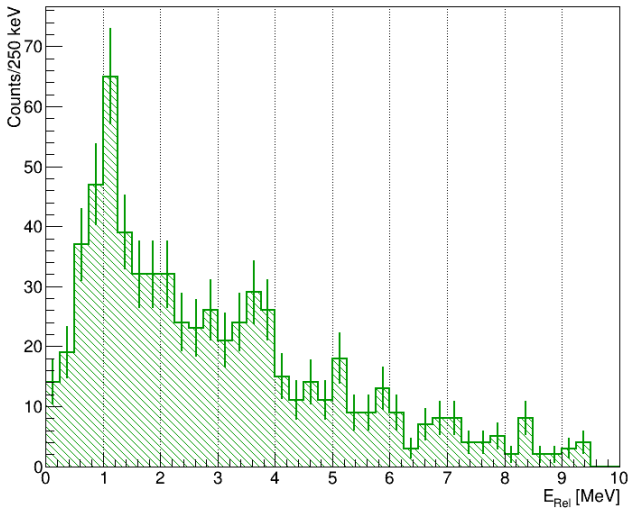

Figure 5.13: Gamma-gated relative-energy spectrum for $^{17}C+n$, demanding ^{19}N as incoming particle and the observation of an outgoing ^{17}C in coincidence with two protons in XBall and a neutron in LAND.

In light of this evidence, we looked at the distribution of events in the relative-energy spectrum when, in addition to the conditions calling two protons in XBall and one neutron in LAND in coincidence with a ^{17}C fragment. It is also requested γ-emission within a 40 ns window from the trigger of a 335 keV γ ray (between 250 and 425 keV). The resulting spectrum, that hereafter will be called as the *γ-gated relative-energy spectrum* is shown in Fig. 5.13.

We can see in the left panel of Figure 5.12 that the γ-ray peak at 335 keV we are gating on is sitting on top of a significant background and hence, the γ-gated relative-energy spectrum shown in Figure 5.13 contains a significant contribution from random γ correlated events.

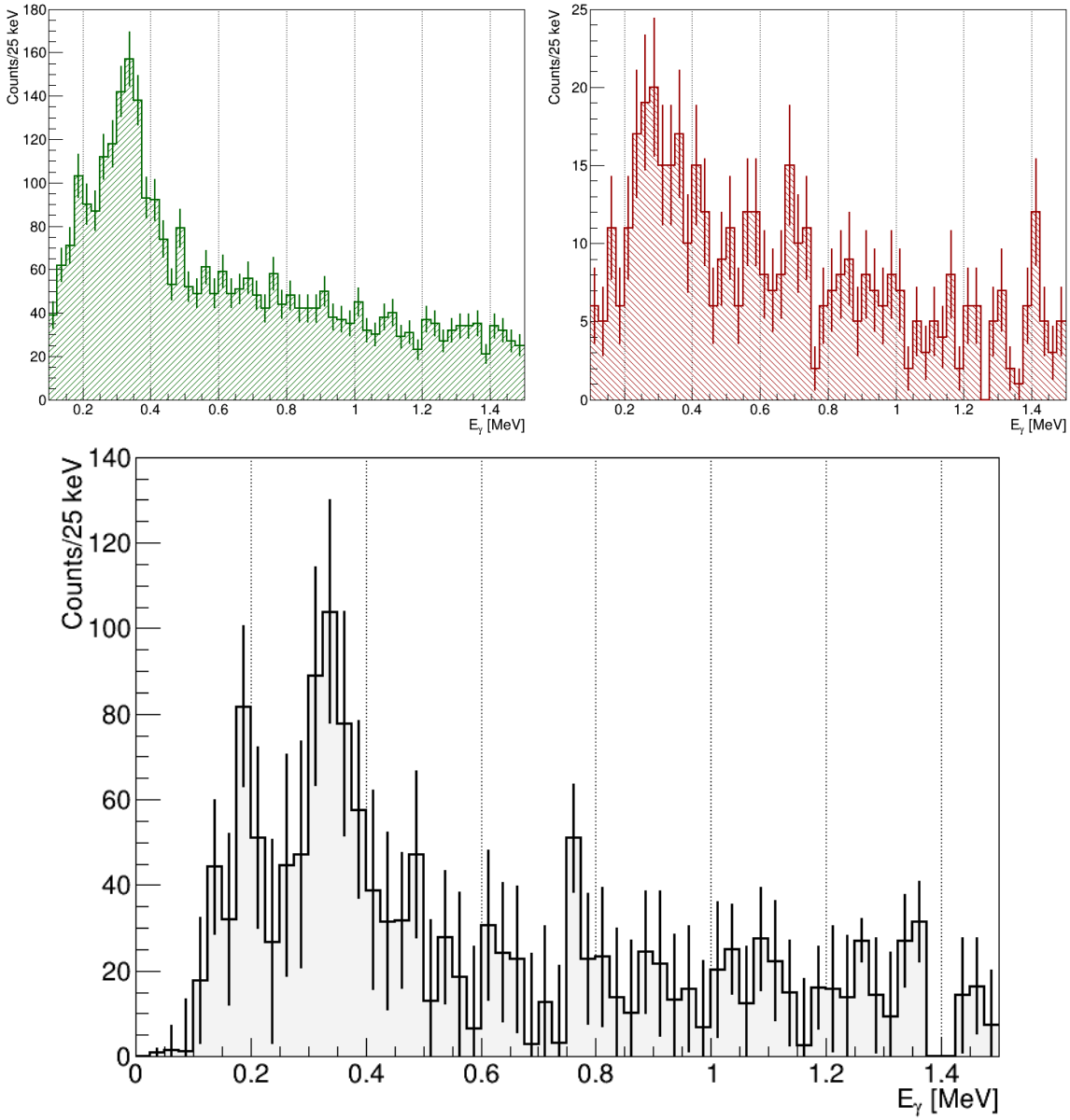

Figure 5.14: Prompt γ-ray energy spectra of ^{17}C in coincidence with one neutron and two protons for CH_2 (top left), C (top right) and reconstructed pure H_2 target (bottom).

Following exactly the same approach of the reconstruction of the pure H_2 relative-energy spectrum described in Section 5.1 both the ^{17}C γ-ray energy spectrum in coincidence with a neutron in Figure 5.12 and the γ-gated relative-energy spectrum in Figure 5.13 also needs to undergo background subtraction in order to make sure that there are no spurious contributions from the C target. The resulting spectrum for the γ-gated spectrum is shown in black in Fig. 5.14 and the the pure H_2 γ-gated relative energy is shown in Fig. 5.15.

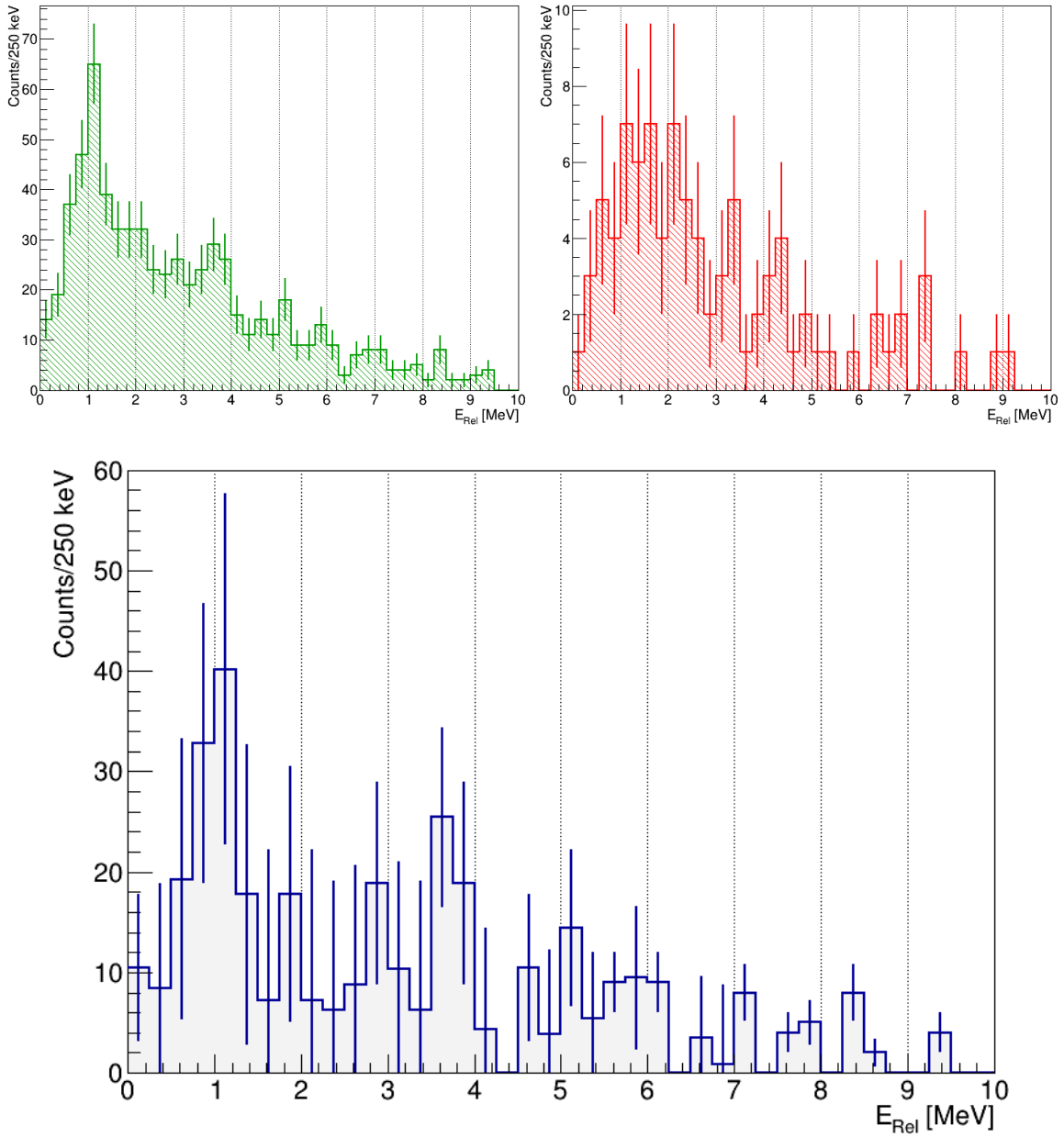

Figure 5.15: Gamma-gated relative-energy spectra for ^{17}C+n in coincidence ^{19}N as incoming particle and the observation of ^{17}C as outgoing fragment in coincidence with two protons in XBall and a neutron in LAND (same subset of event as Figures 5.11 centre and 5.2 centre).

Careful inspection of the prompt γ-ray energy spectra in coincidence with one neutron evaporation events from ^{17}C (see Figure 5.14) was carried out. The small structure observed in the low energy tail of the 335 keV peak for the CH_2 spectrum (top left) does not only remains after the C-background subtraction (bottom), but also seems to be clearer. One may think it is the γ-ray transition corresponding to first excited state of ^{17}C, but we observed it is shifted $\sim$25 keV towards lower energies.

The origin of this shift may be found in the lifetime effect, as for ^{15}C, when we consider the 528 ps lifetime of the first excited state of ^{17}C. While it is not as long to escape detection completely as the ^{15}C first excited state, it is certainly long enough to lead to a significant error in the determination of the scattering angle and, therefore, an inaccurate Doppler correction that could explain the shift towards lower energies.

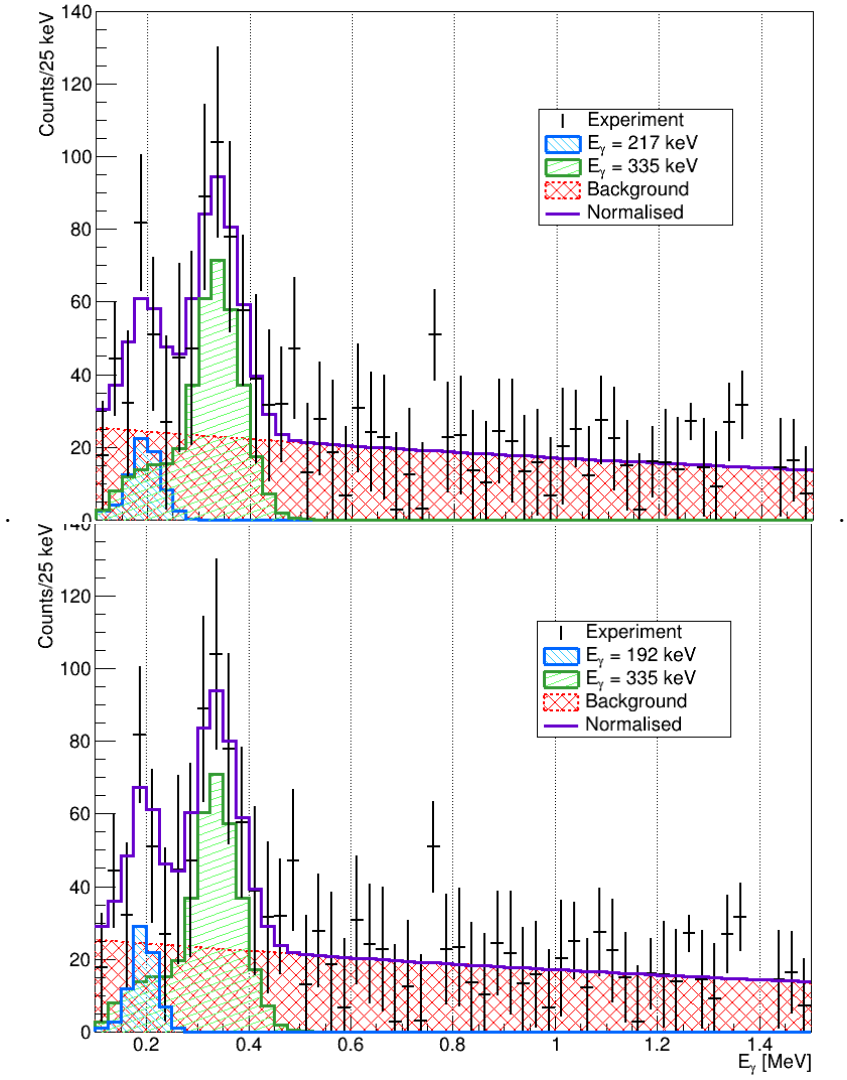

Figure 5.16: Prompt γ-ray spectrum of ^{17}C in coincidence with one neutron and two protons resulting from the reaction $^{19}N(p,2p)^{18}C^{\star} \rightarrow ^{17}C+n$ for the reconstructed pure H_2 target, shown in black. The bright blue and the light green curve are the simulated XBall response function for 335 and 217/192 keV (top/bottom) γ rays. An exponential background is included in red.

In order to gain confidence in the nature of this structure, the background subtracted γ-ray energy spectrum in coincidence with ^{17}C+n events from Figure 5.14 was fitted to the XBall response function for 217 and 335 keV γ-rays (see Section 4.7.1) and an exponential background in Figure 5.16. This operation was repeated with simulations of Xball response to γ rays with energies from 150 to 240 keV, observing that the χ^2 improved and the yield increased for energies lower than 217 keV, reaching a maximum in both yield and goodness of fit at 192 keV.

This reinforces the claim that this structure corresponds to the γ ray from the first excited state in ^{17}C, shifted due to lifetime effects. Therefore, current evidence suggests that some of the resonant states populated in this work decay to the $1/2^+$ state in ^{17}C, although statistics gathered does not allow to identify which unbound states.

The reconstructed pure H_2 target γ-gated relative-energy spectrum for the ^{19}N beam, obtained requesting the observation of a ^{17}C fragment in coincidence with two protons, one neutron and a 335 keV γ ray observed (see Figure 5.15 bottom) was fitted to three, four and five resonances.

This series of fits is performed using the modified Neyman's χ^2_{N*} (Fig. 5.3), which is the modified Neyman's method 4.8.2) but taking the errors as the propagation of the statistical errors of the CH_2 and pure C target (see top panels of Fig. 5.1). The corresponding values of the χ^2_{N*} are shown in Table 5.2, where conspicuously for all fits, the position of the first resonance is in excellent agreement in the different fits. Similarly, the position of the second resonance is in good agreement within one standard deviation. In addition, the fits with three and four resonances agree rather well on a resonance around 5.5 MeV. Concerning the widths, we have a similar scenario: excellent agreement for the first resonance, whilst the second one remains within one standard deviation and, again, fits with three and four resonances match up well with the width of the resonance at 5.5 MeV.

For simplicity, let's call the non-gated relative-energy spectrum (shown in Fig. 5.11), the *full spectrum*. Now, if we compare the γ-gated (Fig. 5.15) and the full spectrum fitted to four resonances in each case, we can clearly see that the first resonant state agrees excellently in both cases. And the higher-lying resonant states are in very good agreement within one standard deviation, this is therefore deemed as the suggestion that the four-resonance fit in the full spectrum is the one that describes our data in the best approximation.

Concerning the widths, the first and the last two resonances agree within one standard deviation. However, as for the second resonance there is a difference although remaining within 2σ, which may be an indication of not only a population by the 335 keV gamma but also directly to the ground state.

Table 5.5: Energy E_{Rel} and width Γ measurements obtained by the Neyman's χ^2_{N*} fit method with three, four and five resonances for the γ gated relative-energy spectrum of $^{17}C+n$.

Fit	Resonance 1		Resonance 2		Resonance 3		Resonance 4		Resonance 5		$\frac{\chi^2}{NDF}$
	E [MeV]	Γ[MeV]	E[MeV]	Γ[MeV]	E [MeV]	Γ [MeV]	E [MeV]	Γ [MeV]	E [MeV]	Γ [MeV]	
3 Resonances	1.00(14)	0.69(71)	3.41(29)	1.00(50)	6.28(40)	0.01(11)					0.728
4 Resonances	1.01(14)	0.76(53)	3.46(27)	0.60(13)	5.57(32)	0.01(11)	7.60(23)	0.34(40)			0.739
5 Resonances	1.01(14)	0.77(47)	3.46(25)	0.62(71)	5.55(31)	0.1(14)	7.51(38)	0.50(57)	8.9(12)	1.9(15)	0.846

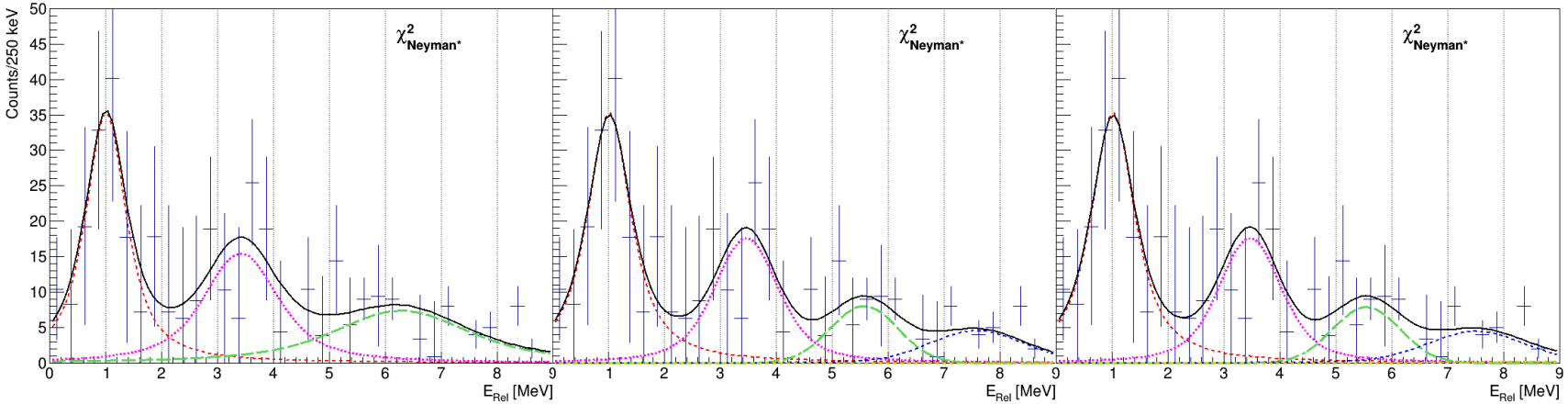

Figure 5.17: H_2 γ gated relative-energy spectra requesting positive identification of ^{19}N as incoming particle and the observation of ^{17}C as outgoing fragment in coincidence with two protons in XBall and a neutron in LAND (same as Figure 5.2 centre), fitted to three (left), four (centre) and five (right) resonances described by Breit-Wigner convoluted with a Gaussian. Results of these fits are presented in Table 5.5.

In the following, the discussion will assume all resonances decay directly to the $5/2^+$ state of ^{17}C because due to the low statistics we are unable to identify which unbound(s) state(s) feed also the $1/2^+$ state in ^{17}C.

Finally, the excitation energy of the resonances found in the relative-energy spectrum at 1.03(10), 3.00(20), 5.31(33) and 7.80(30) MeV is extracted with respect to the ground state of ^{16}C, resulting in 5.54(10), 7.51(20), 9.83(33) and 12.31(30) MeV respectively. A level scheme displaying these results is shown in Figure 5.18.

It is important to note that these excitation energies place all 4 unbound states above the threshold for direct two neutron decay to ^{16}C (see Figure 5.18), and therefore the two neutron evaporation channel is open for all the resonances reported here.

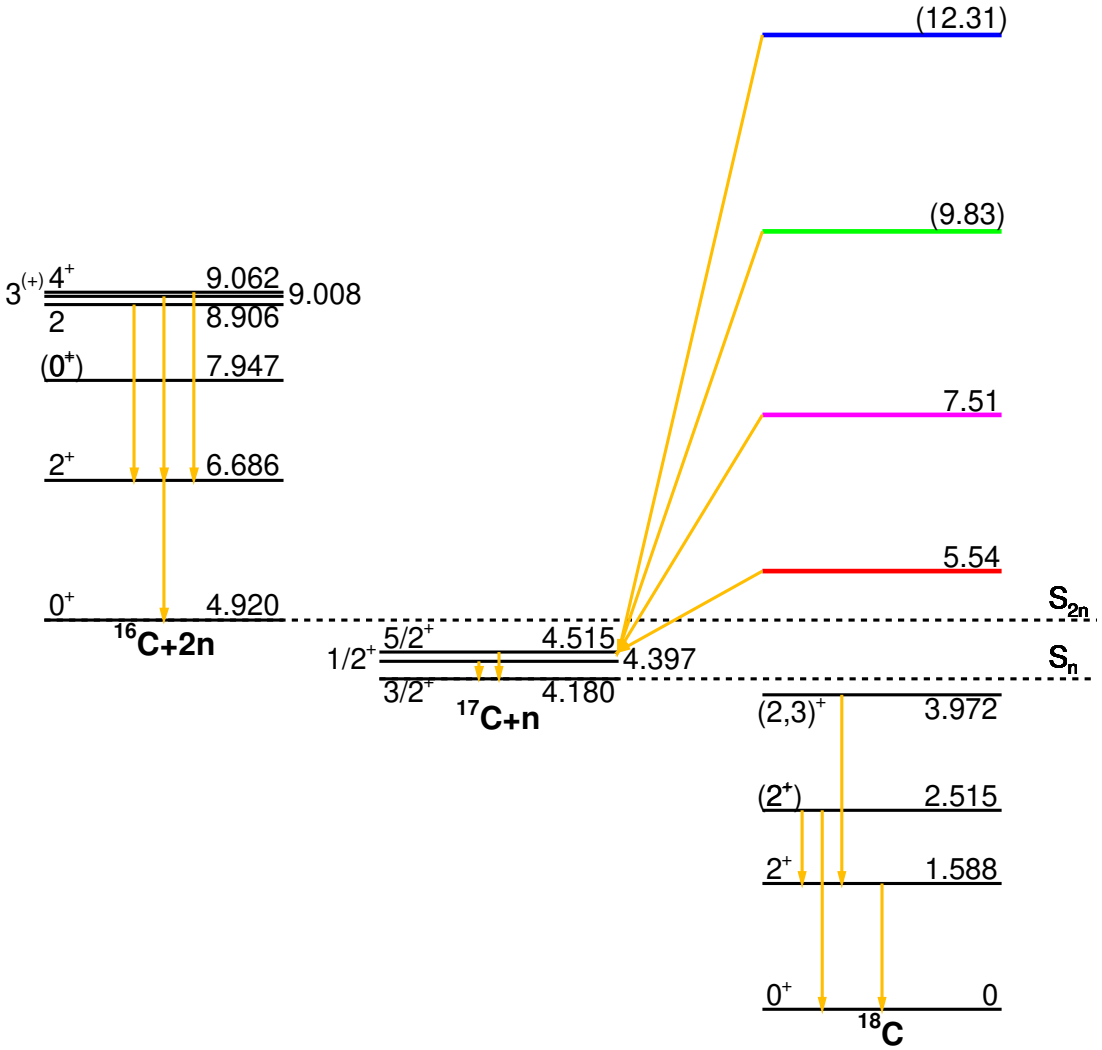

Figure 5.18: Level scheme of ^{18}C, including the unbound states observed in this work at 5.541(10), 7.51(20), 9.83(33) and 12.31(30) MeV, all of them decay through the 335 keV ^{17}C excited state. Dashed lines represent the separation energy of one and two neutrons. In parentheses the energy of the states that can benefit from further evidence.

5.4.2 Exclusive cross sections

Experimental exclusive cross sections are calculated for the unbound states reported in this work as previously explained in Subsection 5.2.1 and presented in table 5.6, together with the neutron detection efficiency associated to their location in relative energy and their observed width. Uncertainties presented account for errors in target thickness, incoming number of events and detection efficiency of protons and neutrons, but are largely dominated by the error in the observed yield corresponding to each resonant state, due to the statistical uncertainty in the fit results.

E* [MeV]	E_{Rel} [MeV]	Γ [MeV]	ϵ_n [%]	σ_{exc} [mb]
5.54(10)	1.03(10)	0.81(29)	83.07(7)	1.16(36)
7.51(20)	3.00(20)	1.37(54)	74.71(5)	1.06(59)
9.83(33)	5.31(33)	0.33(178)	34.6(3)	$0.33^{+0.30}_{-0.33}$
12.31(30)	7.80(30)	0.01(166)	21.1(1)	$0.17^{+0.04}_{-0.17}$

Table 5.6: ^{17}C+n cross sections for the population of the unbound states following the $(p, 2p)$ reaction. The excitation energy $E*$ is obtained by summing up E_{Rel}, the 335 keV contribution from the γ ray and the separation energy of one neutron of ^{18}C, S_n=4180(3) keV.

Note that the exclusive cross sections reported here only account for the events that are observed to decay via one neutron emission to ^{17}C. However, we have seen already that the resonant states observed here were all found beyond the two neutron separation energy, and hence the two neutron decay channel to ^{16}C is open for all of them. The analysis of the two neutron evaporation channel is not concluded.

5.5 Theoretical Predictions

In this section, the excitation energies measured and presented in the level schemes 5.10 and 5.18 are compared to shell model calculations performed by B.A. Brown [94].

The WBP, WBT interactions [95] and a modified version of the WBT Hamiltonian, with a reduction of 25% in the neutron-neutron two body matrix elements (TBME), as indicated in [12], called WBT*, were used to describe the structure of ^{18}C and ^{16}C. These calculations were performed in the full spsdpf-model space truncated to two excitations across a major shell ($\hbar\omega$) and restricted to positive parity states.

All the excited states predicted by these calculations are shown for the regions of interest, i.e. up to 10 MeV for ^{16}C and up to 13 MeV for ^{18}C, although the discussion will be restricted to 1^+ and 2^+ states because this reaction channel cannot populate higher J states.

As for the ^{16}C measurements (see Fig. 5.19), no 1^+ or 2^+ states are predicted by any of the three models close to the first resonant state observed in this work at 5.71(6) MeV. The closest unbound 2^+ states in WBP and WBT lie at 4.789 and 4.934 MeV respectively. Both WBP and WBT interactions predict a 3^+ state within two standard deviations, at 5.564 and 5.691 MeV respectively, but the population of this state is forbidden via one-proton knockout reactions.

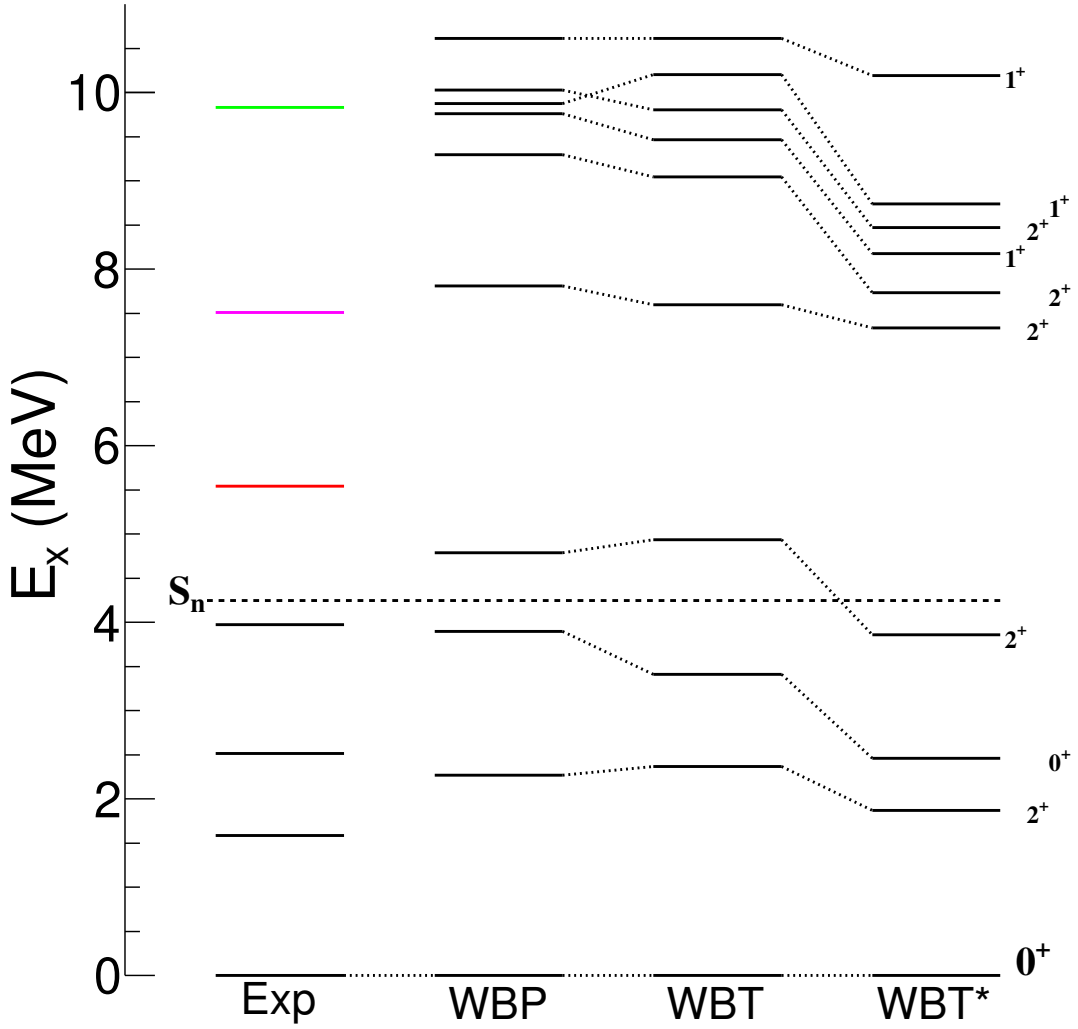

Figure 5.19: Level scheme of ^{16}C, where the unbound states observed in this work at 5.71(6), 7.83(4) and 9.78(88) MeV are shown in colours in the first column in comparison with the shell model calculations performed with WBP, WBT and WBT in the spsdpf-model space.*

In contrast, the excellent agreement of the 2^+ predicted at 7.808, 7.598 and 7.337 by WBP, WBT and WBT* interactions respectively, with the unbound state observed in this work at 7.83(41) MeV could perhaps be a strong indication of a 2^+ spin and parity assignment for this state.

Similarly, higher lying 1^+ at 9.764, 9.464 and 10.191 in WBP, WBT and WBT* respectively, and 2^+ in WBP and WBT lying at 9.807 and 9.299 respectively, also lie within uncertainty with the observed state at 9.78(88) MeV in ^{16}C in this work. However, this would need careful investigation before assigning a spin and parity.

Regarding the level scheme of ^{18}C (see Fig. 5.20), the 2^+ in WBT*, lying at 5.505 MeV seems to be the calculation that best agrees with the first resonant state measured in this work at 5.54(10) MeV. However, the 1^+ in WBP and WBT at 5.20 and 5.25 MeV respectively also seem to be in agreement within two standard deviations.

Giving the numerous higher-lying 1^+ and 2^+ excited states at energies ranging from 9 to 13 MeV in ^{18}C, many levels are within one standard deviation, thus, it is difficult to predict, which spin and parity would model the experimental result at 9.83(33) and 12.31(30) MeV in the best approximation.

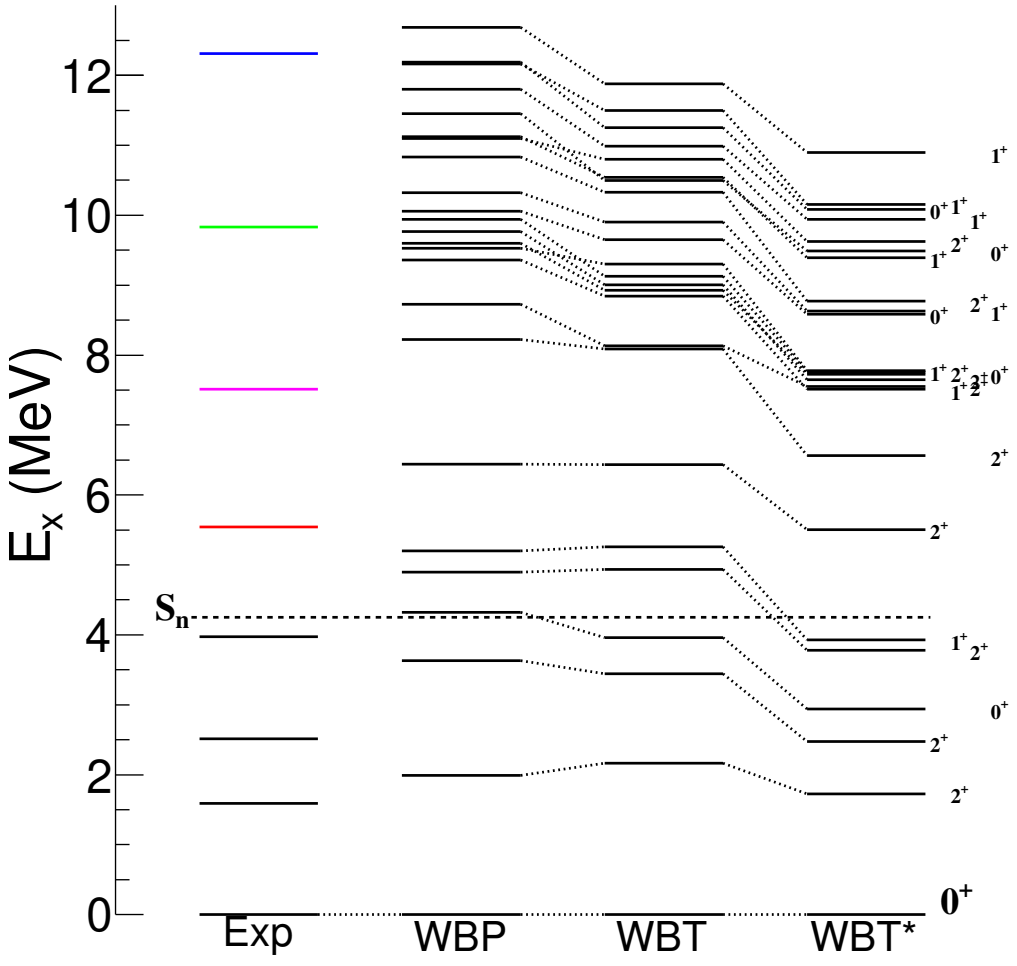

Figure 5.20: Comparing level scheme of ^{18}C unbound states with shell-model calculations performed with WBP, WBT and WBT in the spsdpf-model space. Level scheme of ^{18}C, including the unbound states observed in this work at 5.54(10), 7.51(20), 9.83(33) and 12.31(30) MeV.*

This work also aims to estimate proton amplitudes and spectroscopic factors for the observed unbound states, however these results are not presented since, at the time of writing, theoretical predictions for the cross sections have not been made available yet.

Chapter 6

Conclusions and outlook

This thesis focused on the analysis of the one neutron evaporation channels of neutron-rich carbon isotopes driven by the motivation on the first spin-orbit gap between the $p_{1/2} - p_{3/2}$ orbits since it has been recently confirmed that there is a weakening in the splitting Z = 6 due to an influence of the tensor and two-body spin-orbit forces [3]. In recent years, studies on the quadrupole transition strength $B(E2; 2_1^+ \rightarrow 0_{g.s.}^+)$ of ^{16}C, ^{18}C and ^{20}C [15, 17, 21] have been carried out. Shell-model calculations in the *p* shell-model space for protons and the *sd* shell-model space for neutrons have been performed by Petri *et al.* [15]. The $B(E2; 2_1^+ \rightarrow 0_{g.s.}^+)$ strength as well as the level scheme is calculated for ^{16}C, ^{18}C and ^{20}C probing different two-body nucleon-nucleon interactions, showing a neutron-dominant nature of the first excited 2^+ state [17]. Therefore, this work aims to elucidate the neutron component of the mixed-symmetry 2^+ state of carbon isotopic chain, which is expected above the neutron separation energy. For that purpose, unbound states in ^{16}C, ^{18}C and ^{20}C have been probed via quasi-free scattering (p, 2p) reactions from ^{17}N, ^{19}N, and ^{21}N beams, respectively.

The experiment took place at GSI, Germany, using the R^{3}B/LAND setup, where excited states in ^{16}C, ^{18}C and ^{20}C were populated by inverse kinematics via quasi-free scattering $(p, 2p)$ reactions from ^{17}N, ^{19}N, and ^{21}N beams produced by a primary beam of ^{40}Ar impinging on a 4011 mg/cm^2 Be production target.

The invariant mass method was used to study the unbound states. From the measurements of the momenta of outgoing fragments and neutrons, the two-body relative energy spectra are reconstructed for one-neutron decay events from ^{16}C and ^{18}C. These relative energy spectra are scanned for resonances, described by a Breit-Wigner function convoluted with a Gaussian that accounts for the resolution of LAND, where the height, position and width of the resonances were fitted to the data. The results of this analysis indicate that three unbound states located at 5.71(06), 7.83(41) and 9.78(88) MeV are populated in ^{16}C and that four resonant states are observed at 5.54(10), 7.51(20), 9.83(33) and 12.31(30) MeV for

^{18}C. Coincidence with γ rays were also investigated, observing that all four unbound states observed for ^{18}C decay to the $5/2^+$ state in ^{17}C instead of its ground state. No γ ray was observed in coincidence with any of the states reported for ^{16}C, albeit further investigation is required to know whether this is due to direct decay to ^{15}C ground state or setup limitations that prevent the observation of the γ-ray from the first excited state in ^{15}C because of its long lifetime.

The preliminary exclusive cross sections of the resonant states measured for ^{16}C and ^{18}C were reported, taking into account only the one neutron evaporation channels. Work is ongoing to analyse ^{14}C+2n and ^{16}C+2n events to obtain the contribution to the exclusive cross section due to the possible two-neutron decay branch of all the aforementioned unbound states.

Although this thesis was initially meant to focus on ^{16}C, ^{18}C and ^{20}C, the statistics of the latter was not sufficient to proceed using the same approaches described along this manuscript.

Appendices

Appendix A

Bound States

A.1 γ-ray spectra

Figure A.1 shows the γ-ray spectra for the reconstructed pure H_2 target.

A.2 Cross sections

The inclusive cross sections were calculated for the ^{A}N(p,2p)$^{A-1}$C reactions of interest and are enlisted in Table A.1 in comparison to those published in Ref. [3]. For these calculations, the number of ions of outgoing nitrogen isotopes were taken as an approximation of the incoming isotopes and the efficiencies of two-proton events ϵ_{2p} for the ^{17}N(p,2p)^{16}C, ^{19}N(p,2p)^{18}C and ^{21}N(p,2p)^{20}C reactions were $\epsilon_{2p} = 57.4(3)\%$ and $55.4(3)\%$ respectively, obtained from R3BROOT simulations performed by I. Syndikus [85].

Table A.1: Experimental inclusive cross sections obtained in this work and compared to the values obtained by I. Syndikus [3]. Last column shows the ratio between the cross sections obtained in this work and those in [3].

	this work σ_{exp}[mb]	I. Syndikus σ_{exp}[mb]	ratio
^{17}N(p,2p)^{16}C	3.86(28)	3.82(19)	1.01
^{21}N(p,2p)^{20}C	2.55(42)	2.65(34)	0.96

Our cross-section measurements for ^{17}N(p,2p)^{16}C and ^{21}N(p,2p)^{20}C are in good agreement with those published in Ref. [3] and also for the latter case in Ref. [96]. Further work is needed to obtain ^{19}N(p,2p)^{18}C cross section.

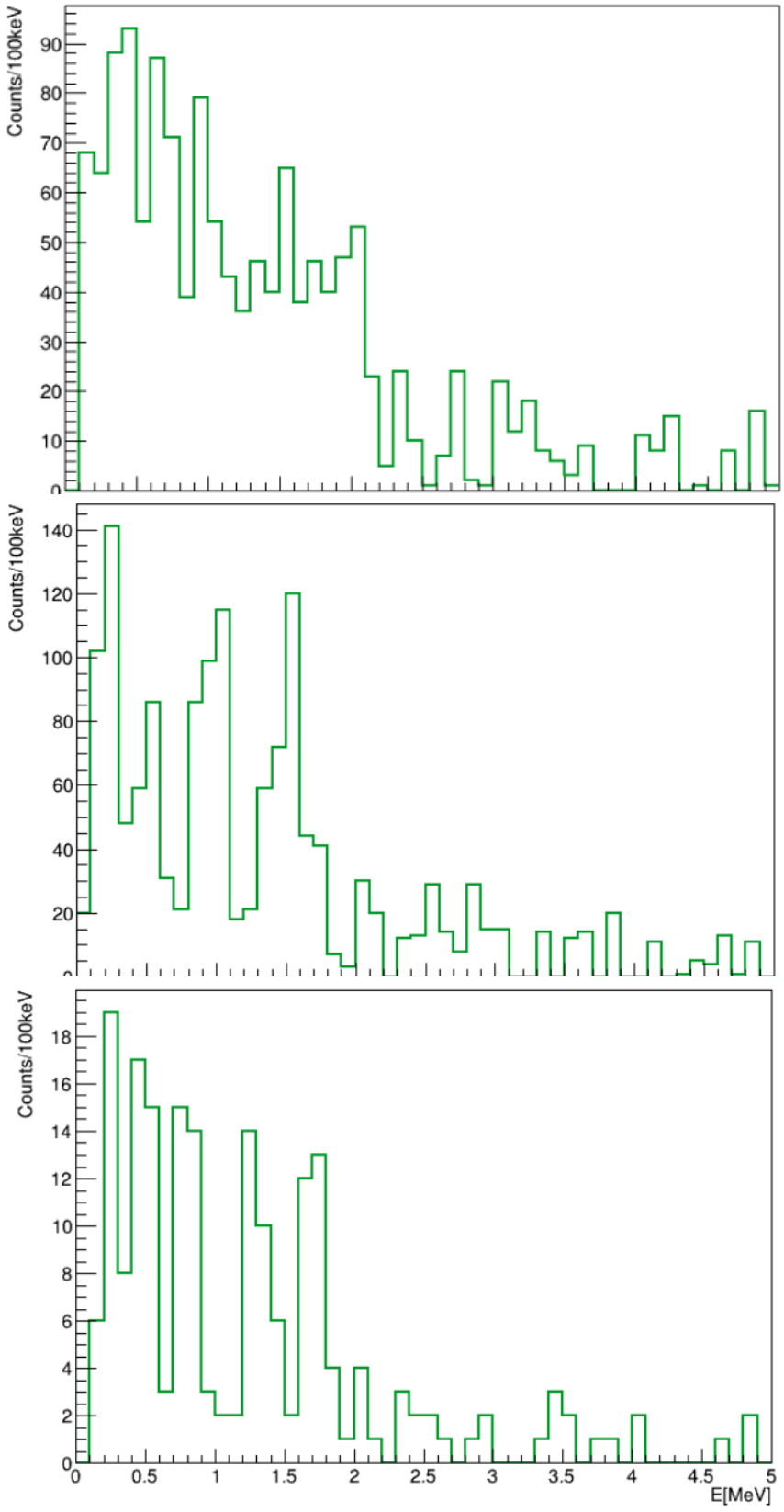

Figure A.1: γ-ray spectra for the reactions $^{17}N(p,2p)^{16}C$ (top), $^{19}N(p,2p)^{18}C$ (centre), and $^{21}N(p,2p)^{20}C$ (bottom) for the pure proton reconstructed target.

Appendix B

Fit methods

As mentioned before within the body of the thesis in Section 4.8.2, there are several fitting methods available, and hence it is required a procedure to assess how well suited a fitting result is to describe the data and how it compares to the fitting results from other methods, in order to determine the best model to describe the experimental data.

The most common method to evaluate the goodness of fit is through the χ^2 function, which definition can vary depending on the choice of errors:

- **Pearson's χ^2_P:** errors from the prediction model y_i.

$$\chi^2_P = \sum_{i=1}^{N} \frac{(n_i - y_i)^2}{y_i} \tag{B.1}$$

- **Neyman's χ^2_N:** uncertainty from the experimental data, where $\Delta n_i = \sqrt{n_i}$.

$$\chi^2_N = \sum \frac{(n_i - y_i)^2}{n_i} = \sum \frac{(n_i - y_i)^2}{(\Delta n_i)^2} \tag{B.2}$$

  - **Neyman's modified χ^2_N*:** modification of the χ^2_N for our case where the distribution to be fitted is a background subtracted histogram, and the error chosen arise from the propagation of the Neymann's errors from the parent distributions.

Besides χ^2 methods, likelihood method was also tested and compared to aforementioned χ^2 tests using the relation:

$$\chi^2_L = -2\ Ln(P) \tag{B.3}$$

In this appendix, fits presented on Chapter 5 are performed using all χ^2_P, χ^2_N, χ^2_N* and χ^2_L tests to show that the choice of fitting method does not influence the results.

B.1 $^{16}C^{\star} \rightarrow ^{15}C+n$ (section 5.3)

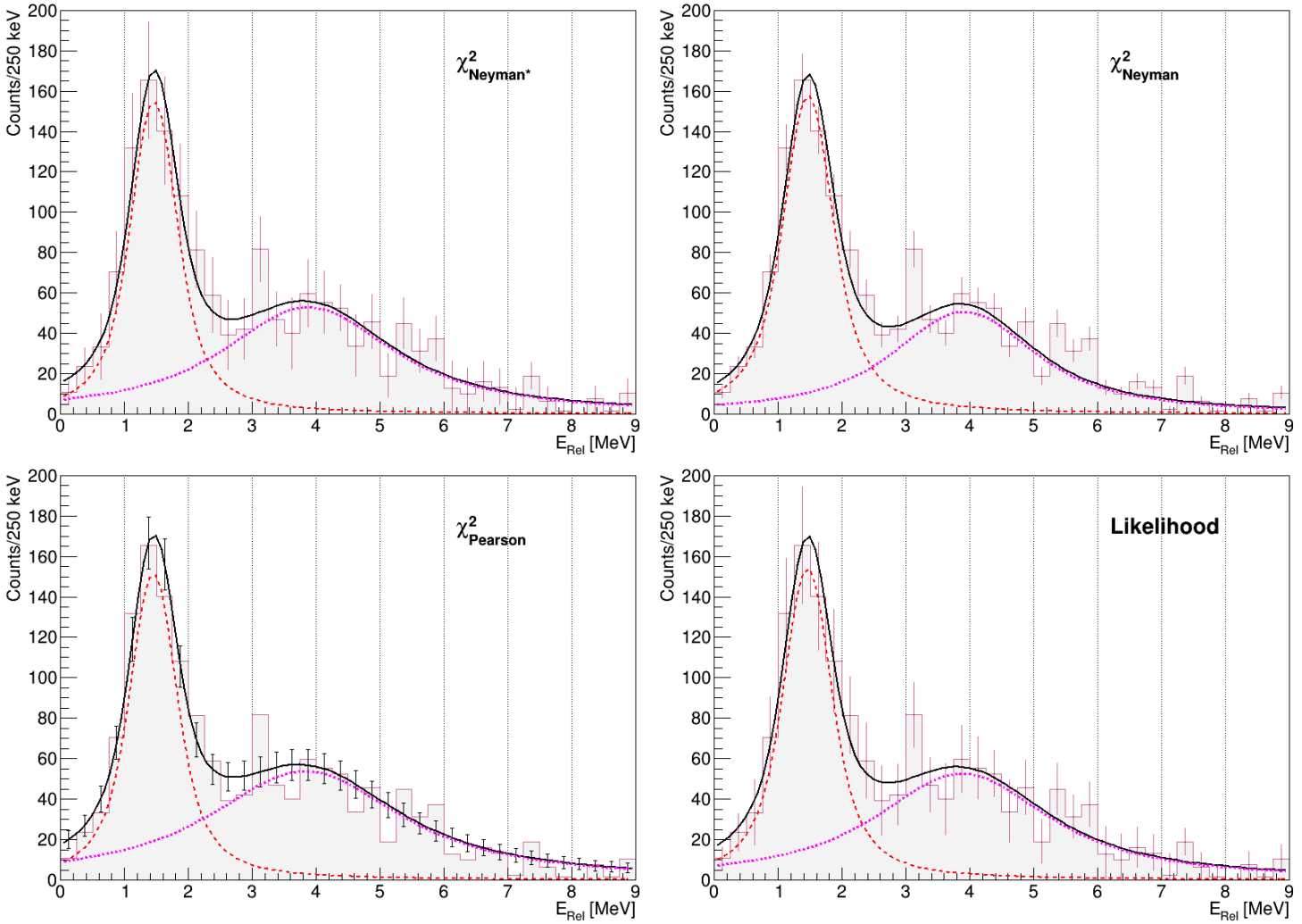

Figure B.1: H_2 relative energy spectra requesting positive identification of ^{17}N as incoming particle and the observation of ^{15}C as outgoing fragment in coincidence with 2 protons in Xball and a neutron in LAND, fitted to 2 resonances using χ^2_N* (top left), χ^2_N (top right), χ^2_P (bottom left) and χ^2_L (bottom right) methods. Results of these fits are presented in Table B.2.

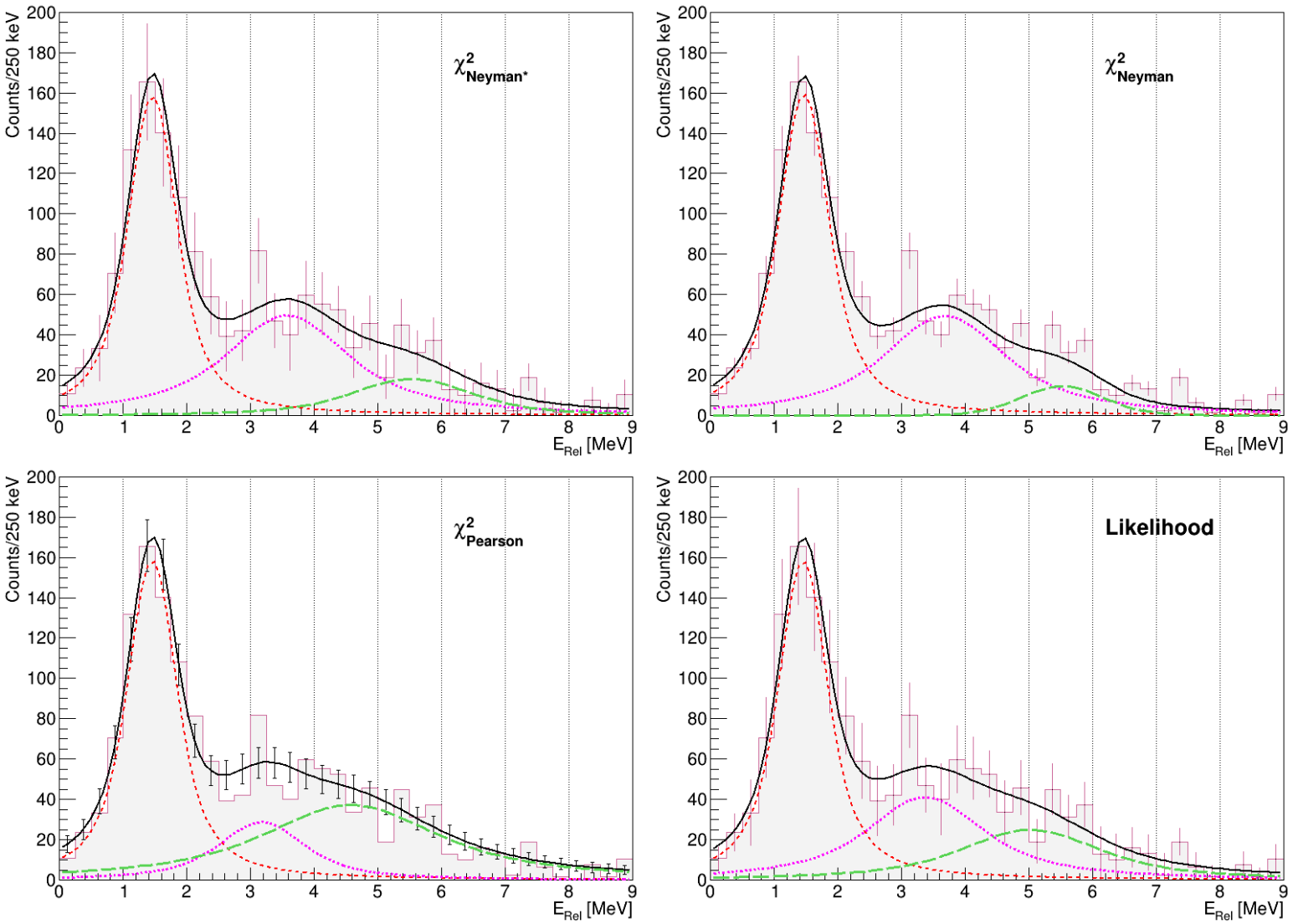

Figure B.2: H_2 relative energy spectra requesting positive identification of ^{17}N as incoming particle and the observation of ^{15}C as outgoing fragment in coincidence with 2 protons in Xball and a neutron in LAND, fitted to 3 resonances using χ^2_N* (top left), χ^2_N (top right), χ^2_P (bottom left) and χ^2_L (bottom right) methods. Results of these fits are presented in Table B.2.

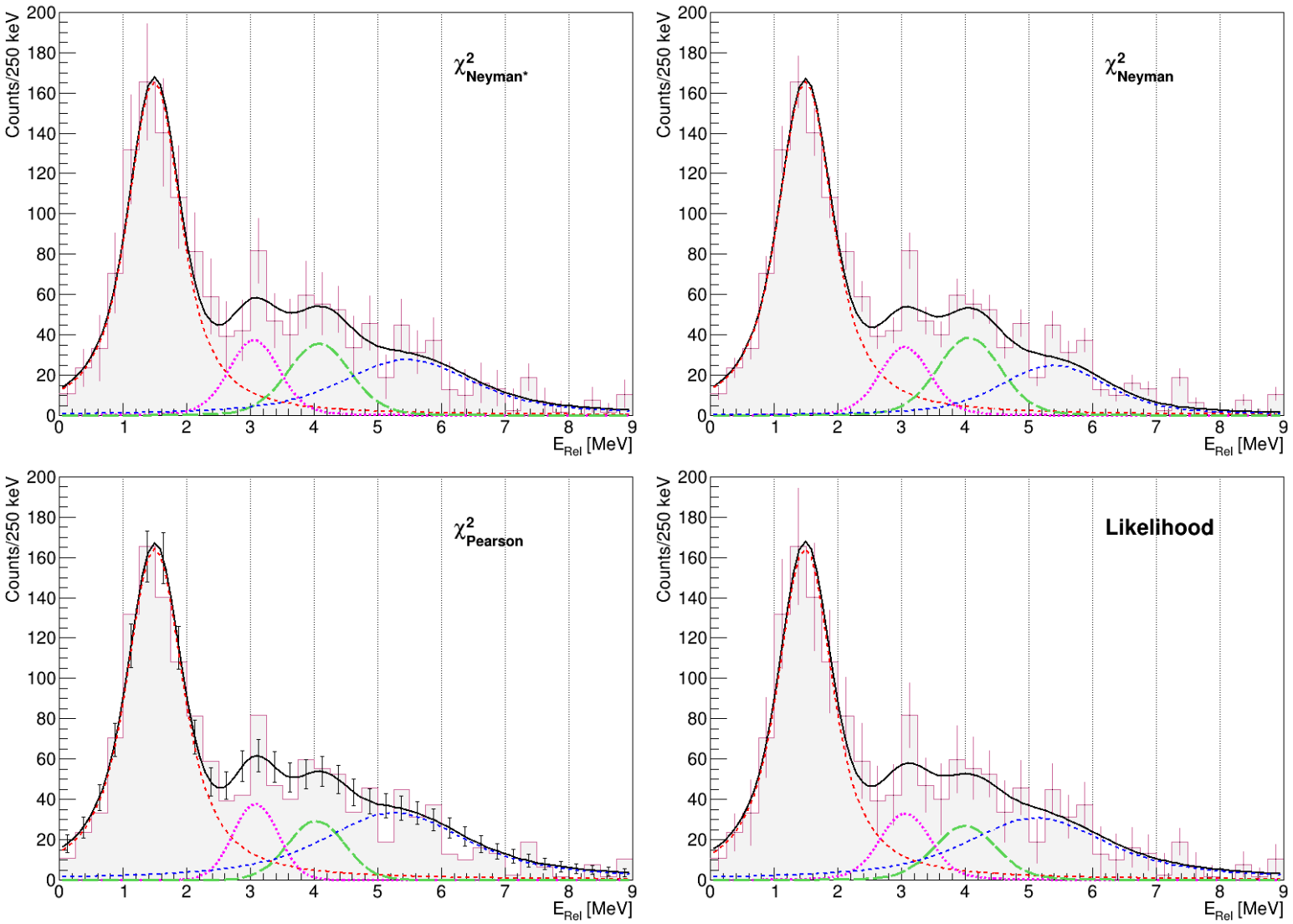

Figure B.3: H_2 relative energy spectra requesting positive identification of ^{17}N as incoming particle and the observation of ^{15}C as outgoing fragment in coincidence with 2 protons in Xball and a neutron in LAND, fitted to 4 resonances using χ^2_N* (top left), χ^2_N (top right), χ^2_P (bottom left) and χ^2_L (bottom right) methods. Results of these fits are presented in Table B.2.

Table B.1: Energy E_{Rel} and width Γ measurements obtained by the Neyman's χ^2_N,Neyman's modified χ^2_{N*}, Pearson's χ^2_P and likelihood L fitted to different number of resonances for the pure H_2 relative energy spectra of ^{15}C+n.

Fit		Resonance 1		Resonance 2		Resonance 3		Resonance 4	
		E_{Rel}	Γ	E_{Rel}	Γ	E_{Rel}	Γ	E_{Rel}	Γ
2 Resonances	χ^2_N*	1.46(6)	0.58(15)	3.88(26)	2.88(54)				
	χ^2_N	1.47(2)	0.66(6)	3.91(11)	2.27(21)				
	χ^2_P	1.45(5)	0.59(18)	3.83(32)	3.30(65)				
	L	1.46(2)	0.62(7)	3.89(13)	2.92(26)				
3 Resonances	χ^2_N*	1.46(6)	0.62(17)	3.57(40)	1.94(14)	5.53(88)	1.3(24)		
	χ^2_N	1.46(2)	0.67(7)	3.68(12)	1.89(30)	5.53(14)	0.20(50)		
	χ^2_P	1.45(7)	0.65(21)	3.17(62)	1.2(22)	4.6(12)	2.89(94)		
	L	1.45(3)	0.65(9)	3.37(32)	1.8(10)	5.02(63)	1.99(95)		
4 Resonances	χ^2_N*	1.49(40)	0.74(13)	3.07(13)	0.01(68)	4.07(18)	0.01(73)	5.41(44)	1.7(15)
	χ^2_N	1.49(7)	0.77(06)	3.07(06)	0.01(68)	4.06(08)	0.01(17)	5.35(17)	1.04(36)
	χ^2_P	1.49(33)	0.79(15)	3.07(01)	0.20(41)	4.0(13)	0.01(77)	5.26(63)	2.0(40)
	L	1.49(2)	0.77(06)	3.07(07)	0.01(50)	4.00(12)	0.01(51)	5.10(18)	2.0(12)

B.2 $^{18}C^{\star} \rightarrow ^{17}C+n$ (section 5.4)

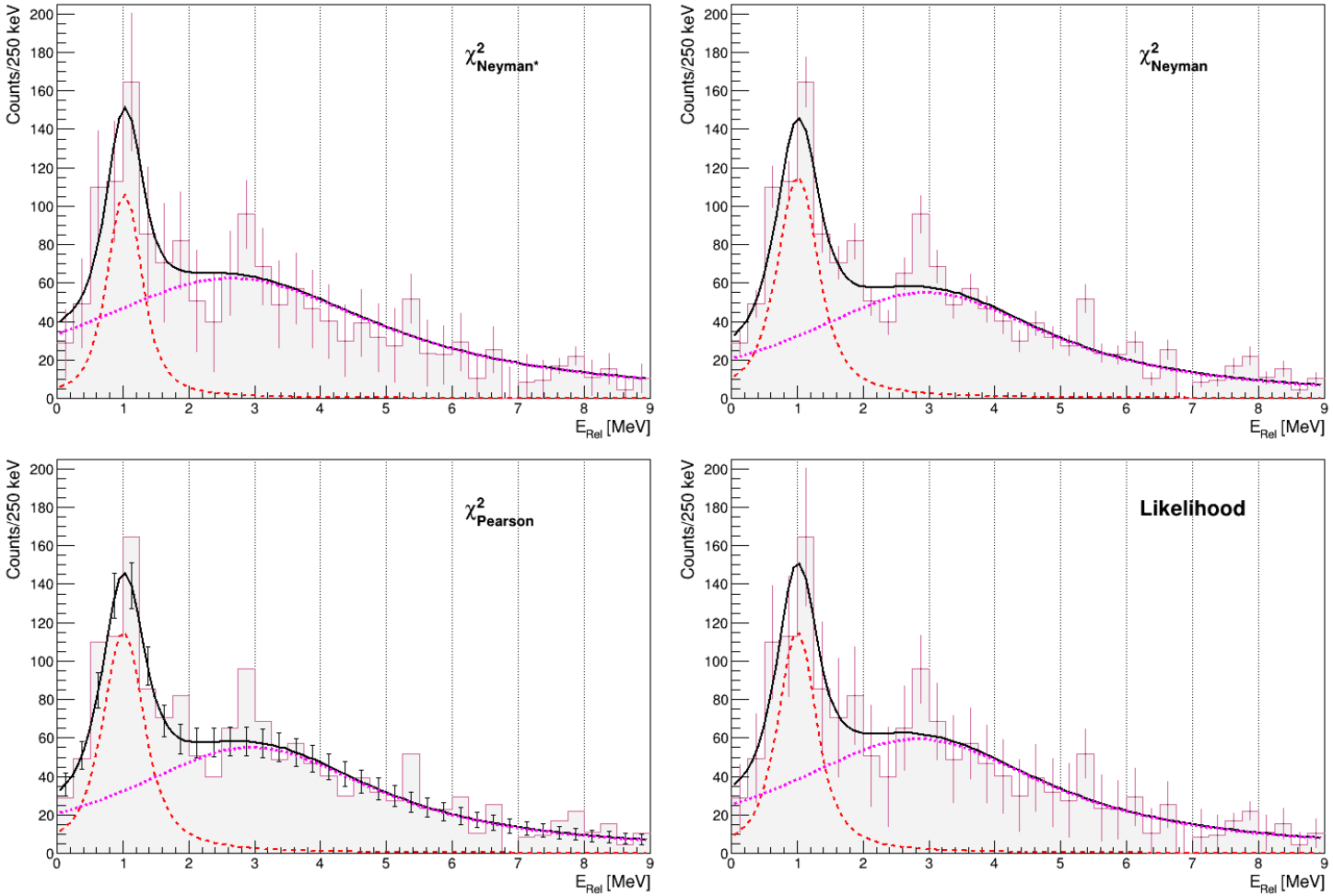

Figure B.4: H_2 relative energy spectra requesting positive identification of ^{17}N as incoming particle and the observation of ^{17}C as outgoing fragment in coincidence with 2 protons in Xball and a neutron in LAND, fitted to 2 resonances using χ^2_N* (top left), χ^2_N (top right), χ^2_P (bottom left) and χ^2_L (bottom right) methods. Results of these fits are presented in Table B.2.

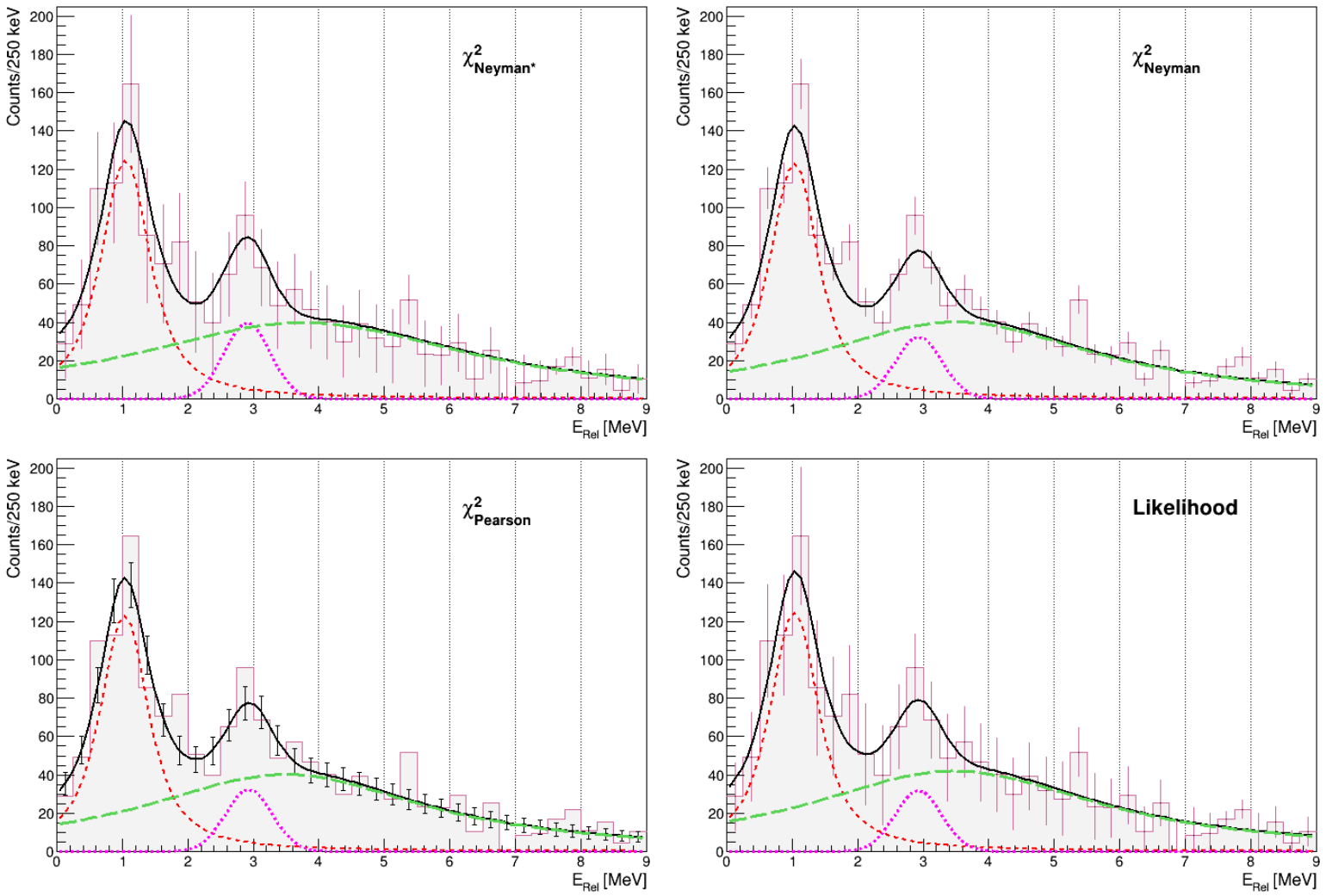

Figure B.5: H_2 relative energy spectra requesting positive identification of ^{17}N as incoming particle and the observation of ^{17}C as outgoing fragment in coincidence with 2 protons in Xball and a neutron in LAND, fitted to 3 resonances using χ^2_N* (top left), χ^2_N (top right), χ^2_P (bottom left) and χ^2_L (bottom right) methods. Results of these fits are presented in Table B.2.

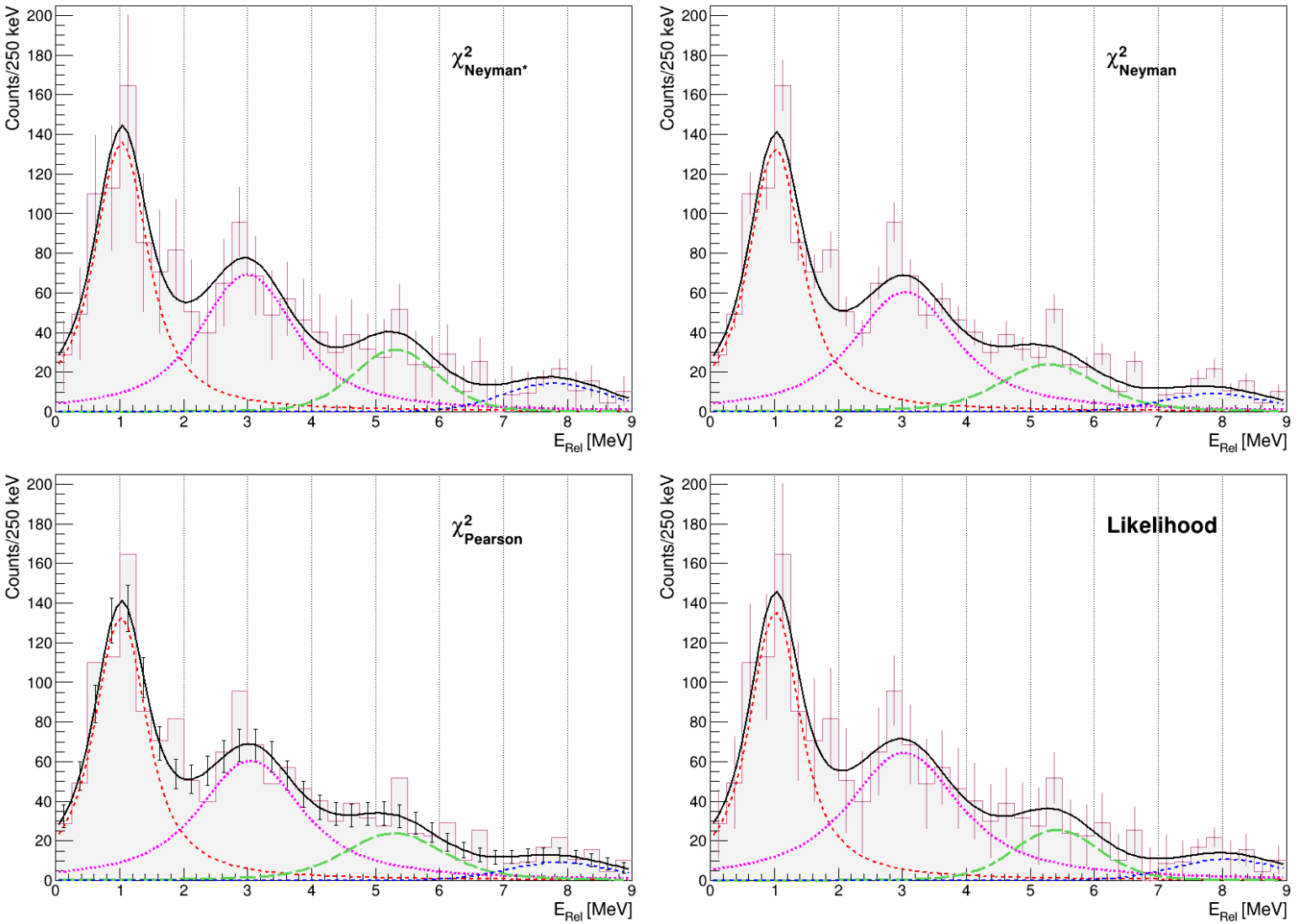

Figure B.6: H_2 relative energy spectra requesting positive identification of ^{17}N as incoming particle and the observation of ^{17}C as outgoing fragment in coincidence with 2 protons in Xball and a neutron in LAND, fitted to 4 resonances using χ^2_N* (top left), χ^2_N (top right), χ^2_P (bottom left) and χ^2_L (bottom right) methods. Results of these fits are presented in Table B.2.

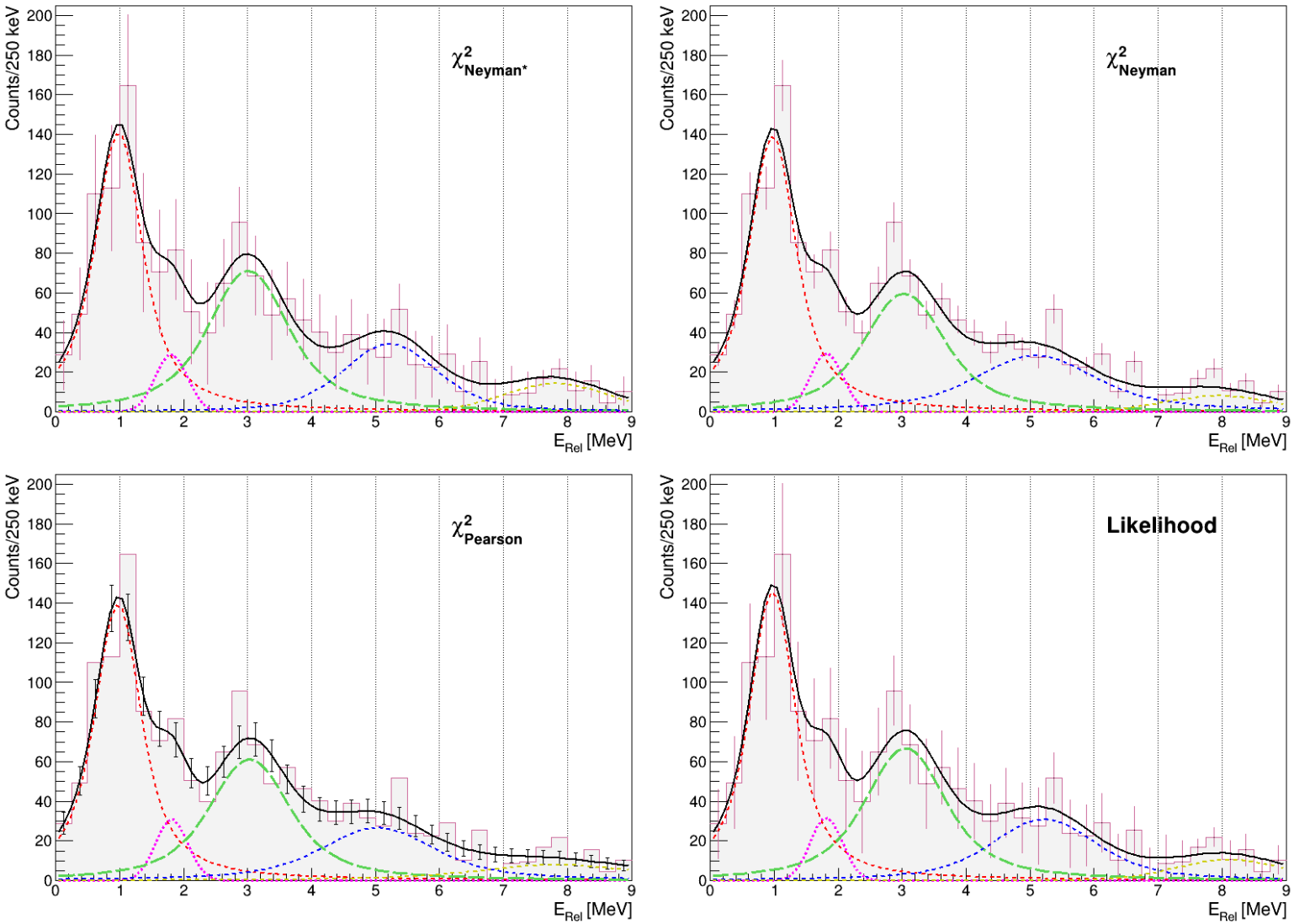

Figure B.7: H_2 relative energy spectra requesting positive identification of ^{17}N as incoming particle and the observation of ^{17}C as outgoing fragment in coincidence with 2 protons in Xball and a neutron in LAND, fitted to 5 resonances using χ^2_N* (top left), χ^2_N (top right), χ^2_P (bottom left) and χ^2_L (bottom right) methods. Results of these fits are presented in Table B.2.

Table B.2: Energy E_{Rel} and width Γ measurements obtained by the Neyman's χ^2_N,Neyman's modified χ^2_{N*}, Pearson's χ^2_P and likelihood L fitted to different number of resonances for the pure H_2 relative energy spectra of ^{17}C+n.

Fit		Resonance 1		Resonance 2		Resonance 3		Resonance 4		Resonance 5	
		E_{Rel}	Γ	E_{Rel}	Γ	E_{Rel}	Γ	E_{Rel}	Γ	E_{Rel}	Γ
2 Resonances	χ^2_N*	1.02(9)	0.37(31)	2.64(59)	5.55(91)						
	χ^2_N	1.01(3)	0.53(11)	2.95(19)	4.47(38)						
	χ^2_P	1.01(3)	0.53(11)	2.95(19)	4.47(38)						
	L	1.00(3)	0.47(10)	2.82(20)	4.73(36)						
3 Resonances	χ^2_N*	1.05(10)	0.71(35)	2.90(15)	0.01(117)	3.76(133)	6.01(149)				
	χ^2_N	1.03(3)	0.70(11)	2.93(6)	0.01(14)	3.48(31)	5.00(132)				
	χ^2_P	1.03(3)	0.70(11)	2.93(6)	0.01(14)	3.48(31)	5.00(132)				
	L	1.03(3)	0.71(15)	2.92(7)	0.01(14)	3.48(45)	5.20(50)				
4 Resonances	χ^2_N*	1.03(10)	0.81(29)	3.00(20)	1.37(54)	5.31(33)	0.33(178)	7.80(30)	0.01(166)		
	χ^2_N	1.02(3)	0.80(11)	3.04(10)	1.51(74)	5.29(23)	0.78(128)	7.87(20)	0.01(138)		
	χ^2_P	1.02(3)	0.80(11)	3.05(10)	1.52(74)	5.29(22)	0.78(128)	7.87(20)	0.01(138)		
	L	1.01(3)	0.78(12)	3.03(10)	1.71(77)	5.41(15)	0.34(52)	8.05(19)	0.01(42)		
5 Resonances	χ^2_N*	0.98(10)	0.71(25)	1.81(20)	0.01(134)	3.00(18)	0.83(140)	5.18(57)	0.83(135)	7.82(30)	0.01(161)
	χ^2_N	0.98(3)	0.70(8)	1.82(6)	0.01(6)	3.01(6)	0.85(14)	5.04(14)	1.55(25)	7.90(20)	0.12(100)
	χ^2_P	0.98(3)	0.70(8)	1.82(6)	0.01(6)	3.02(6)	0.85(14)	5.04(14)	1.55(25)	7.90(20)	0.12(100)
	L	0.97(3)	0.68(8)	1.82(6)	0.0(13)	3.04(6)	0.85(16)	5.14(13)	1.24(48)	8.12(25)	0.01(22)

Bibliography

[1] Petri M., S. Paschalis, R.M. Clark, P. Fallon, A.O. Macchiavelli, K. Starosta, T. Baugher, D. Bazin, L. Cartegni, H.L. Crawford, et al. Structure of ^{16}C: Testing shell model and ab initio approaches. *Physical Review C*, 86(4):044329, 2012.

[2] AO Macchiavelli, M Petri, P Fallon, S Paschalis, RM Clark, M Cromaz, and IY Lee. Phenomenological analysis of B(E2) transition strengths in neutron-rich carbon isotopes. *Physical Review C*, 90(6):067305, 2014.

[3] I. Syndikus et al. Probing the Z = 6 spin-orbit shell gap with (p,2p) quasi-free scattering reactions. *Physics Letters*, B:135748, 2020.

[4] I.Tanihata. Neutron halo nuclei. *Journal of Physics G: Nuclear and Particle Physics*, 22(2):157–198, 1996.

[5] O. Sorlin and M. G. Porquet. Nuclear magic numbers: New features far from stability. *Progress in Particle and Nuclear Physics*, 61(2):602 – 673, 2008.

[6] Takaharu Otsuka, Alexandra Gade, Olivier Sorlin, Toshio Suzuki, and Yutaka Utsuno. Evolution of shell structure in exotic nuclei. *Rev. Mod. Phys.*, 92:015002, Mar 2020.

[7] A.V. Dobrovolsky. Nuclear matter distributions in the neutron-rich carbon isotopes 1417c from intermediate-energy proton elastic scattering in inverse kinematics. *Nuclear Physics A*, 1008:122154, 2021.

[8] X. Pereira-López et al. Low-lying single-particle structure of ^{17}C and the N = 14 sub-shell closure. *Physics Letters B*, 811:135939, 2020.

[9] D. Bazin et al. One-neutron halo of ^{19}C. *Phys. Rev. Lett.*, 74:35693572, May 1995.

[10] D. Q. Fang et al. One-neutron halo structure in ^{15}C. *Phys. Rev. C*, 69:034613, Mar 2004.

[11] M. Stanoiu et al. N = 14 and 16 shell gaps in neutron-rich oxygen isotopes. *Phys. Rev. C*, 69:034312, Mar 2004.

[12] M. Stanoiu, D. Sohler, O. Sorlin, F. Azaiez, Zs. Dombrádi, B. A. Brown, M. Belleguic, C. Borcea, C. Bourgeois, Z. Dlouhy, Z. Elekes, Zs. Fülöp, S. Grévy, D. Guillemaud-Mueller, F. Ibrahim, A. Kerek, A. Krasznahorkay, M. Lewitowicz, S. M. Lukyanov, S. Mandal, J. Mrázek, F. Negoita, Yu.-E. Penionzhkevich, Zs. Podolyák, P. Roussel-Chomaz, M. G. Saint-Laurent, H. Savajols, G. Sletten, J. Timár, C. Timis, and A. Yamamoto. Disappearance of the N = 14 shell gap in the carbon isotopic chain. *Physical Review C*, 78(3):034315, September 2008.

[13] F. Ajzenberg-Selove. Energy levels of light nuclei A = 18–20. *Nuclear Physics A*, 475(1):1–198, 1987.

[14] M. Wiedeking, P. Fallon, A. O. Macchiavelli, J. Gibelin, M. S. Basunia, R. M. Clark, M. Cromaz, M.-A. Deleplanque, S. Gros, H. B. Jeppesen, P. T. Lake, I.-Y. Lee, L. G. Moretto, J. Pavan, L. Phair, E. Rodriguez-Vietiez, L. A. Bernstein, D. L. Bleuel, J. T. Burke, S. R. Lesher, B. F. Lyles, and N. D. Scielzo. Lifetime measurement of the first excited 2^+ state in ^{16}C. *Phys. Rev. Lett.*, 100:152501, Apr 2008.

[15] Petri M. et al. Lifetime measurement of the 2_1^+ state in ^{20}C. *Phys. Rev. Lett.*, 107:102501, 2011.

[16] A. H. Wuosmaa, B. B. Back, S. Baker, B. A. Brown, C. M. Deibel, P. Fallon, C. R. Hoffman, B. P. Kay, H. Y. Lee, J. C. Lighthall, A. O. Macchiavelli, S. T. Marley, R. C. Pardo, K. E. Rehm, J. P. Schiffer, D. V. Shetty, and M. Wiedeking. ^{15}C$(d,p)^{16}$C reaction and exotic behavior in ^{16}C. *Phys. Rev. Lett.*, 105:132501, Sep 2010.

[17] M. Petri et al. Structure of ^{16}C: Testing shell model and ab initio approaches. *Physical Review C*, 86(4):044329, 2012.

[18] A O Macchiavelli et al. Phenomenological analysis of B(E2) transition strengths in neutron-rich carbon isotopes. *Physical Review C*, 90(6):067305, 2014.

[19] S. Raman, C.W. Nestor, and P. Tikannen. Transition probability from the ground to the first-excited 2+ state of even–even nuclides. *Atomic Data and Nuclear Data Tables*, 78(1):1–128, 2001.

[20] H. J. Ong, N. Imai, D. Suzuki, H. Iwasaki, H. Sakurai, T. K. Onishi, M. K. Suzuki, S. Ota, S. Takeuchi, T. Nakao, Y. Togano, Y. Kondo, N. Aoi, H. Baba, S. Bishop, Y. Ichikawa, M. Ishihara, T. Kubo, K. Kurita, T. Motobayashi, T. Nakamura, T. Okumura, and Y. Yanagisawa. Lifetime measurements of first excited states in ^{16,18}C. *Phys. Rev. C*, 78:014308, Jul 2008.

[21] P. Voss, T. Baugher, D. Bazin, R. M. Clark, H. L. Crawford, A. Dewald, P. Fallon, A. Gade, G. F. Grinyer, H. Iwasaki, A. O. Macchiavelli, S. McDaniel, D. Miller, M. Petri, A. Ratkiewicz, W. Rother, K. Starosta, K. A. Walsh, D. Weisshaar, C. Forssén, R. Roth,

and P. Navrátil. Excited-state transition-rate measurements in ^{18}c. *Phys. Rev. C*, 86:011303, Jul 2012.

[22] B. Pritychenko, M. Birch, B. Singh, and M. Horoi. Tables of e2 transition probabilities from the first 2+ states in even–even nuclei. *Atomic Data and Nuclear Data Tables*, 107:1–139, 2016.

[23] Warburton E. K. and Brown B. A. Effective interactions for the 0p1s0d nuclear shell-model space. *Phys. Rev. C*, 46:923–944, 1992.

[24] E Gueorguieva, M Kaci, C Schück, A Minkova, Ch Vieu, J.J Correia, and J.S Dionisio. The recoil shadow anisotropy method. *Nuclear Instruments and Methods in Physics Research Section A: Accelerators, Spectrometers, Detectors and Associated Equipment*, 474(2):132–142, 2001.

[25] N. Imai, H. J. Ong, N. Aoi, H. Sakurai, K. Demichi, H. Kawasaki, H. Baba, Zs. Dombrádi, Z. Elekes, N. Fukuda, Zs. Fülöp, A. Gelberg, T. Gomi, H. Hasegawa, K. Ishikawa, H. Iwasaki, E. Kaneko, S. Kanno, T. Kishida, Y. Kondo, T. Kubo, K. Kurita, S. Michimasa, T. Minemura, M. Miura, T. Motobayashi, T. Nakamura, M. Notani, T. K. Onishi, A. Saito, S. Shimoura, T. Sugimoto, M. K. Suzuki, E. Takeshita, S. Takeuchi, M. Tamaki, K. Yamada, K. Yoneda, H. Watanabe, and M. Ishihara. Anomalously hindered $e2$ strength $b(e2; 2_1^+ \rightarrow 0^+)$ in ^{16}C. *Phys. Rev. Lett.*, 92:062501, Feb 2004.

[26] A. Chester, P. Adrich, A. Becerril, D. Bazin, C.M. Campbell, J.M. Cook, D.-C. Dinca, W.F. Mueller, D. Miller, V. Moeller, R.P. Norris, M. Portillo, K. Starosta, A. Stolz, J.R. Terry, H. Zwahlen, C. Vaman, and A. Dewald. Application of the time-of-flight technique for lifetime measurements with relativistic beams of heavy nuclei. *Nuclear Instruments and Methods in Physics Research Section A: Accelerators, Spectrometers, Detectors and Associated Equipment*, 562(1):230–240, 2006.

[27] P. Adrich, D. Enderich, D. Miller, V. Moeller, R.P. Norris, K. Starosta, C. Vaman, P. Voss, and A. Dewald. A simulation tool for recoil distance method lifetime measurements at nscl. *Nuclear Instruments and Methods in Physics Research Section A: Accelerators, Spectrometers, Detectors and Associated Equipment*, 598(2):454–464, 2009.

[28] Gamow G. Mass defect curve and nuclear constitution. *Proc. R. Soc. Lond.A*, 126(932-644), September 1930.

[29] J.A. Wheeler N. Bohr. The mechanism of nuclear fission. *Phys. Rev.*, 56, 1939.

[30] K. S. Krane. *Introductory nuclear physics.* New York: John Wiley Sons., 1988.

[31] J. Lilley. *Nuclear Physics: Principles and Applications.* Wiley Sons, 2001.

[32] B.L. Cohen. *Concepts of Nuclear Physics*. McGraw-Hill, New York, 1971.

[33] J. Bartlett. Nuclear structure. *Nuclear Structure*, 130(165):437–442, 1932.

[34] W. M. Elsasser. Sur le principe de Pauli dans les noyaux, journal = J. Phys. Radium, year = 1933, volume = 4, pages = 549-556, number = 0, month = sep, doi = 10.1051/jphysrad:01933004010054900, publisher = American Physical Society,.

[35] M. G. Mayer and J. H. D. Jensen. *Elementary Theory of Nuclear Shell Structure*. John Wiley & Sons, Inc., 1955.

[36] Maria Goeppert Mayer. On closed shells in nuclei. ii. *Phys. Rev.*, 75:1969–1970, Jun 1949.

[37] Otto Haxel, J. Hans D. Jensen, and Hans E. Suess. On the "magic numbers" in nuclear structure. *Phys. Rev.*, 75:1766–1766, Jun 1949.

[38] D.S. Saxon R.D. Woods. *Diffuse Surface Optical Model for Nucleon-Nuclei Scattering*. McGraw-Hill, New York, 1968.

[39] Casten R. *Nuclear structure from a simple perspective*, volume 23. Oxford University Press on Demand, 2000.

[40] Maria G. Mayer. The shell model. *Nobel Lectures*, Physics:20–37, 1963.

[41] A. Ozawa, T. Kobayashi, T. Suzuki, K. Yoshida, and I. Tanihata. New magic number, $N = 16$, near the neutron drip line. *Phys. Rev. Lett.*, 84:5493–5495, Jun 2000.

[42] A. Gade and J. Tostevin. Knockout reactions. *Nuclear Physics News*, 20:11–16, 2010.

[43] Jim Al-Khalili and Filomena Nunes. Reaction models to probe the structure of light exotic nuclei. *Journal of Physics G: Nuclear and Particle Physics*, 29(11):R89–R132, oct 2003.

[44] Taylor J. *Proton Induced Quasi-free Scattering with Inverse Kinematics*. PhD thesis, 2011.

[45] Wamers F. Quasi-free-scattering and one-proton-removal reactions with the proton-dripline nucleus ^{17}Ne at relativistic beam energies. *Technical University of Darmstadt*, 2011.

[46] Z. Elekes, Zs. Dombrádi, R. Kanungo, H. Baba, Zs. Fülöp, J. Gibelin, Á. Horváth, E. Ideguchi, Y. Ichikawa, N. Iwasa, H. Iwasaki, S. Kanno, S. Kawai, Y. Kondo, T. Motobayashi, M. Notani, T. Ohnishi, A. Ozawa, H. Sakurai, S. Shimoura, E. Takeshita, S. Takeuchi, I. Tanihata, Y. Togano, C. Wu, Y. Yamaguchi, Y. Yanagisawa, A. Yoshida, and K. Yoshida. Low-lying excited states in 17,19c. *Physics Letters B*, 614(3):174–180, 2005.

[47] M.E. Cobern G.E. Moore S. Mordechai R.V. Kollarits H. Nann W. Chung H.T.Fortune, R. Middleton and B.H. Wildenthal. Spectroscopy of ^{16}c. *Physics Letters B*, 70:408–410, 1977.

[48] D.P. Balamuth, J.M. Lind, K.C. Young, and R.W. Zurmühle. Angular correlation study of levels in 16c. *Nuclear Physics A*, 290(1):65–71, 1977.

[49] H. T. Fortune, M. E. Cobern, S. Mordechai, G. E. Moore, S. Lafrance, and R. Middleton. $(sd)^2$ states in ^{14,16}C. *Phys. Rev. Lett.*, 40:1236–1239, May 1978.

[50] Y. Satou, J.W. Hwang, S. Kim, K. Tshoo, S. Choi, T. Nakamura, Y. Kondo, N. Matsui, Y. Hashimoto, T. Nakabayashi, T. Okumura, M. Shinohara, N. Fukuda, T. Sugimoto, H. Otsu, Y. Togano, T. Motobayashi, H. Sakurai, Y. Yanagisawa, N. Aoi, S. Takeuchi, T. Gomi, M. Ishihara, S. Kawai, H.J. Ong, T.K. Onishi, S. Shimoura, M. Tamaki, T. Kobayashi, Y. Matsuda, N. Endo, and M. Kitayama. One-neutron knockout reaction of 17c on a hydrogen target at 70 mev/nucleon. *Physics Letters B*, 728:462–466, 2014.

[51] H. G. Bohlen, R. Kalpakchieva, B. Gebauer, S. M. Grimes, H. Lenske, K. P. Lieb, T. N. Massey, M. Milin, W. von Oertzen, Ch. Schulz, T. Kokalova, S. Torilov, and S. Thummerer. Spectroscopy of particle-hole states of ^{16}C. *Phys. Rev. C*, 68:054606, Nov 2003.

[52] R. Gilman, H. T. Fortune, L. C. Bland, Rex R. Kiziah, C. Fred Moore, Peter A. Seidl, C. L. Morris, and W. B. Cottingame. Nonanalog (π^-,π^+) double charge exchange on ^{18}O. *Phys. Rev. C*, 30:962–964, Sep 1984.

[53] F. Becker M. Belleguic C. Borcea C. Bourgeois B. A. Brown Z. Dlouhy Z. Dombrádi Z. Fülöp H. Grawe S. Grévy F. Ibrahim A. Kerek A. Krasznahorkay M. Lewitowicz S. Lukyanov H. van der Marel P. Mayet J. Mrázek S. Mandal D. Guillemaud-Mueller F. Negoita Y. E. Penionzhkevich Z. Podolyák P. Roussel-Chomaz M. G. Saint Laurent H. Savajols O. Sorlin G. Sletten D. Sohler J. Timár C. Timis A. Yamamoto M. Stanoiu, F. Azaiez. Study of drip line nuclei through two-step fragmentation. *Eur. Phys. J. A*, 20:95–96, 2003.

[54] Y. Kondo, T. Nakamura, Y. Satou, T. Matsumoto, N. Aoi, N. Endo, N. Fukuda, T. Gomi, Y. Hashimoto, M. Ishihara, S. Kawai, M. Kitayama, T. Kobayashi, Y. Matsuda, N. Matsui, T. Motobayashi, T. Nakabayashi, K. Ogata, T. Okumura, H. J. Ong, T. K. Onishi, H. Otsu, H. Sakurai, S. Shimoura, M. Shinohara, T. Sugimoto, S. Takeuchi, M. Tamaki, Y. Togano, and Y. Yanagisawa. One-neutron removal reactions of ^{18}C and ^{19}C on a proton target. *Phys. Rev. C*, 79:014602, Jan 2009.

[55] A. A. Revel, F. M. Marqués, O. Sorlin, T. Aumann, C. Caesar, M. Holl, V. Panin, M. Vandebrouck, F. Wamers, H. Alvarez-Pol, L. Atar, V. Avdeichikov, S. Beceiro-Novo, D. Bemmerer, J. Benlliure, C. A. Bertulani, J. M. Boillos, K. Boretzky, M. J. G. Borge,

M. Caamaño, E. Casarejos, W. N. Catford, J. Cederkäll, M. Chartier, L. Chulkov, D. Cortina-Gil, E. Cravo, R. Crespo, U. Datta Pramanik, P. Díaz Fernández, I. Dillmann, Z. Elekes, J. Enders, O. Ershova, A. Estradé, F. Farinon, L. M. Fraile, M. Freer, D. Galaviz, H. Geissel, R. Gernhäuser, P. Golubev, K. Göbel, J. Hagdahl, T. Heftrich, M. Heil, M. Heine, A. Heinz, A. Henriques, A. Ignatov, H. T. Johansson, B. Jonson, J. Kahlbow, N. Kalantar-Nayestanaki, R. Kanungo, A. Kelic-Heil, A. Knyazev, T. Kröll, N. Kurz, M. Labiche, C. Langer, T. Le Bleis, R. Lemmon, S. Lindberg, J. Machado, J. Marganiec, A. Movsesyan, E. Nacher, M. Najafi, T. Nilsson, C. Nociforo, S. Paschalis, A. Perea, M. Petri, S. Pietri, R. Plag, R. Reifarth, G. Ribeiro, C. Rigollet, M. Röder, D. Rossi, D. Savran, H. Scheit, H. Simon, I. Syndikus, J. T. Taylor, O. Tengblad, R. Thies, Y. Togano, P. Velho, V. Volkov, A. Wagner, H. Weick, C. Wheldon, G. Wilson, J. S. Winfield, P. Woods, D. Yakorev, M. Zhukov, A. Zilges, and K. Zuber. Strong neutron pairing in core + $4n$ nuclei. *Phys. Rev. Lett.*, 120:152504, Apr 2018.

[56] Z. Elekes, Zs. Dombrádi, T. Aiba, N. Aoi, H. Baba, D. Bemmerer, B. A. Brown, T. Furumoto, Zs. Fülöp, N. Iwasa, Á. Kiss, T. Kobayashi, Y. Kondo, T. Motobayashi, T. Nakabayashi, T. Nannichi, Y. Sakuragi, H. Sakurai, D. Sohler, M. Takashina, S. Takeuchi, K. Tanaka, Y. Togano, K. Yamada, M. Yamaguchi, and K. Yoneda. Persistent decoupling of valence neutrons toward the dripline: Study of ^{20}C by γ spectroscopy. *Phys. Rev. C*, 79:011302, Jan 2009.

[57] J. D. Garrett, F. Ajzenberg-Selove, and H. G. Bingham. Levels of ^{15}C from a study of ^{9}Be(^{7}Li, p)^{15}C. *Phys. Rev. C*, 10:1730–1738, Nov 1974.

[58] M. Hass, H.T. King, E. Ventura, and D.E. Murnick. Measurement of the magnetic moment of the first excited state of 15c. *Physics Letters B*, 59(1):32–34, 1975.

[59] D. E. Alburger and D. J. Millener. Beta decay of ^{15}C. *Phys. Rev. C*, 20:1891–1901, Nov 1979.

[60] B.A. Brown H.A. Doubt J. Asher, D.W. Bennett and M.A. Grace. A measurement of the g factor of the 0.74 mev $5/2^+$ state of ^{15}C. *J. Phys. G: Nucl. Phys.*, 6:251–259, 1980.

[61] H. T. Fortune. Widths in ^{15}C and ^{15}F. *Phys. Rev. C*, 83:024311, Feb 2011.

[62] Joseph Cerny. Studies of exotic light nuclei. *Proceedings of the Third International Conference on Nuclei Far from Stability, Cargese, Corsica, France*, CERN-76:225–234, Sep 1976.

[63] R. Jahn, G. J. Wozniak, D. P. Stahel, and Joseph Cerny. (α,^{2} He) reaction as a spectroscopic tool for investigating high-spin states. *Phys. Rev. Lett.*, 37:812–816, Sep 1976.

[64] F.E. Cecil, J.R. Shepard, R.E. Anderson, R.J. Peterson, and P. Kaczkowski. Charged particle reaction studies on 14c. *Nuclear Physics A*, 255(2):243–249, 1975.

[65] S. E. Darden, G. Murillo, and S. Sen. $d_{3/2}$ 1p-2h strength in ^{15}C. *Phys. Rev. C*, 32:1764–1766, Nov 1985.

[66] G. Murillo, S. Sen, and S.E. Darden. A study of the reactions14c(→d, d)14c and 14c(→d, p)15c at 16.0 mev. *Nuclear Physics A*, 579(1):125–143, 1994.

[67] Bi Pin-Zhen. Binding energy and deep inelastic scattering. *Modern Physics Letters A*, 03(07):653–659, 1988.

[68] W. Von Oertzen. Nuclear reactions below the fermi-energy regime: The unique physics of a finite multiparticle system. *Nuclear Instruments and Methods in Physics Research Section A: Accelerators, Spectrometers, Detectors and Associated Equipment*, 287(1):188–199, 1990.

[69] Y. Satou, T. Nakamura, N. Fukuda, T. Sugimoto, Y. Kondo, N. Matsui, Y. Hashimoto, T. Nakabayashi, T. Okumura, M. Shinohara, T. Motobayashi, Y. Yanagisawa, N. Aoi, S. Takeuchi, T. Gomi, Y. Togano, S. Kawai, H. Sakurai, H.J. Ong, T.K. Onishi, S. Shimoura, M. Tamaki, T. Kobayashi, H. Otsu, Y. Matsuda, N. Endo, M. Kitayama, and M. Ishihara. Unbound excited states in 19,17c. *Physics Letters B*, 660(4):320–325, 2008.

[70] D. Suzuki, H. Iwasaki, H.J. Ong, N. Imai, H. Sakurai, T. Nakao, N. Aoi, H. Baba, S. Bishop, Y. Ichikawa, M. Ishihara, Y. Kondo, T. Kubo, K. Kurita, T. Motobayashi, T. Nakamura, T. Okumura, T.K. Onishi, S. Ota, M.K. Suzuki, S. Takeuchi, Y. Togano, and Y. Yanagisawa. Lifetime measurements of excited states in 17c: Possible interplay between collectivity and halo effects. *Physics Letters B*, 666(3):222–227, 2008.

[71] D. Smalley, H. Iwasaki, P. Navrátil, R. Roth, J. Langhammer, V. M. Bader, D. Bazin, J. S. Berryman, C. M. Campbell, J. Dohet-Eraly, P. Fallon, A. Gade, C. Langer, A. Lemasson, C. Loelius, A. O. Macchiavelli, C. Morse, J. Parker, S. Quaglioni, F. Recchia, S. R. Stroberg, D. Weisshaar, K. Whitmore, and K. Wimmer. Lifetime measurements of ^{17}C excited states and three-body and continuum effects. *Phys. Rev. C*, 92:064314, Dec 2015.

[72] H. Ueno, H. Miyatake, Y. Yamamoto, S. Tanimoto, T. Shimoda, N. Aoi, K. Asahi, E. Ideguchi, M. Ishihara, H. Izumi, T. Kishida, T. Kubo, S. Mitsuoka, Y. Mizoi, M. Notani, H. Ogawa, A. Ozawa, M. Sasaki, T. Shirakura, N. Takahashi, and K. Yoneda. β-delayed neutron and γ-ray spectroscopy of ^{17}c utilizing spin-polarized ^{17}b. *Phys. Rev. C*, 87:034316, Mar 2013.

[73] Sunji Kim, Jongwon Hwang, Yoshiteru Satou, Nigel A. Orr, Takashi Nakamura, Yosuke Kondo, Julien Gibelin, N. Lynda Achouri, Thomas Aumann, Hidetada Baba, Franck Delaunay, Pieter Doornenbal, Naoki Fukuda, Naohito Inabe, Tadaaki Isobe, Daisuke Kameda, Daiki Kanno, Nobuyuki Kobayashi, Toshio Kobayashi, Toshiyuki Kubo, Sylvain Leblond, Jenny Lee, F. Miguel Marqués, Ryogo Minakata, Tohru Motobayashi,

Daichi Murai, Tetsuya Murakami, Kotomi Muto, Tomohiro Nakashima, Noritsugu Nakatsuka, Alahari Navin, Seijiro Nishi, Shun Ogoshi, Hideaki Otsu, Hiromi Sato, Yohei Shimizu, Hiroshi Suzuki, Kento Takahashi, Hiroyuki Takeda, Satoshi Takeuchi, Ryuki Tanaka, Yasuhiro Togano, Adam G. Tuff, Marine Vandebrouck, and Ken ichiro Yoneda. Invariant mass spectroscopy of ^{17}C via one-neutron knockout reaction of ^{18}C. *JPS Conf. Proc.*, page 030031, 2015.

[74] Zs. Vajta, Zs. Dombrádi, Z. Elekes, T. Aiba, N. Aoi, H. Baba, D. Bemmerer, Zs. Fülöp, N. Iwasa, Á. Kiss, T. Kobayashi, Y. Kondo, T. Motobayashi, T. Nakabayashi, T. Nannichi, H. Sakurai, D. Sohler, S. Takeuchi, K. Tanaka, Y. Togano, K. Yamada, M. Yamaguchi, and K. Yoneda. γ-ray spectroscopy of ^{19}C via the single-neutron knock-out reaction. *Phys. Rev. C*, 91:064315, Jun 2015.

[75] K. Whitmore, D. Smalley, H. Iwasaki, T. Suzuki, V. M. Bader, D. Bazin, J. S. Berryman, B. A. Brown, C. M. Campbell, P. Fallon, A. Gade, C. Langer, A. Lemasson, C. Loelius, A. O. Macchiavelli, C. Morse, T. Otsuka, J. Parker, F. Recchia, S. R. Stroberg, D. Weisshaar, and K. Wimmer. Magnetic response of the halo nucleus ^{19}C studied via lifetime measurement. *Phys. Rev. C*, 91:041303, Apr 2015.

[76] M. Thoennessen, S. Mosby, N.S. Badger, T. Baumann, D. Bazin, M. Bennett, J. Brown, G. Christian, P.A. DeYoung, J.E. Finck, M. Gardner, E.A. Hook, B. Luther, D.A. Meyer, M. Mosby, W.F. Rogers, J.K. Smith, A. Spyrou, and M.J. Strongman. Observation of a low-lying neutron-unbound state in 19c. *Nuclear Physics A*, 912:1–6, 2013.

[77] S. Altstadt. *$^{13,14}B(n,\gamma)$ via Coulomb Dissociation to Constrain the Astrophysical r-Process.* PhD thesis, Goethe Universität Frankfurt, 2014.

[78] Ralf Plag. land02, 2013.

[79] Díaz-Fernández P. *An investigation into quasi-free scattering of light neutron-rich nuclei around N=14.* PhD thesis, 2013.

[80] Holl M. Quasi-free scattering from relativistic neutron-deficient carbon isotopes, 2014.

[81] Olga Ershova. *Coulomb Dissociation Reactions on Molybdenum Isotopes for Astrophysics Applications.* PhD thesis, Frankfurt, 2011.

[82] Ralf Plag. Land02: featuring the unofficial guide to the unofficial version of land02.

[83] C. Caesar. Beyond the neutron drip line: The unbound oxygen isotopes ^{25}o and ^{26}o. *Phys. Rev. C*, 88:034313, Sep 2013.

[84] Julian Kahlbow. *One-Neutron Removal Reactions on ^{11}Be and ^{12}Be.* PhD thesis, Darmstadt, 2015.

[85] Ina Syndikus. *Proton Knockout Reactions from Neutron-Rich N isotopes at R^3B.* PhD thesis, 2019.

[86] Ralf Plag. Some documentation on ralf's tracker.

[87] R. Thies. Prototype tests and pilot experiments for the r^3b scintillator-based detection systems, 2011.

[88] Dominic M. Rossi. *Investigation of the Dipole Response of Nickel Isotopes in the Presence of a High-Frequency Electromagnetic Field.* PhD thesis, 2009.

[89] V. Panin. *Fully Exclusive Measurements of Quasi-Free Single-Nucleon Knockout Reactions in Inverse Kinematics.* PhD thesis, 2012.

[90] Simulations and Data Analysis for R3B. R3broot website, 2022.

[91] G. García. Private communication. 2022.

[92] G. Breit and E. Wigner. Capture of slow neutrons. *Phys. Rev.*, 49:519–531, Apr 1936.

[93] Steve Baker and Robert D. Cousins.

[94] A. Brown. Private communication. 2022.

[95] H. T. Fortune. Effective interactions for the 0p1s0d nuclear shell-model space. *Phys. Rev. C*, 46:923–944, 1992.

[96] P. Díaz-Fernández. Quasifree (p, pn) scattering of light neutron-rich nuclei near $n = 14$. *Phys. Rev. C*, 97:024311, Feb 2018.